universität wien

MASTERARBEIT / MASTER'S THESIS

Titel der Masterarbeit / Title of the Master's Thesis

„Microstructures and Clay Mineralogy of Fault and Wall Rocks in the Opalinus Clay Formation“

verfasst von / submitted by

Jonas Strasser, BSc

angestrebter akademischer Grad / in partial fulfilment of the requirements for the degree of

Master of Science (MSc)

Wien, 2023 / Vienna 2023

Studienkennzahl lt. Studienblatt / degree programme code as it appears on the student record sheet:	A 066 815
Studienrichtung lt. Studienblatt / degree programme as it appears on the student record sheet:	Master Erdwissenschaften
Betreut von / Supervisor:	Ao. Univ. Prof. Susanne Gier
Mitbetreut von / Co-Supervisor:	Dr. Kurt Decker

Contents

Abstract

The Opalinus Clay is considered a suitable host-rock for the disposal of nuclear waste, because of its self-sealing property, which is caused by swelling clay minerals such as smectite. The aim of this thesis is to investigate if this self-sealing property is influenced by the formation of fault zones. In this study, samples from both fault rock and undeformed wall rock were analysed for their mineralogical properties using x-ray diffraction analysis (XRD). Furthermore, the total carbon content and the cation exchange capacity were measured. To determine changes in the microstructure, the specimens were examined using a digital microscope and scanning electron microscope. Based on the measured length of grooves behind ploughing clasts, displacements of less than 4 mm can be identified. Furthermore, a mechanical grain size reduction can be identified on the shiny slip surfaces. The deformation occurs only on a narrow section and produces a decomposition of the clay minerals. On one sample the slickenside is covered with spherical nanoparticles, which are post-tectonic in origin. Despite low slip rates, a direction of movement is recognizable on some samples. The results show that there is no difference in bulk mineralogy, but there is a minor difference in clay mineralogy, total organic carbon, and cation exchange capacity between the samples from the wall rock and the samples from the fault rock. XRD indicates an increase of illite in illite/smectite (I/S) mixed layer minerals of fault rocks, compared to wall rocks. Wall rock samples consist of (R1) I/S containing 73-74 % illite, whereas fault rock samples consist of (R1) I/S containing 77-80 % illite. Finally, samples from fault zones have a lower cation exchange capacity and a higher organic carbon content. The wall rock specimen shows CEC values of 35 mEq/100g, compared to the adjacent fault rock, which shows CEC values of 17 and 26 mEq/100g.

Zusammenfassung

Der Opalinuston ist aufgrund seiner quellfähigen Tonminerale wie Smektit ein vielversprechendes Wirtsgestein für die Endlagerung von radioaktiven Abfällen. Im Rahmen dieser Masterarbeit wurden Gesteine aus Störungszonen und nicht deformierten Bereichen des Opalinuston untersucht, um zur Klärung der Frage beizutragen, ob Gesteine in Störungszonen weniger quellfähig sind und somit eine potenzielle Schwachstelle für die Langzeitlagerung von radioaktiven Abfällen darstellen. Die Proben wurden mit Röntgendiffraktometrie untersucht, um gesamtmineralogische und tonmineralogische Änderungen festzustellen. Weiters wurde der gesamte organische Kohlenstoff und die Kationenaustauschkapazität bestimmt. Für die Identifizierung von Mikrostrukturen im Tonstein wurden die Proben mit einem Digitalmikroskop und Rasterelektronenmikroskop untersucht. Die Ergebnisse zeigen keine Änderung in der Gesamtmineralogie, jedoch eine geringfügige Änderung in der Tonmineralogie. Gesteine von Störungszonen haben „Mixed-Layer-Tonminerale“ mit einem höheren Illitgehalt (77-80 %) als undeformierte Gesteine (73-74 %), was auf eine Verminderung der Quellfähigkeit hinweist. Des Weiteren haben Gesteine von Störungszonen eine niedrigere Kationenaustauschkapazität und einen höheren Gehalt an organischem Kohlenstoff. Die Kationenaustauschkapazität beträgt 17 und 26 mEq/100g für Störungsgesteine und 35 mEq/100g für undeformierte Gesteine. Mikrostrukturelle Änderungen sind nur direkt auf der Scherfläche von Störungszonen erkennbar und zeigen eine mechanische Zerlegung der Tonminerale. Darüber hinaus sind Versätze von weniger als 4 mm und Bewegungsrichtungen erkennbar.

Chapter 1

Introduction

1.1 Importance of clays in the radioactive waste disposal

Clays are one of the most essential raw materials and are used in countless applications all over the world. In the past few years, clay has become a significant player as a suitable host-rock for a nuclear waste repository (IAEA, 2003).

In Switzerland, it was decided to use the Jurassic Opalinus Clay as a host rock for high-level radioactive waste (NAGRA, 2002*a*). Not only because of the low hydraulic permeability/conductivity but also because of the high retention of radionuclides clay is an excellent host rock (Lee and Tank, 1985; NAGRA, 2002*a*). Another well-known property of clay is that some clay minerals are swellable. Several experiments have shown that the Opalinus Clay contains these minerals and, therefore, has a high swelling capacity (Zhang et al., 2007; Crisci et al., 2018). One of these swelling clay minerals is called smectite, which is the group name for several minerals like montmorillonite, saponite, nontronite, and hectorite (Murray, 2006*a*). Smectites are so-called three-layer minerals consisting of two silica tetrahedral (T) sheets, which surround one octahedral (O) sheet. A negative layer charge of about -0.66 per unit cell occurs, because of the substitution of trivalent cations (Al^{3+}, Fe^{3+}) by divalent cations (Fe^{2+}, Mg^{2+}) (Grim, 1962). This charge is balanced by exchangeable cations like sodium or calcium, which are hydrated by one (for sodium) or two (for calcium) molecular water layers (Grim, 1962). Consequently, an expansion of the smectite mineral occurs. Therefore host rocks like the Opalinus Clay have a self-sealing property, which can seal preferential flow-paths like fault zones and zones which got disturbed due to excavation (NAGRA, 2002*b*).

However, the amount of smectite is dependent on temperature, time, and water chemistry (Hower et al., 1976; Pytte and Reynolds, 1989; Whitney, 1990). For instance, bentonite at 100 °C over a period of 100 years causes a loss in smectite

of 1-8 % (Zheng et al., 2015). During this process, also called smectite illitization, smectite is becoming more "illitic", resulting in loss of swelling capacity due to the non-expandability of illite (Ohazuruike and Lee, 2023). This illitization process progresses in phases, generating mixed-layer minerals increasing in order (Nadeau, 1981). During this diagenesis process in a K-rich environment, smectite and mixed-layer of illite-smectite (I/S) changes as follows (Schoonheydt and Johnston, 2006):
$smecitite \rightarrow I/S\,R0 \rightarrow I/S\,R1 \rightarrow I/S\,R3 \rightarrow Illite \rightarrow muscovite$
The illite content increases in the mixed-layer mineral with I/S R0 having 0-60 % illite layers, I/S R1 65-85 % illite layers, and R3 I/S 85-100 % illite layers (Schoonheydt and Johnston, 2006).
Most studies on porosity and mineralogy of fault rocks in the Opalinus Clay were carried out, using sample material from the main fault at the Mont Terri Laboratory (Gaucher et al., 2003; Keller et al., 2013; Orellana et al., 2022). Furthermore, recent studies have shown that the porosity in fault rocks is higher than in intact clays (Orellana et al., 2022). A suspected smectite-illite transformation in the main fault of the Opalinus Clay (Laurich et al., 2014) makes further investigations even more critical.

1.2 Aim of this study

The research question of this thesis is whether the swelling/self-sealing properties of the Opalinus Clay change due to the formation of fault rocks. Therefore, properties such as bulk mineralogy, clay mineralogy, cation-exchange capacity and total organic carbon concentration were analyzed in detail in the undeformed wall rocks, as well as in the deformed fault rocks. Furthermore, structural investigations within the fault rocks and in the transition zone to the wall rock were carried out using a high-resolution digital microscope and electron microscope. Understanding the deformation processes on a microscopic scale should also help explain changes in mineralogy, porosity, and permeability. These detailed studies are of great importance, as the encapsulation of nuclear wastes must be ensured over a timescale of one million years.

1.3 Geological setting

The Opalinus Clay investigated in this study originated from three different boreholes BAC1-1, RHE1-1, and STA2-1, which are located in the Folded Jura in northern Switzerland (Figure 1.2). Geographically, borehole RHE 1-1 is located between Schaffhausen and Eglisau and boreholes STA 2-1 and BAC1-1 are located east of it, between Eglisau and Baden (Figure 1.2). The Opalinus Clay was deposited in the lower Dogger (about 174 Ma ago) and consists of sandy shales, and grey, silty, micaceous clays, with an average thickness between 80 m and 120 m (NAGRA, 2002*b*; Nussbaum et al., 2011). Further, the Opalinus Clay can be divided into five sub-units of three facies from the bottom to the top (Bläsi et al., 1991; Hostettler et al., 2017): dark-grey shaly facies, carbonate-rich sandy facies, sandy facies with sandstone lenses, dark-grey shaly facies with mica and pyrite, and light-grey sandy facies (Figure 1.1). These different facies can be explained by changes in depositional conditions, in the shallow-marine epicontinental sea (Lauper et al., 2018). Above the Opalinus Clay Formation is the Passwang Formation, which contains oolitic limestones with lithoclasts in the lower part (Hostettler et al., 2017). Further east from Jura where the borehole BAC1-1 is located, there is the Murchisonae-Oolith Formation, an equivalent of the Passwang Formation (Burkhalter et al., 1997; Bläsi et al., 2013) (Figure 1.1). Below the Opalinus Clay Formation is the Staffelegg Formation, composed of brownish-black silty mudstone in the lower part, and grey marls in the upper part (Hostettler et al., 2017).

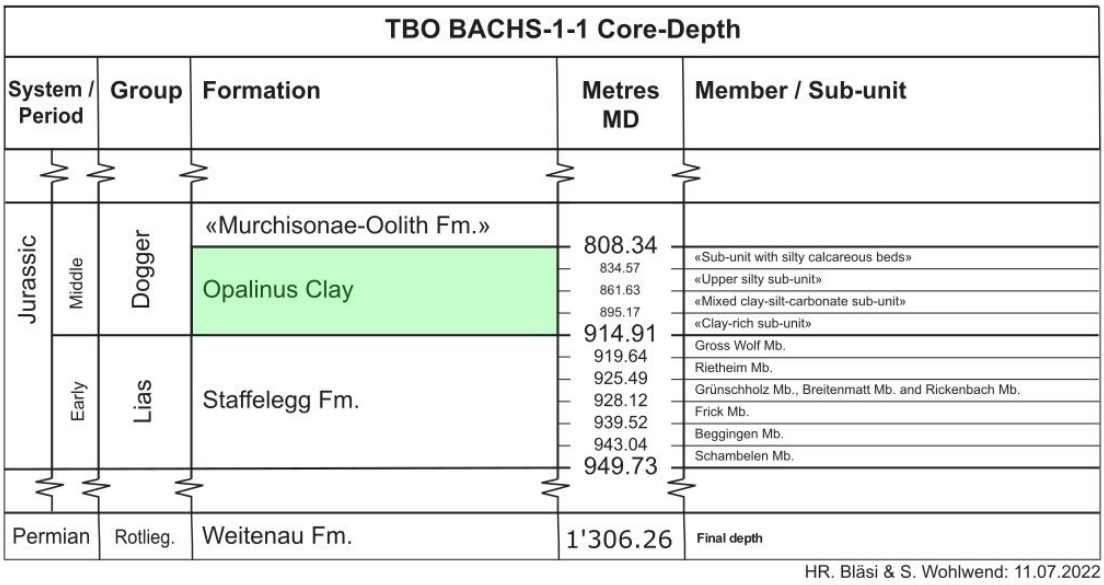

Figure 1.1: Section of stratigraphy of Nagra's deep borehole Bachs (BAC1-1). The final depth is 1306 m. In this borehole, the Opalinus Clay is located between 808 m and 914 m and can be divided into four subunits.
For the total stratigraphic chart see Figure A.1.
Adapted from NAGRA (2021).

From north to south, the thickness of the Jura belt increases, reaching a maximum thickness of 3 km (Büchi et al., 1965). During the Cretaceous burial temperature of the Opalinus Clay were between 75 °C to 90 °C (Mazurek et al., 2006). Studies have shown that during the thin-skinned deformation of the Jura belt, the temperatures never exceeded 100 °C (Gehring et al., 1991).

This thin-skinned Jura fold-and-thrust belt propagated to the north and got detached at the mechanically weak, salt and anhydrite-bearing Zenglingen Formation (Nussbaum et al., 2017). Geologically, the northern part of the folded Jura borders to the Upper Rhine Graben, the western part to the Bresse Graben, and the southern part to the Molasse Basin. The Mont Terri area is characterized by NNE striking faults from the Oligocene and ENE striking faults from the late Variscan (Nussbaum et al., 2011). Earthquakes along the WSW-ENE-striking faults indicate tectonic activities (Kastrup et al., 2004). Structural analysis of the Nagra drill cores revealed two distinct thrust-type deformation related to SSW-NNE- and SSE-NNW-directed shortening, respectively (Decker et al., 2022). In the regional tectonic context, all faults are assorted to Neogene shortening of the Deformed Tabular Jura (Decker et al., 2022) (Figure 1.2). In the vicinity of the boreholes, there are WSW-ENE-striking faults as can be seen in the map (Figure 1.2).

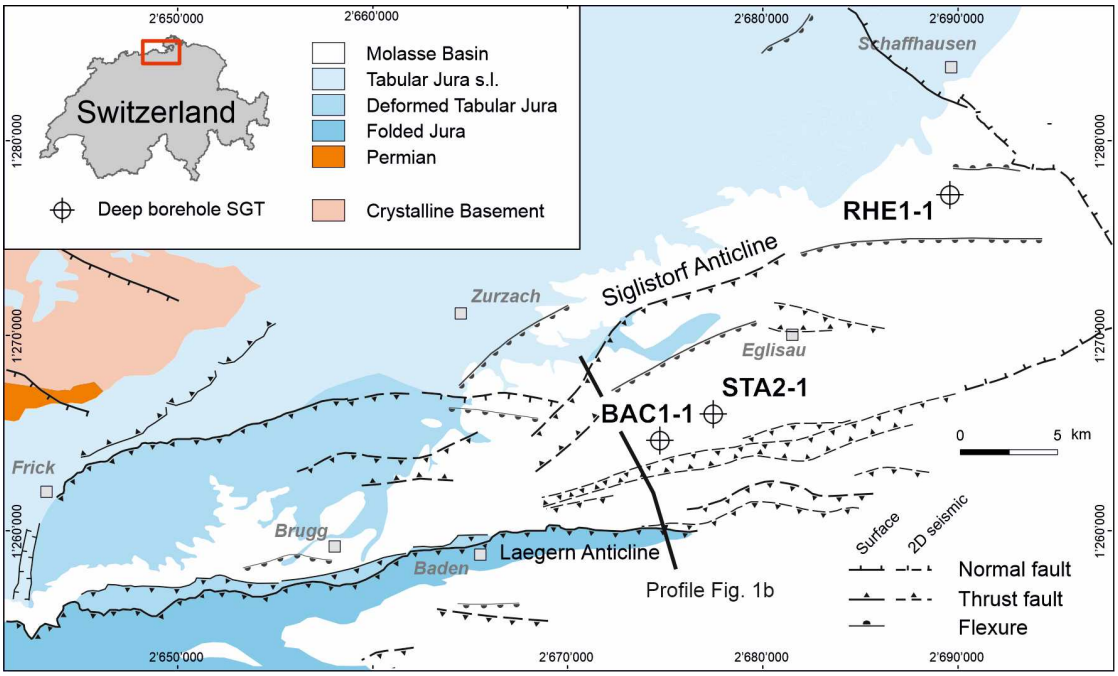

Figure 1.2: Geological overview of the study area showing the location of the boreholes BAC1-1, STA2-1, and RHE1-1. Note that all boreholes are located in the deformed Tabular Jura. The Mesozoic sediments are overlain by Paleogene to Neogene Molasse deposits. The black line shows the trace of the cross-section Figure 1.3. Note the almost parallel WSW-ENE-striking faults in the whole area. Adapted from NAGRA (2021) and Decker et al. (2022).

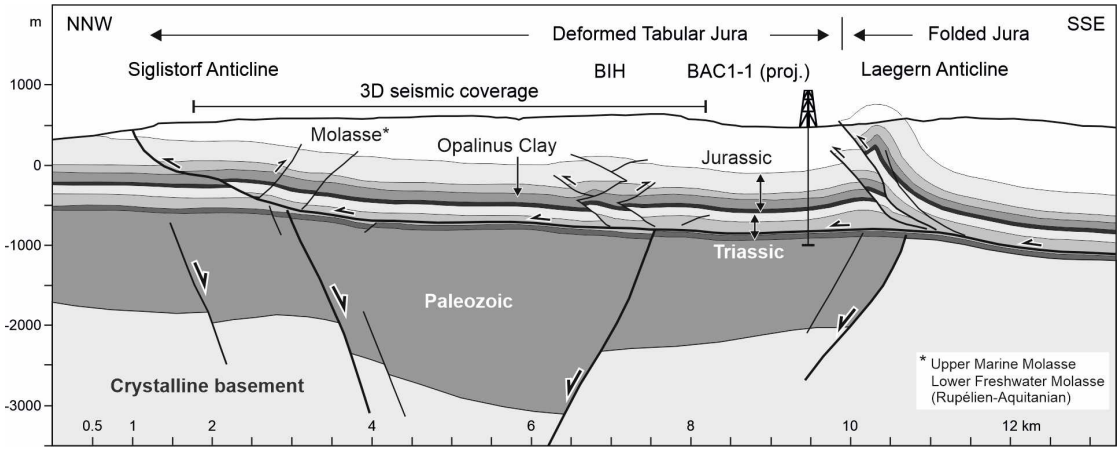

Figure 1.3: Cross-section through the study area. Note location of BAC1-1 in the deformed Tabular Jura and the Opalinus Clay between 808 m and 914 m (dark grey). The entire stratigraphic record of borehole can be seen in Figure A.1. Adapted from NAGRA (2021) and Decker et al. (2022).

Chapter 2

Methodology

2.1 Sample material and sample selection

In total, Nagra provided 15 pairs of rock samples from oriented drill cores for the analyses performed in this study (Figure 2.1, Figure 2.2). Each pair of the sample consists of a fault rock sample (labeled FR in the following) and a sample from wall rock (WR) collected from undeformed claystone next to the fault. Samples derive from the Opalinus Clay (7 pairs of samples) and similar clay-rich sediments from the formations above (Murchinsonae Oolith Fm., Wedelsandstein Fm., Variansmergel Fm.) and below the Opalinus Clay (Staffelegg Fm.). Samples derive from Nagra's deep boreholes Bachs = BAC1-1, Rheinau = RHW1-1, Stadel = STA-2-1 and STA3-3. All of the sampled fault rocks are clay gouges formed in shallow-dipping or sub-horizontal faults and thin fault zones with apparently low displacement (Decker et al., 2022). The thicknesses of the fault zones observed in the Opalinus Clay typically range from less than one millimetre to about 3 centimeters. Thicknesses of the analysed clay gouges in this study are between several tens of a millimeter and about 2 mm. Fault zones are defined by a volume of clay gouge, a series of closely-spaced sub-parallel slip surfaces combining to anastomosing networks, or by a combination of both. The spacing of the slip surfaces is less than 1 mm. By far most of the observed slip surfaces have a polished and shiny appearance ("mirror-like slickensides"). Slip surfaces are striated with striations partly formed by grooves of sand- or silt-sized ploughing clasts. In addition, many slip surfaces are overgrown by syn-kinematic mineral fibres mostly formed by calcite. Slip surfaces also form the sharp borders between fault rock and wall rock making a visual differentiation possible.

Figure 2.1: Top: Core photograph of sample STA2-1 843.38. The red rectangle shows an approximately 1,5 cm thick fault zone composed of a series of sub-parallel fault planes; on the right-hand side there is the slip surface from this zone. The striated surface is partly overgrown by syn-kinematic calcite.
Bottom: Core photograph of sample RHE1-1 637.93. Fault plane delimiting the sampled clay gouge from undeformed wall rock of the Opalinus Clay. The striated fault plane is partly coated with fibrous minerals (calcite and/or celestine). Fibers are less than 3 mm long indicating very small displacement along the fault plane of less than about 1 cm.
Adapted from Decker et al. (2022).

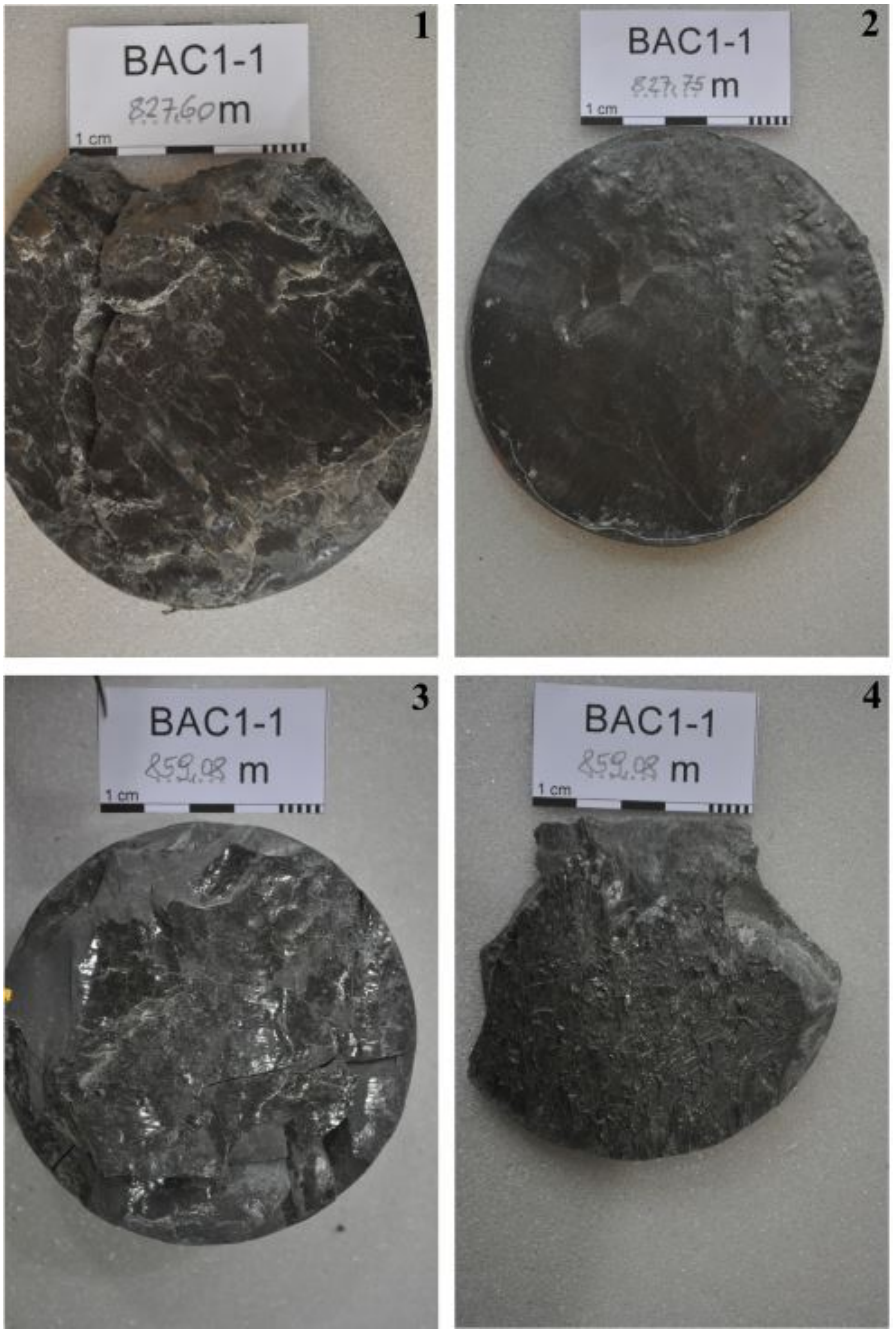

Figure 2.2: Top: Core photograph of sample BAC1-1 827.60 and 827.75. (1): Sub-parallel polished and striated slip surfaces with syn-kinematic calcite overgrowing the fault plane behind small releasing steps. The maximum length of fibers is about 7 mm (2): Finely striated fault plane with a knobby surface on one part.
Bottom: Core photograph of sample BAC1-1 859.08 (3): Closely-spaced shiny "mirror-like" slickensides combining to an anastomosing network. No growth of syn-kinematic fibrous minerals. (4): Rough knobby striated slip surface displaying multiple, up to 4 mm long steps. The orientation of steps is about perpendicular to the striation.
Adapted from Decker et al. (2022).

Out of the 15 pairs of fault rock and wall rock samples five pairs were selected from three different wells. All samples are from the Opalinus clay in order to obtain a homogeneous mineralogical composition of the samples. In addition, samples containing more material were preferred. In total, there are five wall rock and five fault rock samples, each in a depth ranging from 550 m to 859 m. All of the sampled faults and fault zones are shallow-dipping or sub-horizontal with SSW-NNE- or SSE-NNW-trending slickenlines (Decker et al., 2022). Available shear sense indicators such as fibrous mineralisation and ploughing clasts prove top-NNE- or top-NNW-directed slip (Decker et al., 2022). Fault slip data from the analysed fault zones are shown in the attachments A.2 and A.3.

The sample material, mostly consisting of mm- to about 1 cm sized rock fragments, was hand-sorted using tweezers under a Nikon stereo microscope with magnification ranging from 7.5x to 75x. Due to the shiny surface of the fault rocks, it was possible to distinguish fault rocks from wall rocks. Under the microscope, the contamination of the respective sample was removed to obtain clean samples of fault rock and wall rock.
High-resolution images from selected samples were taken using a Keyence digital microscope with a VH-ZST dual objective zoom lens (20x - 2000x). Consequently, surface roughness and scratches were observed using different illumination techniques and an optical shadow effect mode on the microscope. In addition, the lengths of grooves on two different slickensides were measured and statistically analyzed.

List of analyzed samples

Well	Rock Type	Core Depth	Formation	Digital Microscopes	SEM	Total Rock XRD	XRD Clay <2	XRD Clay <0.2	TOC/TIC	CEC
BAC1-1	**WR**	**828.28**	**OPA**			Y	Y		Y	Y
BAC1-1	**FR**	**827.52 - 828.28**	**OPA**	Y	Y	Y	Y		Y	Y
BAC1-1	**WR**	**834.89**	**OPA**			Y	Y	Y	Y	
BAC1-1	**FR**	**834.89**	**OPA**			Y	Y	Y	Y	
BAC1-1	**WR**	**859.08**	**OPA**			Y	Y		Y	Y
BAC1-1	**FR**	**859.08**	**OPA**		Y	Y	Y		Y	Y
RHE1-1	**WR**	**637.94**	**OPA**			Y	Y	Y	Y	
RHE1-1	**FR**	**637.94**	**OPA**		Y	Y	Y	Y	Y	
STA2-1	**WR**	**843.38**	**OPA**			Y	Y		Y	Y
STA2-1	**FR**	**843.38**	**OPA**	Y		Y	Y		Y	Y

Table 2.1: List of all samples and methods used for analysis: SEM = scanning electron microscopes, XRD = x-ray diffraction, TOC/TIC = total organic/inorganic carbon, CEC = cation exchange capacity; WR = wall rock, FR = fault rock; Name of the well: BAC1-1, RHE1-1, and STA2-1; Core depth in meters below surface; Samples for which the particular examination method was applied are marked with (Y)es. Sample BAC1-1 FR 827.52-828.28 can also be labeled with just one length in text and images.

2.2 Scanning electron microscopy

2.2.1 Ion milling and sample preparation

Samples were prepared for scanning electron microscopy (SEM) using the Broad Ion-Beam (BIB) technique. During this process, the sample is bombarded with Argon ions, which interact with the surface atoms of the sample. As a result, sample atoms get ejected (sputtering), and a smooth examination surface can be created. This polished surface is necessary to detect grain boundaries and microstructures. For the preparation, a Hitachi ArBlade 5000 broad ion beam polisher with an Ar ion beam was used. Each sample was milled for 2.5 to 3 hours at a beam energy of 8kV. Furthermore, some unpolished samples were used to analyse surface structures like slickensides and slickenfibres. Then, all samples were carbon coated using a Leica EM SCD500 high vacuum sputter coater. Some samples were coated from more than one side in order to prevent the charging of the specimens. SEM observations were done in an FEI Quanta 3D FEG operated at 10 kV. The same instrument was also equipped for energy-dispersive X-ray spectroscopy (EDS), making elemental analysis possible.

2.3 Bulk rock X-ray diffraction analysis

Each sample was ground by hand using an agate mortar and pestle, until a homogeneous powder with a particle size of approximately 5-10 μm was obtained. Between each grinding process, the mortar and pestle were thoroughly cleaned with deionized water and acetone to avoid any contamination of the sample.
The specimen was prepared for X-ray diffraction (XRD)-Analysis using a back-loading technique. The sample holder was clamped onto a preparation table and filled with the powder specimen. Then the powder was pressed using a powder press block. After the sample surplus was removed, the bottom of the sample holder was clamped onto the holder ring. Samples were measured using a Panalytical PW 3040/60 X´Pert Pro X-Ray diffractometer. XRD patterns were obtained using CuKα radiation at 40 kV and 40 mA with a scan step size of 0.00167° and a time of 5 s per step.

In order to obtain a quantitative analysis of mineral phases, it is necessary to prepare the samples with randomly oriented grains. For the platy clay minerals, this random orientation was achieved by using sandpaper on the sample surface. Finally, the samples were measured using the parameters specified above (40 kV and 40 mA). The quantitative interpretation of mineralogical composition was conducted using the method of Schultz (1964). For this method, the intensity (counts) of the main diffraction peaks were used and corrected with a specific factor.

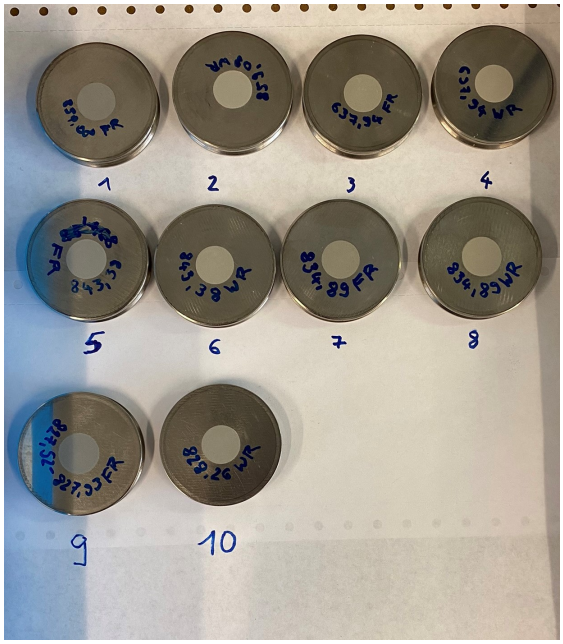

Figure 2.3: Sample holders for XRD analysis, filled with the powder specimen.

Principles of X-ray powder diffraction

X-ray diffraction can be used to determine the crystal structure and thus to identify mineral phases. The powder diffraction method is used to study clay minerals. X-rays are generated by heating a filament, which produces electrons. These electrons hit the anode and can remove the inner shell electrons of the anode material. Outer shell electrons can fill the vacancy, releasing characteristic X-rays. After monochromatization of the radiation, X-rays will hit the sample at different 2θ angles. Constructive interference occurs if the path difference is an integer multiple of the wavelength (Ewald, 1962). The relationship between wavelength λ, distance of crystal lattice d ,and diffraction angle 2θ can be described with Bragg's law (2.1).

$$n\,\lambda = 2d\,sin\theta \tag{2.1}$$

Resulting patterns are plotted as intensity versus different angles 2θ.

2.4 Clay mineral analysis

$< 2\ \mu m$ Fraction

To start with, 13 g of each sample was chemically treated with a mixture of 200 ml $H_2O_2 : H_2O = 1 : 1$ for a period of seven days. During that time, the samples were stirred several times. H_2O_2 can oxidize organic material in the samples following the simplified reaction $C + 2H_2O_2 \longrightarrow CO_2 + 2H_2O$.

After the reaction stopped, the suspensions were treated with an ultrasonic probe, operating at 400 W, for 2 minutes. Then, the dispersed samples were poured into an Atterberg-cylinder and filled with deionized water until a 30 cm water column was reached. To prevent aggregation/flocculation during sedimentation, a spatula-tip sodium triphosphate was added.
The sedimentation velocity can be calculated according to Stokes (1851) as follows:

$$V = \frac{2}{9}\,\frac{(\rho_p - \rho_f)\,g\,a^2}{\eta} \tag{2.2}$$

Hence the sedimentation velocity V depends on the specific mass of colloidal material ρ_p and fluid ρ_f, earth's acceleration g, the radius of the particles a and the viscosity of the fluid η. However, clay minerals are flaky and heterogeneous which must be taken into account when calculating the sedimentation time (Gee and Or, 2002). Therefore the settling time for $< 2\ \mu m$ clay particles in a 30 cm water column is 24 hours and 33 minutes at a room temperature of 20 °C (Köster, 1964).

After that time, particles with a size coarser than $2\mu m$ are settled to the bottom

of the cylinder due to their higher settling velocity. The fraction that remained in the suspension was drained into a bowl (Figure 2.4). Thereafter, the suspensions were dried in the oven at 40 °C. Next, the dried clay was ground with an agate mortar and pestle, until a homogeneous powder was achieved. For each sample, two centrifuge tubes were filled with 50 mg of the sample. One centrifuge tube was filled with KCl, and the other with $MgCl_2$. The resulting concentration of the clay suspension was 1 mg/ml. Saturated samples were rotated in an overhead shaker for 23 hours. Then samples were centrifuged for 5 minutes at 1500 revolutions per minute (rpm). After the remaining liquid was drained, the centrifuge tubes were filled with deionized water, shaken, and centrifuged again for 10 minutes at 4000 rpm. As a result of this, excess KCl and $MgCl_2$ were removed. Finally, the vessel was filled with 5 ml deionized water, ultrasonically disaggregated (1 min, 21 % amplitude), and pipetted onto petrographic glass slides. For each K- and Mg-saturated sample, two slides containing 1 ml of the suspension (with a clay concentration of 10 mg/ml) were prepared and air-dried (Figure 2.5).

Figure 2.4: Atterberg-cylinder with drained $< 2\ \mu m$ fraction on the left, and with $< 2\ \mu m$ fraction still in suspension on the right. Particles that exceed $2\ \mu m$ are on the bottom of the cylinder.

$< 0.2\ \mu m$ fraction

In order to analyse mixed-layer minerals like illite/smectite (I/S), it is necessary to obtain a finer ($< 0.2\ \mu m$) clay fraction. In the beginning, the remaining $< 2\ \mu m$ clay fraction was dissolved in deionized water. Thereafter, the samples were ultrasonically dispersed at 400 W for 2 minutes. Then each sample was filled in a centrifuge bottle and topped with deionized water to the 600 ml marking. This marking represents a specific water column, which must be considered for the calculation of centrifuge rpm and operating time. For this study an operating time of 16.3 min at 3800 rpm was calculated specifically (Tanner and Jackson, 1948). This calculation relies on Stokes'law (2.2), with consideration of higher gravity determined by rotational speed and radius of the centrifuge. Afterwards, the fraction that stayed in suspension ($< 0.2\ \mu m$) was filled in a bowl and dried. The remaining clay fraction was dispersed in water and centrifuged again, in order to obtain more fine clay fraction. For each sample, a centrifuge tube was filled with 25 mg of the clay fraction. Every centrifuge tube was treated with 25 ml $MgCl_2$. The tubes were rotated in the overhead shaker for 23 hours and prepared like the $2\ \mu m$ fraction afterwards. This time only 2.5 ml deionized water was used to reach the concentration of 10 mg clay per ml water.

Due to the fact that the already ground $< 2\ \mu m$ fraction was used, a reduction in particle size may have occurred. This reduction prevented the separation of finer mixed-layer minerals from coarser clay minerals like illite and chlorite. Therefore, the experiment was repeated using original sample material.

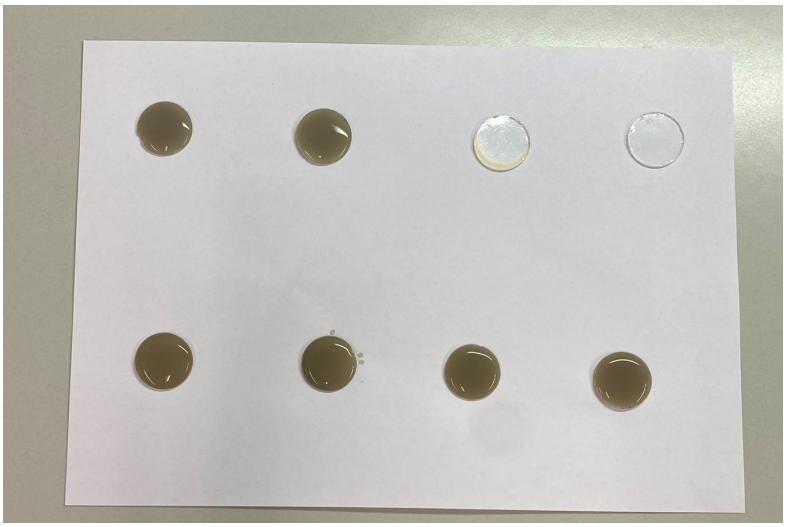

Figure 2.5: Preparation of the clay fraction on glass slides (containing 1 ml of the clay fraction) for XRD measurement.

Identification of clay minerals

In order to identify clay minerals, a special pre-treatment of the specimens with KCl and $MgCl_2$ is necessary. In the absence of this treatment, the basal spacing of smectite can vary from 10 to 20 Å, making the interpretation of the XRD patterns difficult (Borchardt, 1989). For example, a Mg-saturated smectite shows a peak at 15 Å at 54 % relative humidity. After saturating the sample with ethylene glycol (EG), this peak will shift to 17 Å because of expansion. A Mg-saturated vermiculite has a peak at 14 Å, whereas a saturation with K would produce a peak at 10 Å (Douglas, 1989). Non-swelling minerals like illite and chlorite are not affected by these treatments and have constant peaks at 10 Å for illite, and 14 Å for chlorite. Kaolinite is identified by the peak at 7.2 Å, which can be eliminated by heating at 550°C (Dixon and Weed, 1989).
For the identification of mixed-layer clay minerals, it is useful to treat the samples with EG. The most common mixed-layer clay mineral is illite/smectite (I/S) (Moore and Reynolds Jr, 1989). In order to identify these minerals, the method of Mering (1949) can be used, in which reflections between the position of the 001 peaks of both mineral end members of the mixed-layer mineral are used (Moore and Reynolds Jr, 1989). As the illite content in the mixed-layer mineral increases, the peak position will move to a higher 2θ angle (Moore and Reynolds Jr, 1989). Calculated mixed-layer mineral patterns from (Moore and Reynolds Jr, 1989) were used to quantify measured samples.

2.5 Total carbon

Total carbon (TC) is the sum of total organic carbon (TOC) and total inorganic carbon (TIC). Organic carbon is formed by the decomposition of plants and animals, whereas inorganic carbon originates mainly from carbonates such as calcite ($CaCO_3$), and dolomite ($CaMg(CO_3)_2$). Organic carbon will decompose between 150 °C to 450 °C, and inorganic carbon below 1000 °C (Leco-Corporation, 2018). With this assumption, it is possible to measure TOC and TIC. This temperature-dependent method does not require any pre-treatment of the samples. Samples were measured using the Leco RC612 Multiphase Determinator. For the calibration, the reference material Leco LCRM 502-902 Carbon % 11.99 ± 0.05, 502-905 Carbon % 4.99 ± 0.05, and 502-696 Carbon % 1.02 ± 0.03 was used

For analysis, 0.100 g (± 0.0005 g) of finely ground samples were weighed into a clean crucible. This procedure was done twice for each specimen to avoid any errors and to increase accuracy. Finally, the crucible was placed into the appropriate auto-loader. The measurement was performed automatically. The samples were inserted into the combustion tube of the furnace. Thereafter, the produced gas flows through an afterburner furnace and furnace catalyst. Finally, the gas gets measured by a solid-state infrared detector.

2.6 Cation exchange capacity

The surface of clay minerals is usually negatively charged and can therefore attract cations. Exchangeable cations between the silicate layers can be measured as milliequivalents (mEq) per 100 g (Murray, 2006*b*). The cation exchange capacity (CEC) depends on the type of clay mineral. Illite and chlorite have an exchange capacity of 10-40 mEq per 100 g, and kaolinite 3-15 mEq per 100 g, whereas the exchange capacity of smectite is much higher with 80-150 mEq per 100 g (Grim, 1968). A high cation exchange capacity is indicative of a high smectite content. The cation exchange capacity of clay loam ranges from 15 to 30 mEq per 100 g, and for pure clay it is more than 30 mEq per 100 g.
The cation exchange capacitity was determined using a Cu(II) ethylendiamine complex, and measured using a Spectroquant Prove 300 UV/VIS spectrophotometer at a wavelength of 585 nm (Figure 2.6). Clay minerals have a high affinity for Cu, and therefore ion concentration decreases in the solution after exchange (Meier and Kahr, 1999). The light absorption decreases with decreasing ion concentration in exchanging solution, which can be measured with the spectrophotometer.

Cu(II) ethylendiamine complex was prepared, dissolving 1.463 g of triethylenetetramine in 100 ml deionized water and 1.596 g of Cu(II) sulfate in 1 l water (Meier and Kahr, 1999). Then both solutions were mixed together. First, 200 mg ($\pm$ 0.5 mg) of each clay specimen ($< 2\ \mu m$) was put into a beaker. Next, 50 ml of deionized water was added and samples were stirred for 2 minutes and ultrasonically dispersed for one minute. After adding 10 ml of Cu(II) ethylendiamine complex to each sample, all samples were stirred for another 3 minutes and then transferred to centrifuge tubes. The samples were centrifuged for 10 minutes at 4000 rpm, and afterwards filled into a beaker. The sample liquid was filled into a 20 mm rectangular sample cell and measured 5 times with the spectrophotometer. To avoid any cross contamination the cuvette was rinsed two times between each measurement. Furthermore, a blank value with deionized water and a reference value with a standard sample (Hennersdorf) was measured.
The CEC can be calculated from the measured absorbance (extinction) according to (Meier and Kahr, 1999) as follows:

$$CEC_{(mmol/100g)} = (Eb - Em)\,\frac{100}{Eb} \tag{2.3}$$

Therefore, the CEC in mmol/100g depends on Eb = Extinction without sample and Em = Extinction of the sample solution (Meier and Kahr, 1999). For the standard sample (Hennersdorf), 500 mg of sample material was used, and therefore the result was divided by 2.5.

Figure 2.6: Spectrophotometer with Cu-complex solution of samples. Differences in ion concentration are measured with the Spectrophotometer.

Chapter 3

Results

3.1 Digital surface images

With the high-resolution digital microscope, the sample surface is clearly visible, and fault rocks can be recognized without doubt. All samples have a fine-grained texture and dark grey color; however, the surface of all wall rocks appears coarse-crystalline. It is noticeable that all fault rocks (Figure 3.1a) have a shiny surface with high topography, whereas the surface of the undamaged rocks (Figure 3.1b) appears dull and homogeneous. At a high magnification of the fault rocks, steps, striated ridges and grooves are visible, which can be used to identify the direction of movement (Figure 3.2, Figure 3.3).

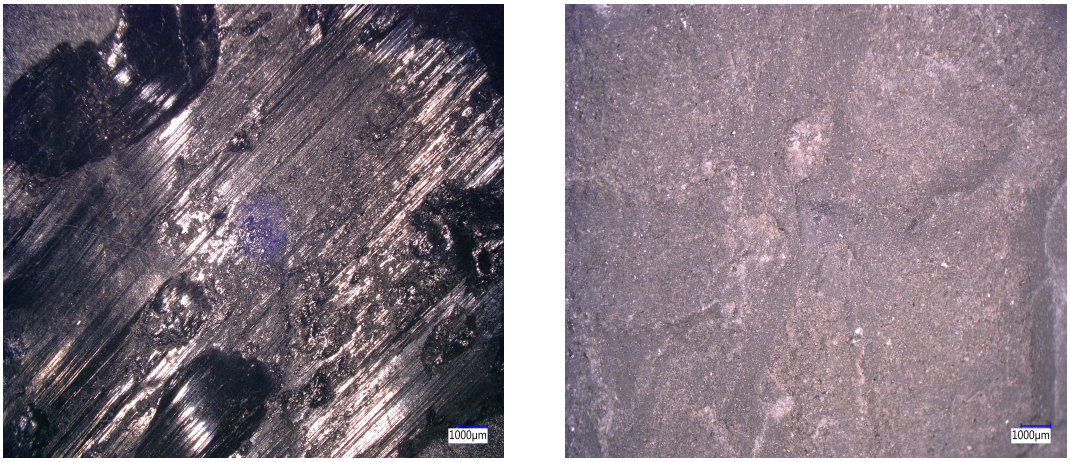

(a) Slickenside on fault rock **(b)** Wall rock

Figure 3.1: High-resolution image from sample pair STA2-1 843.89, shows clearly the difference between fault rock and wall rock in top view. Further, parallel grooves on fault rock (Figure 3.1a) are visible. All fault rock samples are characterized by their glossy surface.

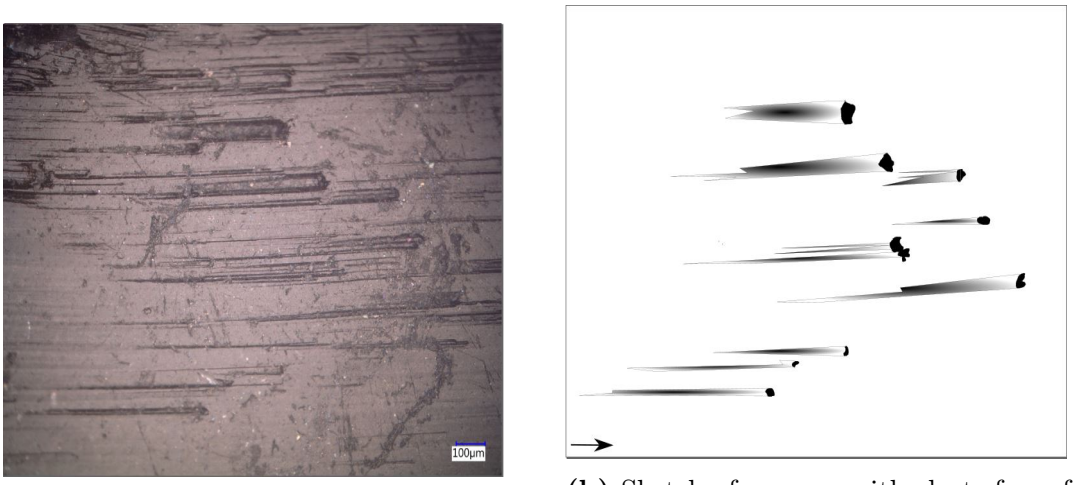

(a) Fault rock with grooves.

(b) Sketch of grooves with clasts from fault rock (left picture).

Figure 3.2: Magnified image of fault rock (sample STA2-1 843.38 FR) shows deep groves. The black arrow indicates the direction of movement from the missing block. The presence of clasts at the end of each groove cannot be confirmed due to the low image resolution, but the shape of the grooves indicates the direction of movement.

The grooves on two different slickensides from the sample STA2-1 843.38 FR show substantial variation in length. The beginning and end of each groove are clearly visible and can be measured precisely, but in areas with high groove density, grooves can overlap and can not be measured accurately (Figure 3.4). The statistical analysis of the two slickensides from sample STA2-1 843.38 FR shows that the length varies between 559 μm and 2588 μm with a mean of 1467 μm for one specimen (Figure 3.5a) and between 25 μm and 217 μm with a mean of 123 μm for the other one (Figure 3.5b). The slickensides from sample BAC1-1 827.52 FR are quit similar with a length between 525 μm and 4022 μm and a mean of 1924 μm for one sample (Figure 3.6a) and a length between 751 μm and 3442 μm with a mean of 2072 μm (Figure 3.6a) for the other one.

Furthermore, all slickensides show a different distribution in groove length (Figure A.8, Figure A.9, Figure A.10 and Figure A.11) .

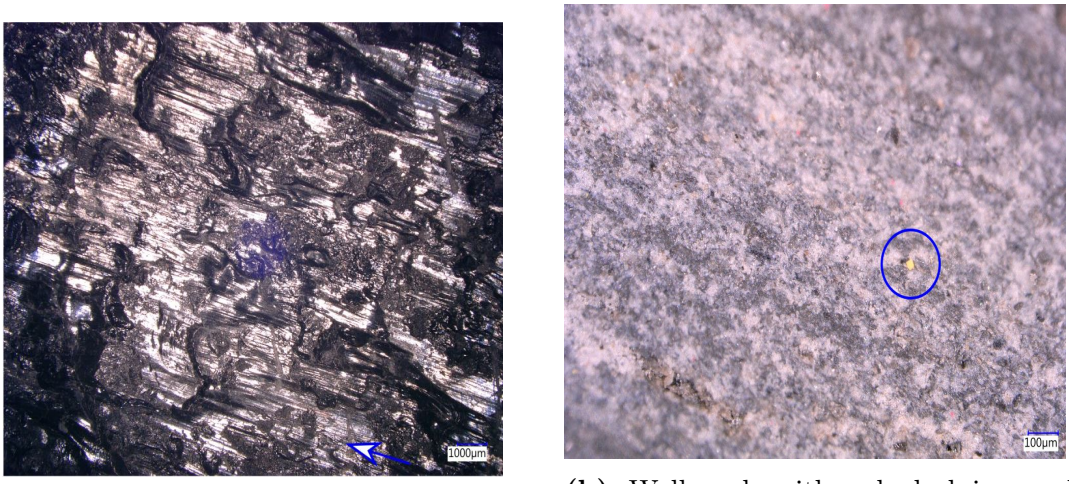

(a) Fault rock with slickenside risers

(b) Wall rock with euhedral iron sulfide crystal (blue circle).

Figure 3.3: Slickenside risers on fault rock (sample BAC1-1 859.08 FR) are perpendicular to the shear direction. The blue arrow indicates the direction of movement from the missing block. Wall rock (sample BAC1-1 834.89 WR) has a dull, coarse-crystalline surface.

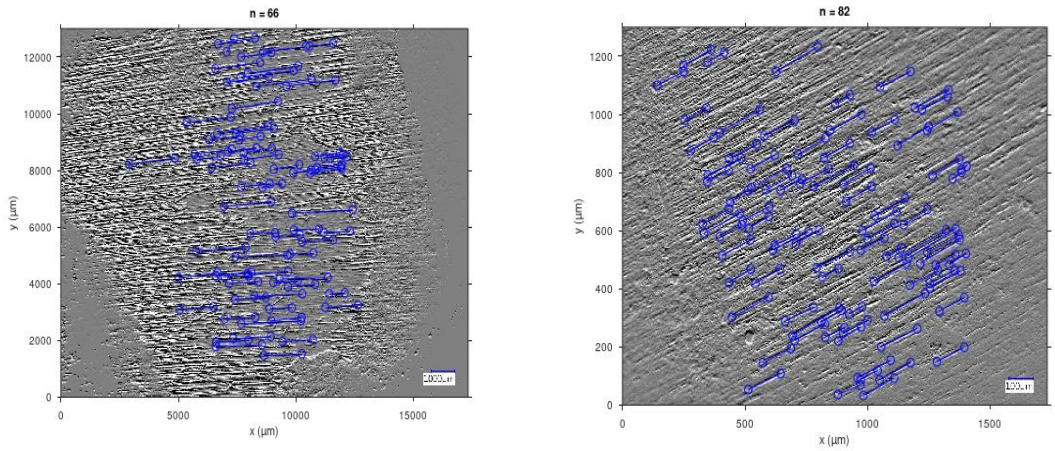

(a) Sample with long grooves.

(b) Sample with short grooves.

Figure 3.4: Surface roughness image of mapped grooves from sample STA2-1 843.38 FR. Blue lines indicate the selected objects. X- and y-axis each show the length in micrometers.

A direct comparison of the groove length with other specimens shows that most grooves have a length between 1000 μm and 2500 μm (Figure 3.5a and Figure 3.6). Only one sample (Figure 3.5b) has significantly shorter grooves, with most grooves ranging between 100 μm and 150 μm. All measured data are right-skewed. Due to high groove density and insufficient exposure of the shear surface, it was not possible to collect more data about groove length from other samples.

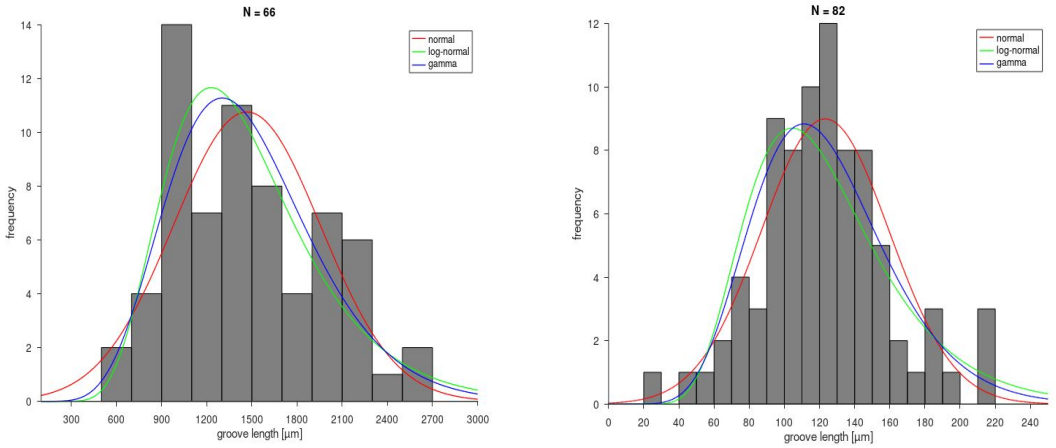

(a) Distribution of lengths of long grooves. **(b)** Distribution of lengths of long grooves.

Figure 3.5: The histograms show the distribution of mapped grooves from sample STA2-1 843.38 FR. Both distributions are right-skewed. Data set Figure 3.5a is gamma distributed or log-normally distributed, whereas data set Figure 3.5b with short grooves is normally distributed.

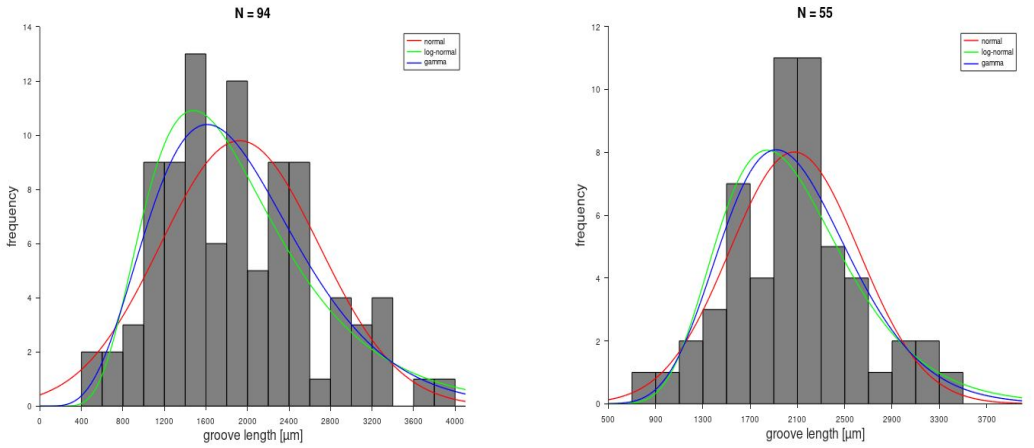

(a) Distribution of groove length. **(b)** Distribution of groove length.

Figure 3.6: The histograms show the distribution of mapped grooves from sample BAC1-1 827.52 FR. Both distributions are right-skewed. Data set Figure 3.6a is gamma distributed distributed, whereas data set Figure 3.6b is normally distributed.

	Histogram Figure 3.5a		Histogram Figure 3.5b	
	Groove length	**Log groove length**	**Groove length**	**Log groove length**
Range	2029.56	1.5324	192.0544	2.1644
Mean	1467.0162	7.2341	123.239	4.7641
Median	1336.457	7.1978	122.7449	4.8101
Skewness	0.38637	-0.25613	0.24803	-1.4141
Kurtosis	2.2692	2.5229	3.5838	7.5407

Table 3.1: Properties of statistical distributions of two samples from STA2-1 843.38 FR (Figure 3.4a and Figure 3.4b). Note the mean groove length between both samples varies by a factor of eleven.

	Histogram Figure 3.6a		Histogram Figure 3.6b	
	Groove length	**Log groove length**	**Groove length**	**Log groove length**
Range	3496.8185	2.0358	2690.9568	1.5221
Mean	1924.8006	7.4792	2072.6493	7.5996
Median	1844.6489	7.5199	2083.7406	7.6419
Skewness	0.56486	-0.48405	0.26887	-0.76197
Kurtosis	2.9612	3.1444	3.2526	4.4395

Table 3.2: Properties of statistical distributions of two different slickensides from sample BAC1-1 827.52 FR. Note that both slickenside have similar statistical properties.

3.2 Scanning electron microscopy

Looking at the samples with a higher magnification, several details, such as single grains and grain-boundaries, shear zones, and fractures, become visible. Due to the unidirectional carbon coating of the specimens, some irregular parts like pores, cracks, and edges are less conductive and, therefore, visible in a lower resolution. Besides, oblique striations resulting from the ion milling makes identifying microstructures rather difficult.

3.2.1 Surface view on slickensides

Slickensides are recognizable by their shiny surface. However, the high topography makes it difficult to analyse them with the SEM. As on small scale, kinematic indicators such as grain traces are also visible on a bigger scale. Lateral breakouts at these grooves show the direction of movement.
Further, every slickenside surface is covered with nanometer-sized clay particles, which represent the remains of crushed large clay minerals. Sometimes heavier minerals such as celestite or pyrite, (which appear brighter) can shine through this layer of clay minerals (Figure 3.7 - Figure 3.9).

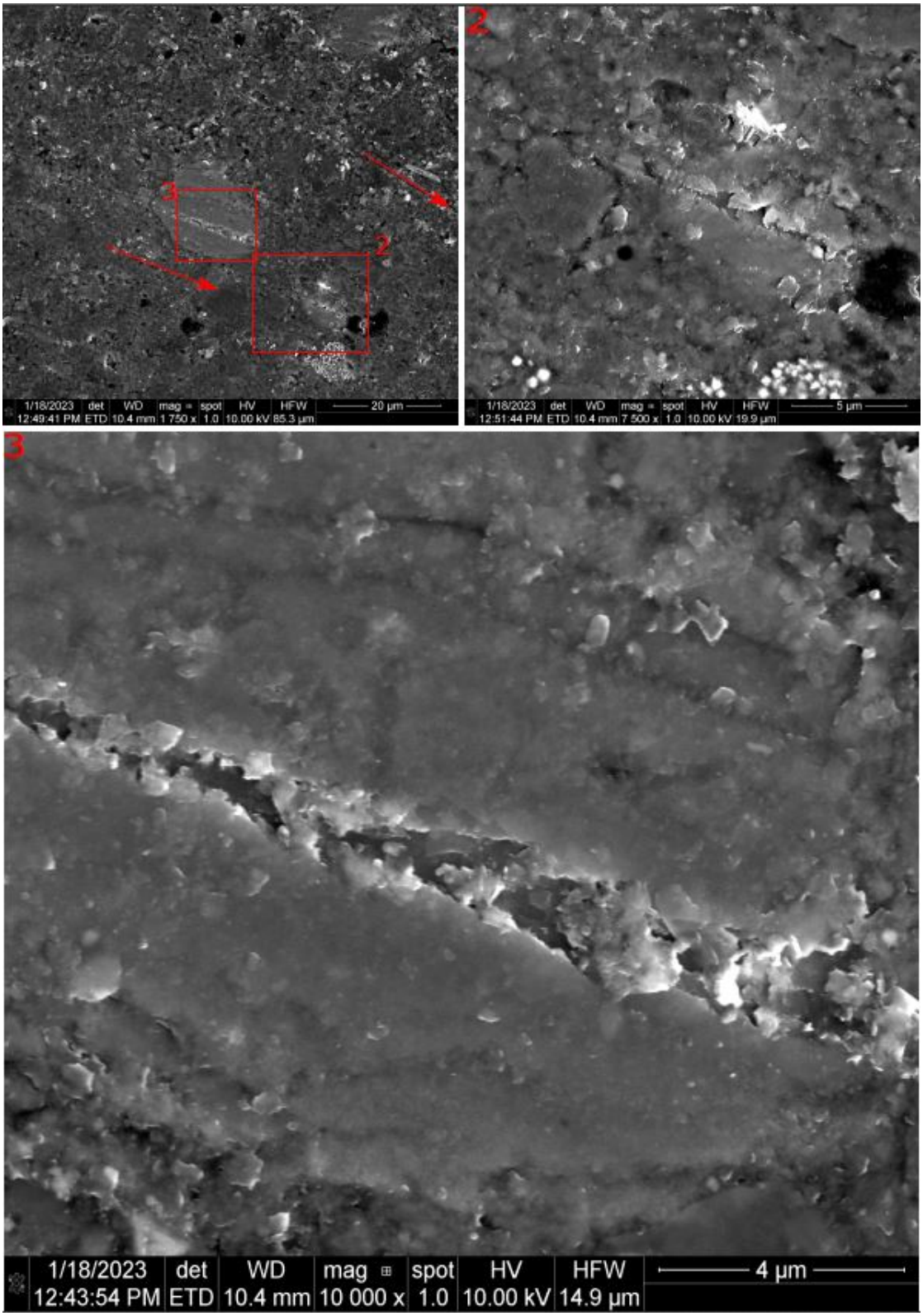

Figure 3.7: SEM images in orthogonal view of a slickenside of the sample BAC1-1 859.08 FR. Two grooves with different directions make a 15° angle. Images 2 and 3 are insets of top left image, showing a large mica crystal with a groove across. Note, that whole slickenside surface consists of fragments of larger mica crystals, which are mechanically disintegrated during the displacement process. Red arrows show the movement of the missing block.

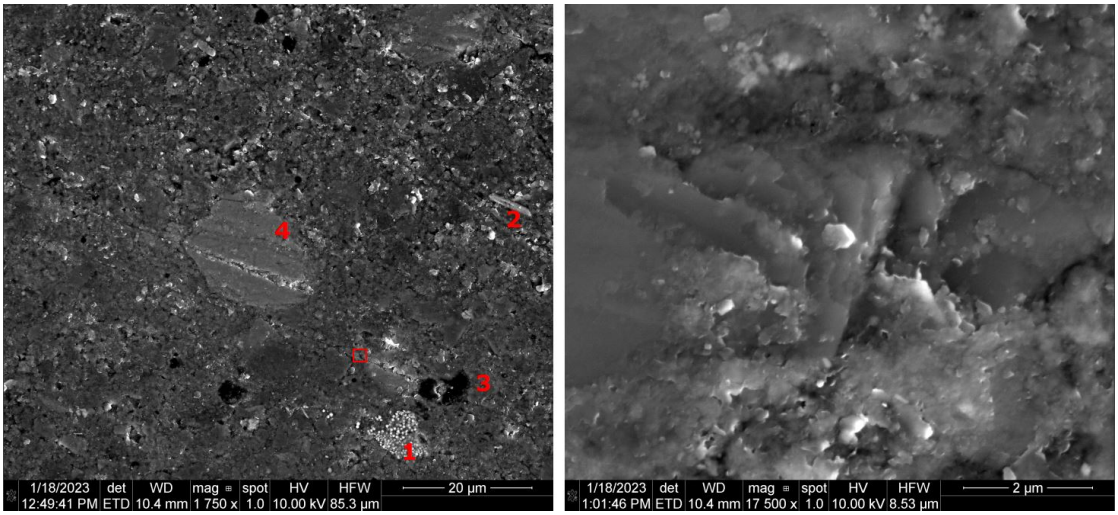

Figure 3.8: SEM images in orthogonal view of a slickenside of the sample BAC1-1 859.08 FR. Right image is located within the red rectangle. Whole sample is covered with nanometer-sized clay particles, below this layer are: (1) euhedral pyrite crystals which form pyrite framboids; (2) euhedral celestite crystals with typical prismatic crystal habit. (3) Dark spots are organic matter or pore space.

One sample (RHE1-1 639.94 FR) is covered with spherical nano-particles with a size of less than 250 nm (Figure 3.9). This nano-particle layer varies in thickness and particle shape across the slickenside surface, and does not show any signs of deformation. As a result of this, there are areas where the heavier celestite crystals from underneath are visible. Also, a preferred celestite orientation can be diagnosed on the slickenside surface. Looking at another part of this sample, the nano-particle cover gets thicker, and single particles become more spherical. Additionally, not only the slickenside surface but also pore spaces are covered by nano-particles.

In the SEM image of sample BAC1-1 859.08 FR there is also multi-branching tree-like patterns on the slickenside surface (Figure 3.10). These crystal aggregates show dendritic shapes. Unfortunately, accurate EDX measurement of these dendrites is not possible, because the interaction volume of the spot is too large.

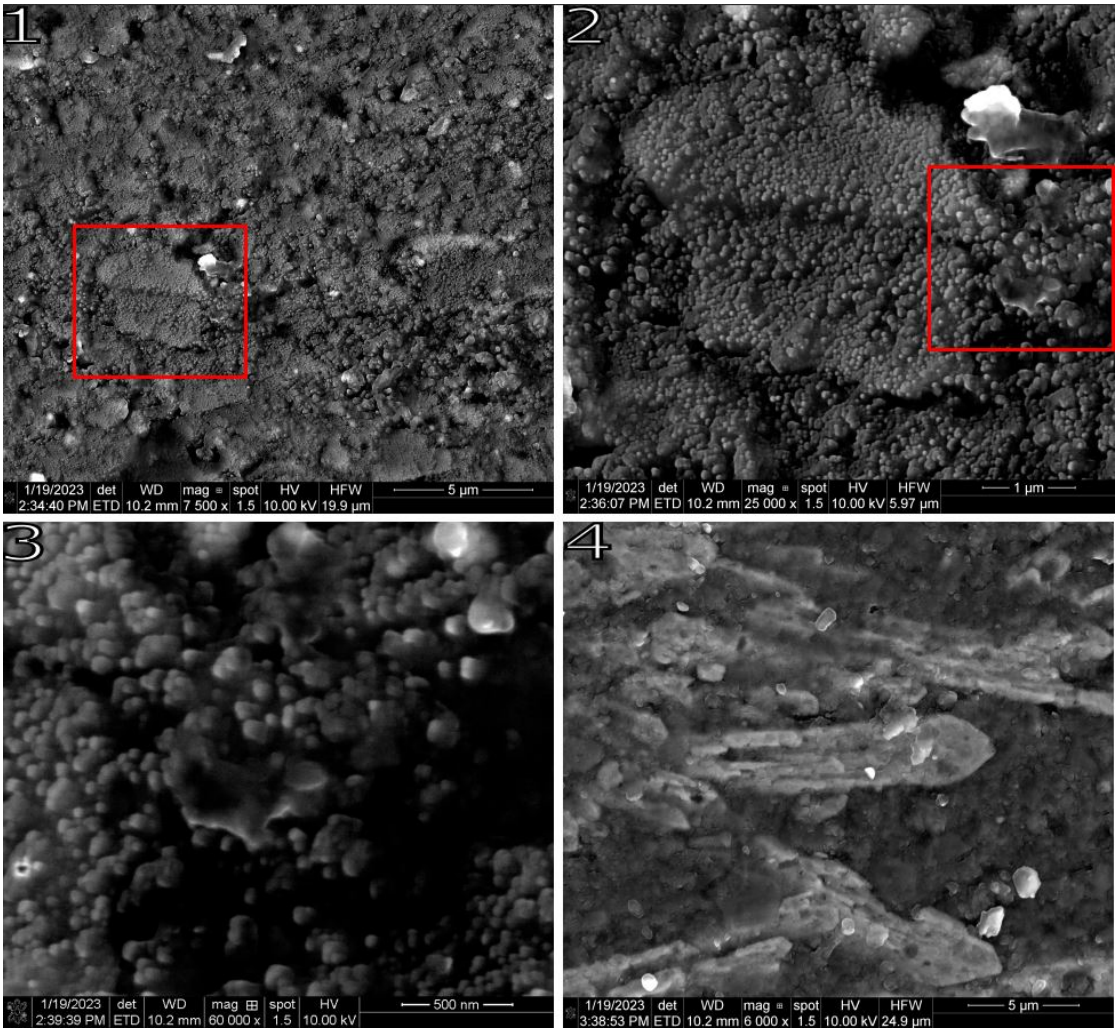

Figure 3.9: SEM images in orthogonal view of a slickenside of the sample RHE1-1 639.94 FR. Slickenside is completely coverd with spherical nano-particles. (2) is enlargement of a part of the image shown in (1), showing biotite crystal covered with nano-particles. (3) is an inset of (2), showing pore space, with nano-sized particles. (4) at the same specimen there are areas with less developed particles, below this particle layer are euhedral celestite crystals.

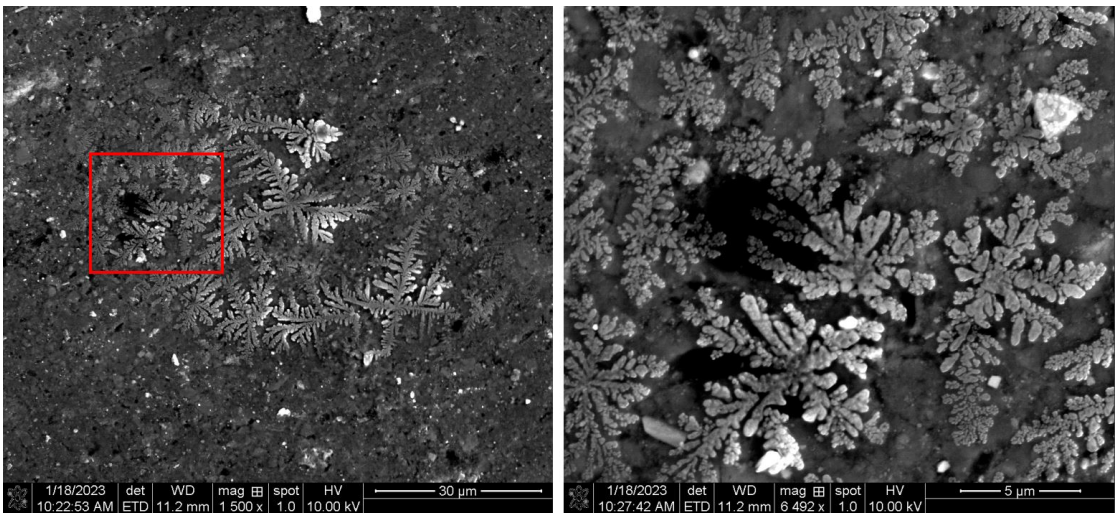

Figure 3.10: SEM images in orthogonal view of a slickenside of the sample BAC1-1 859.08 FR, showing tree-like patterns (dendrites) with a maximum extension of 30 μm . Right image is located within the red rectangle, showing dendrites growing from the pores out to the slickenside. There is no preferred direction of growth visible on the slickenside surface.

3.2.2 View on polished surface

All BIB-milled specimens are cross-sections parallel to the kinematic indicators. First, analysed samples are characterised by open fractures parallel to the shear plane. These fractures have a maximum aperture width of less than 5 μm and do not have any sedimentary or mineral filling. Besides, all fractures follow the direction parallel to the bedding and do not cut through individual mineral grains. Further, some fractures form boundaries between different textures, such as areas with coarse and fine grains. Hence, the boundary between carbonate-rich and clay-rich areas within the upper part of the sample is very sharp.
Further, in one sample cross section (RHE1-1 637.94), a homogeneous layer of celestite on the shear surface is visible. Below this layer, there is a sharp transition to the underlying carbonate-rich minerals. In some places, there are also prismatic celestite crystals, which are apparently aligned parallel to the fault surface (Figure 3.14b). Overall, the most common minerals are stacked platy clay particles, that do not show any sign of tectonic deformation, but are bent around larger homogeneous quartz and calcite grains (Figure 3.11 - Figure 3.14). Between these stacked clay minerals are large grains of quartz, calcite, pyrite, siderite/dolomite and feldspar. In addition, all samples contain evenly distributed organic matter, in various sizes and shapes (Figure 3.11 - Figure 3.14). Another notable feature is the abundance of pyrite, which appear brighter due to the presence of elements with a higher atomic number. Pyrite occurs as large grains, small euhedral micro-crystals, and pyrite clusters so-called framboids (Figure 3.14).

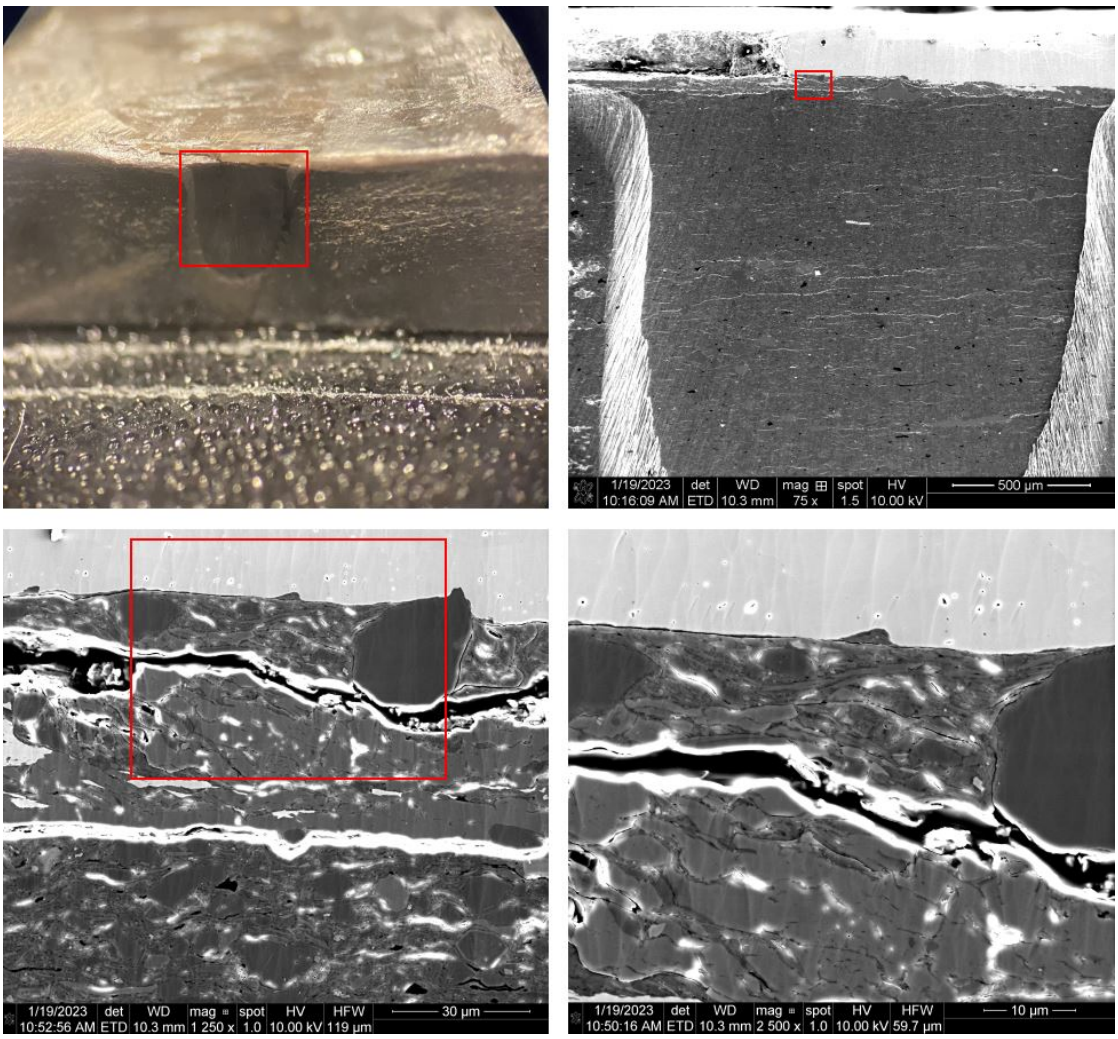

Figure 3.11: Top left image shows sample RHE1-1 637.94 FR under a stereo dissecting microscope. Note polished cross-section with an extension of 1 mm^2. The cross-section is oriented parallel to the macroscopic slickenline. Image to the right shows the polished surface under the SEM. Bottom images are magnified sections, showing massive celestite on top of the slickenside. Below this celestite layer is a horizon with carbonates, and isolated quartz grains, which is separated by a fracture from the underlying clay rich horizon.

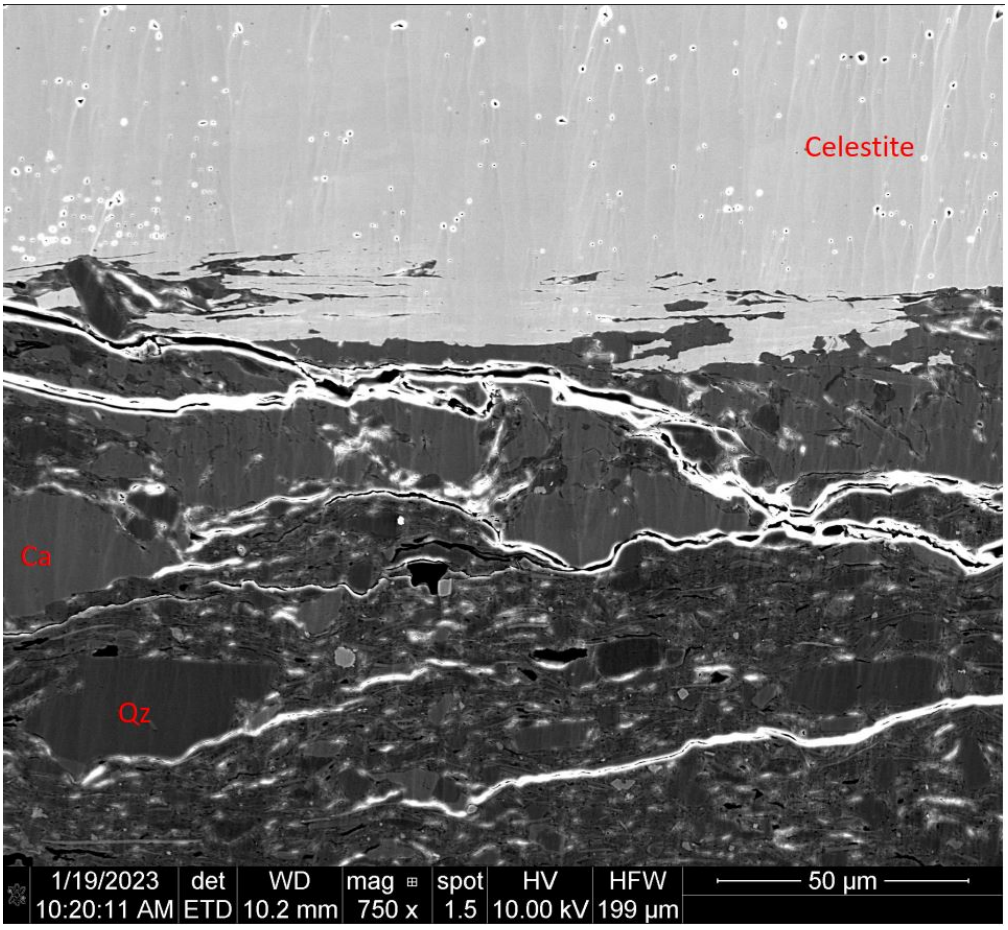

Figure 3.12: Image shows sample RHE1-1 637.94 FR under the SEM. Ca = calcite; Qz = quartz; The top of the slickenside is covered by celestite. Between the massive celestite and the carbonates are isolated (tabular) celestite crystals visible. Note that there are no shear sense indicators visible.

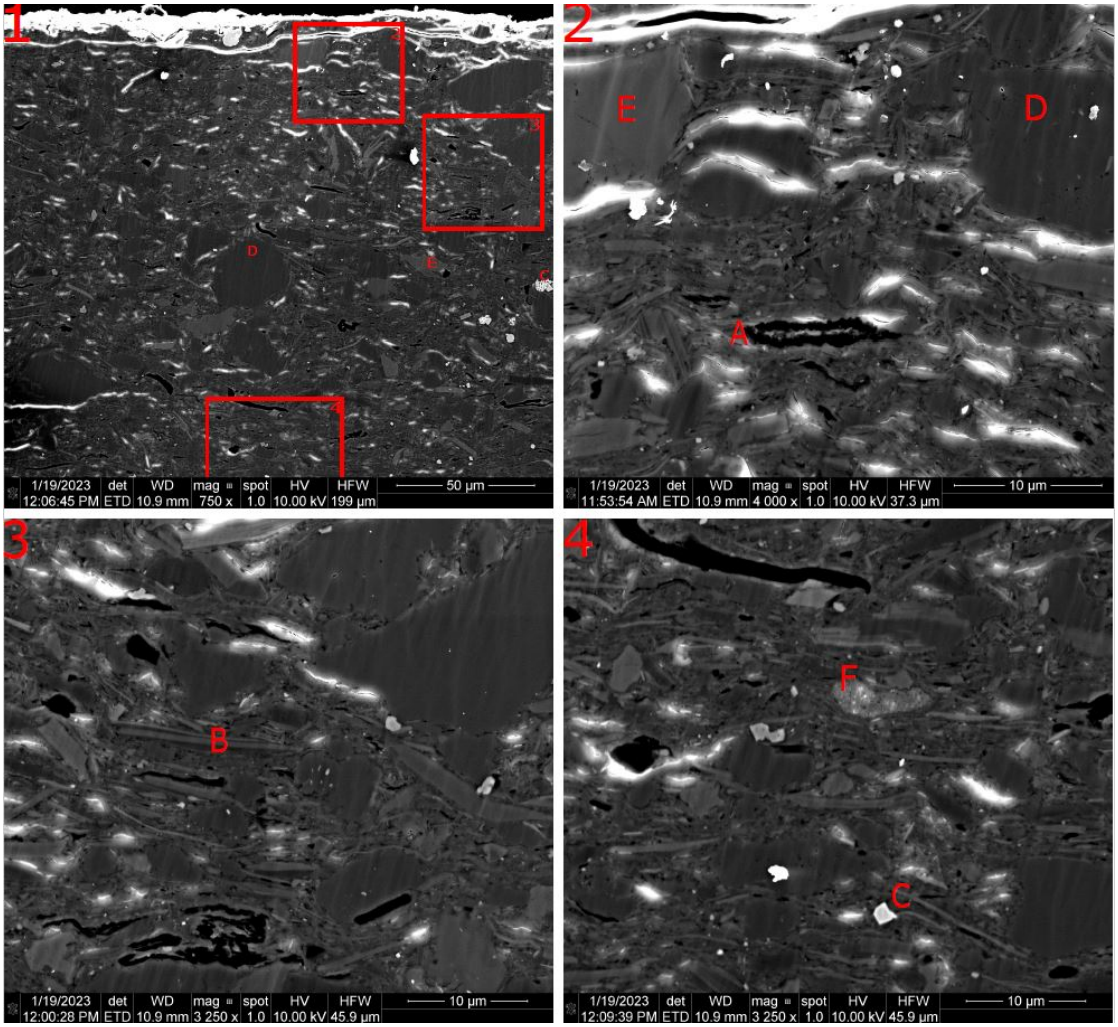

Figure 3.13: Top left image (1) of sample shows overview of sample BAC1-1 827.52 cut parallel to slickenline. (2) is a magnified image of upper part of the sample contains big calcite (E) and quartz (D) grains. Organic material (A) shows deformation by compaction due to overburden. (3) is a magnified image of lower part of the sample. Clay minerals in lower part of the sample (3) and (4) seem to be less disturbed than clay minerals in the upper part (2). Further, pyrite (C) and fossil remnants are visible in some areas of the sample. Vertical striation on all images is a results of sample preparation.

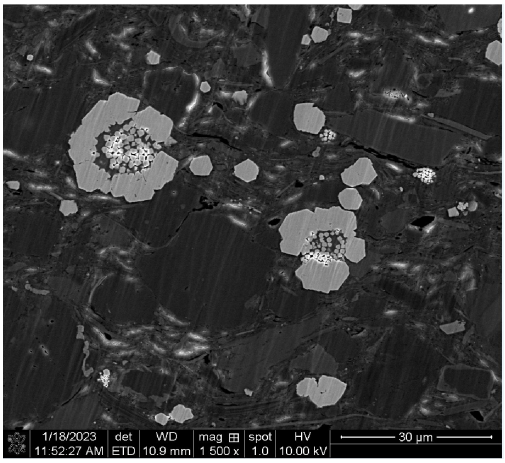

(a) Transition from pyrite framboids to coarser crystals of pyrite.

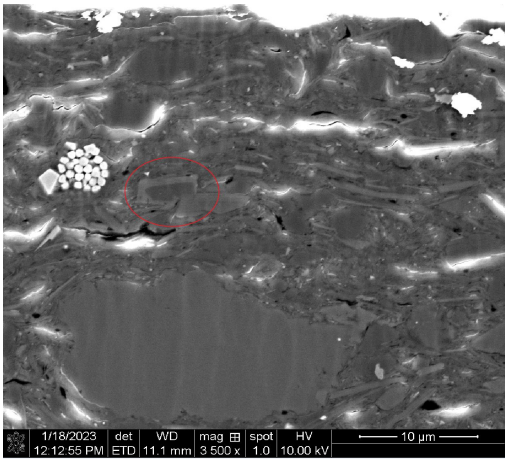

(b) Dolomite with Fe-rich overgrowth (ankerite)

Figure 3.14: SEM images of sample BAC1-1 827.52 showing pyrite and dolomite.

3.3 Mineralogy of whole rock samples

To determine variations in the mineralogical composition, X-ray diffraction patterns of fault rock and wall rock samples are compared below (Figure 3.15 - Figure 3.18). The XRD analysis shows, that all samples consist of the same minerals. The major components of the Opalinus Clay are: clay minerals (kaolinite, chlorite), quartz, carbonates (calcite, ankerite and siderite), feldspars (albite, microcline), sulphides (pyrite) and mica (muscovite). These minerals can be found in all samples, however, pyrite seems to be the least abundant mineral. The sample BAC1-1 828.26 FR has the highest pyrite concentration of all samples. Similarly, the wall rock part from this sample also contains a higher pyrite concentration than other wall rock samples (Figure 3.18). The lowest pyrite concentration can be found in the fault rock samples BAC1-1 834.89 FR, RHE1-1 637.94 FR and WR and STA2-1 843,38 FR, where it is present only in traces. Furthermore, siderite and ankerite can be found in low concentrations in all samples. Two sample pairs (RHE1-1 637.94 and STA2-1 843.38) show a higher amount of siderite, than the rest of the analyzed samples. The siderite concentration of sample STA2-1 843.38 WR is more than 17 %, and therefore, remarkably high.

Quantitative analysis shows that the composition of all samples consists of 21 % to 38 % quartz, 2% to 3 % k-feldspar, 2% to 3 % plagioclase, 5 % to 18 % calcite, 1 % to 2 % ankerite, 0 % to 17 % siderite, 0 % to 4 % pyrite, and 40 % to 62 % clay minerals (Figure 3.18). A closer look at adjacent sample pairs shows that there is no noticeable difference in mineralogical composition between fault rock and wall rock samples. However, most fault rock samples contain slightly less quartz but more clay minerals.

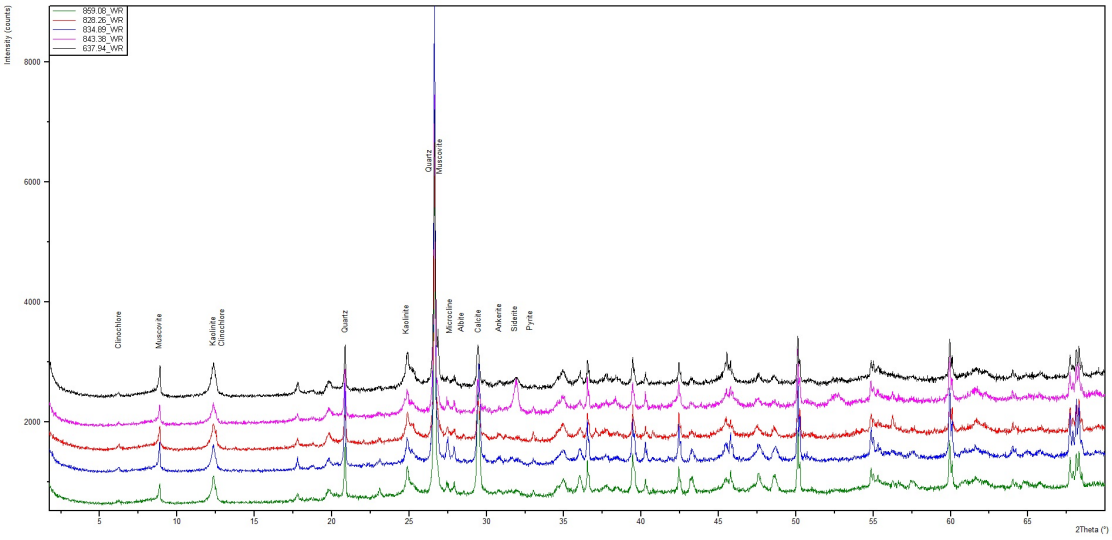

Figure 3.15: Whole rock XRD patterns of all **wall rock** samples. The direct comparison shows that there is no difference in mineralogical composition between these samples. All samples contain: chlorite, muscovite, kaolinite, quartz, microcline, albite, calcite, ankerite, siderite, pyrite;

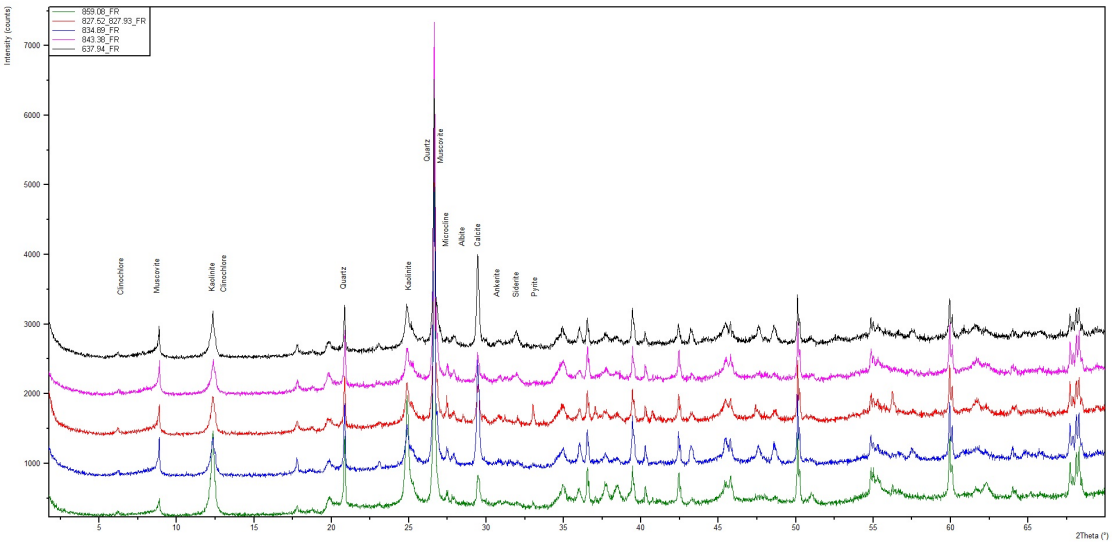

Figure 3.16: Whole rock XRD patterns of all **fault rock** samples. Note that there is no variation in mineralogical composition between different fault rock samples. All samples contain: chlorite, muscovite, kaolinite, quartz, microcline, albite, calcite, ankerite, siderite, pyrite;

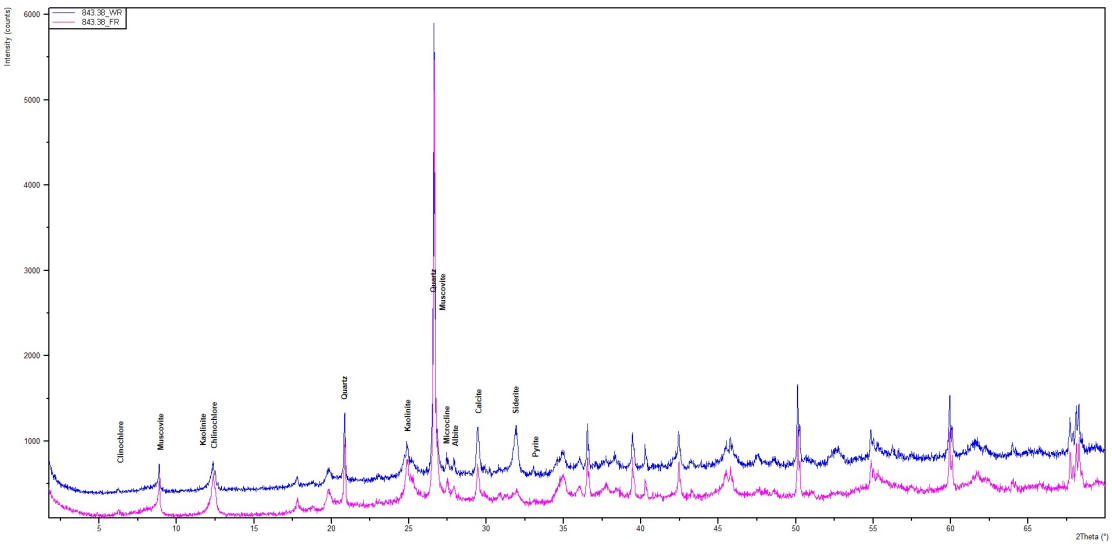

Figure 3.17: Whole rock XRD patterns of sample STA2-1 843.38 shows no deviation in mineralogical composition between wall rock (upper blue pattern) and fault rock (lower pink pattern). All samples contain: chlorite, muscovite, kaolinite, quartz, microcline, albite, calcite, ankerite, siderite, pyrite;

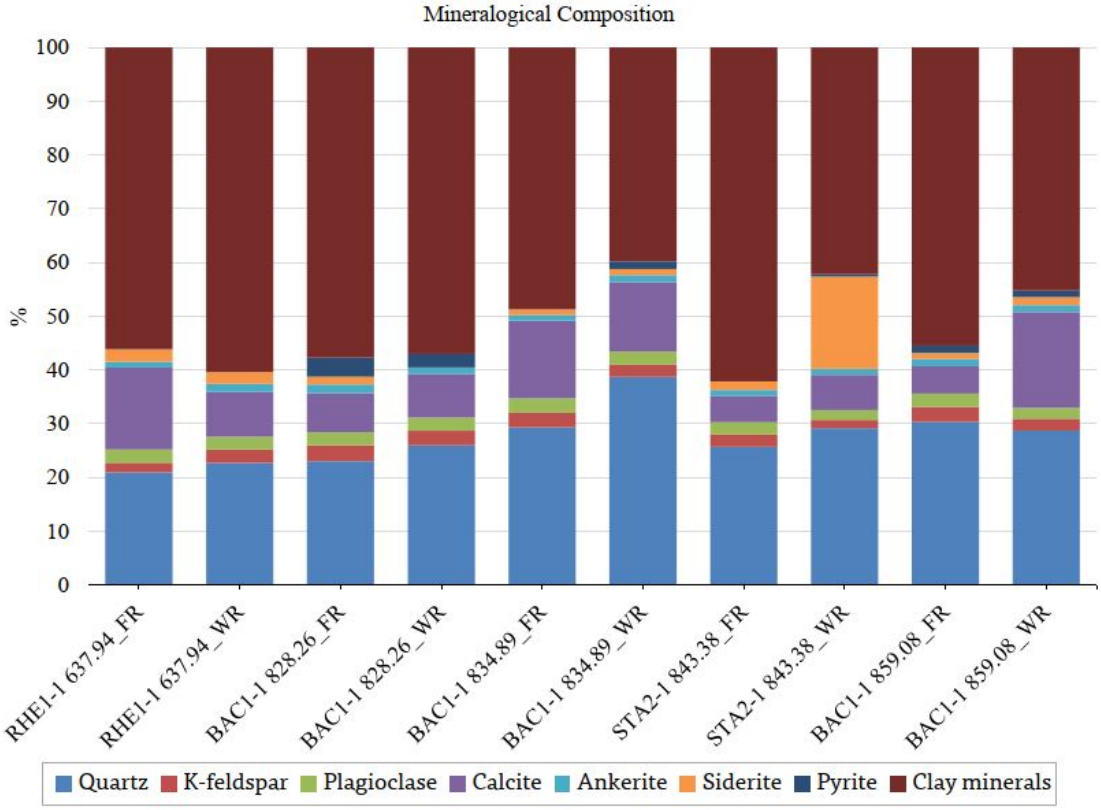

Figure 3.18: Results of quantitative determination of total amounts of quartz, k-feldspar, plagioclase, calcite, ankerite, siderite, pyrite and clay minerals of all samples. The average clay mineral concentration is approximately 53 %. Note that there is only one sample STA2-1 843.38 WR showing a high amount of siderite. There is no no systematic differences in composition between fault rock and wall rock samples.

3.4 Mineralogy of clay fractions

The results of the XRD analysis of the clay fraction show that all samples contain the same clay minerals: kaolinite, illite, chlorite, and illite/smectite mixed-layer. The basal reflection of illite is at d(00l) = 10 Å, producing 001-peaks at 10 Å, 5 Å, and 3.3 Å. Chlorite produces peaks at 14.2 Å, 7,1 Å, 4.73 Å, and 3.56 Å. Kaolinite peaks can be found at 7.1 Å, and 3.5 Å. Finally, a peak at approximately 11.9 Å in the Mg-saturated sample could be from the illite/smectite mixed-layer minerals, because it would represent a fraction of the sum of the smectite (14 Å) and illite (10 Å) spacing (green pattern in Figure 3.19 and Figure 3.20). No difference can be found when comparing the stacked XRD patterns from wall rock and fault rock (Figure 3.19 - Figure 3.21).

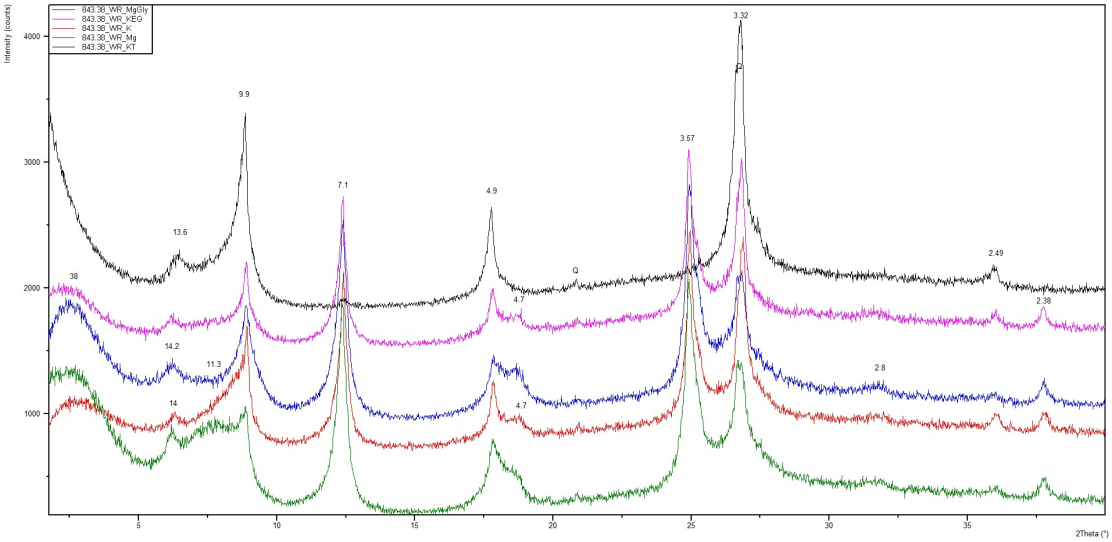

Figure 3.19: XRD patterns of sample STA2-1 843.38 WR: Mg-saturated (green), K-saturated (red), Mg-Gly-saturated (blue), K-EG-saturated (pink), and K-saturated and heated to 550 °C (black). d-values in Å; X-axis represents measured angle in 2θ, and y-axis intensity in counts per second.

When looking closer at XRD pattern from fault rock and wall rock, the peak intensities and positions are very similar. Only at lower 2θ angles between 0 ° and 9 ° peaks differ in width and intensity. With exception of sample BAC1-1 828.26 FR, all fault rock samples have higher intensities in the low angle regions than the wall rock samples at this low 2θ diffraction angle (Figure 3.22, Figure 3.23).

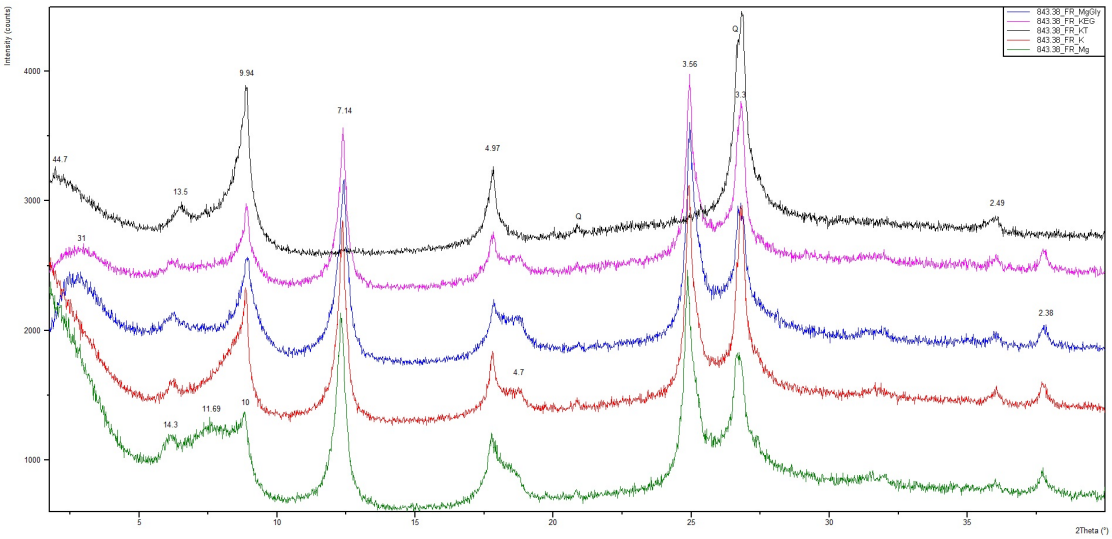

Figure 3.20: XRD patterns of sample STA2-1 843.38 FR: Mg-saturated (green), K-saturated (red), Mg-Gly-saturated (blue), K-EG-saturated (pink), and K-saturated and heated to 550 °C (black). d-values in Å; X-axis represents measured angle in 2θ, and y-axis intensity in counts per second.

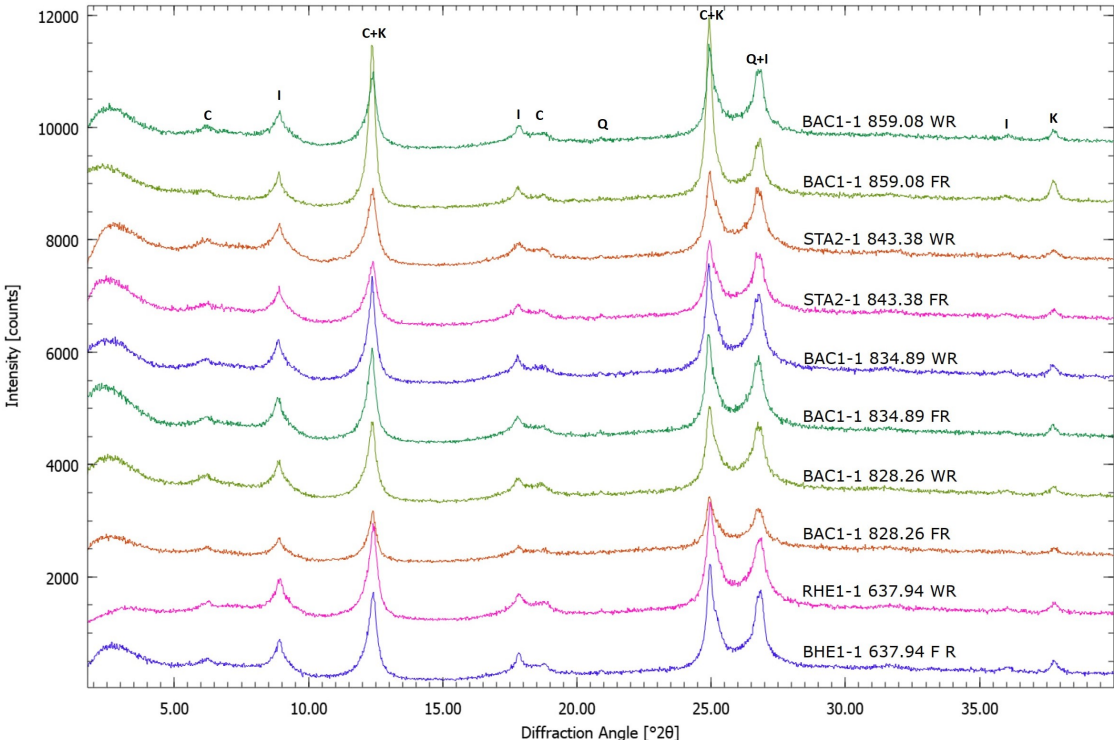

Figure 3.21: XRD patterns of all samples saturated with Mg and EG. Note that there is only marginal difference in peak intensity between the samples. C = chlorite; K=kaolinite; I=illite; Q=quartz;

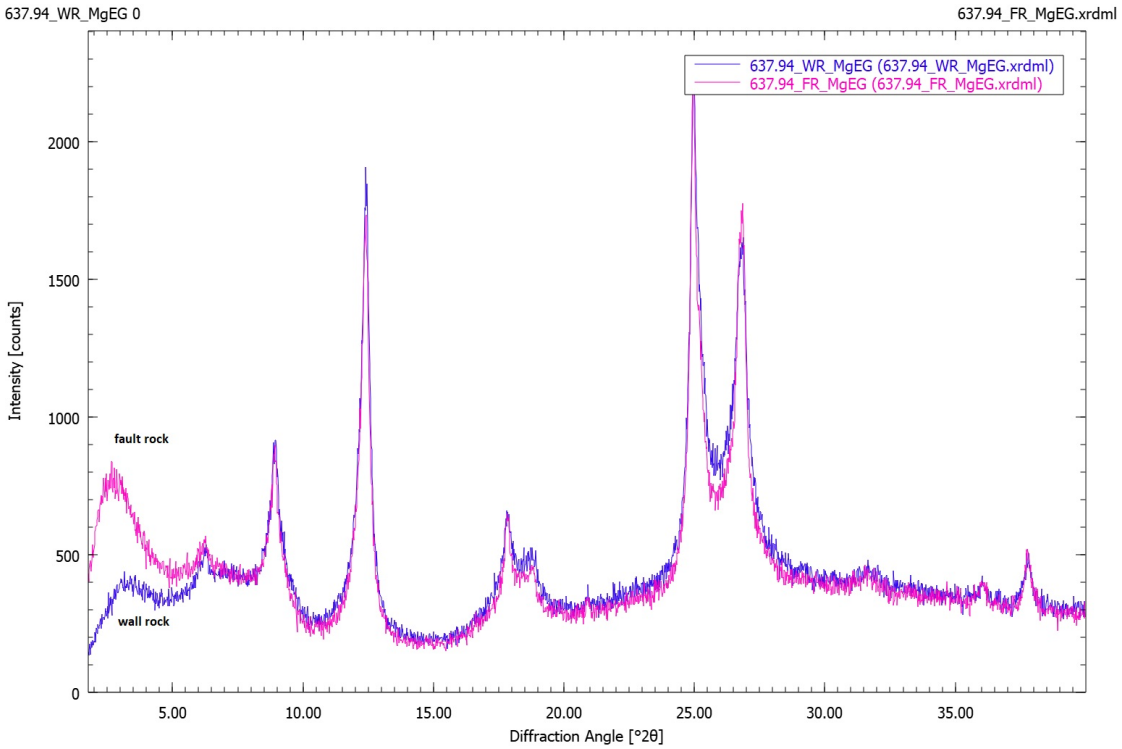

Figure 3.22: XRD patterns of Mg-EG-saturated fault rock (pink) and wall rock (blue) from sample RHE1-1 637.94. Note the difference in intensity at low diffraction angle.

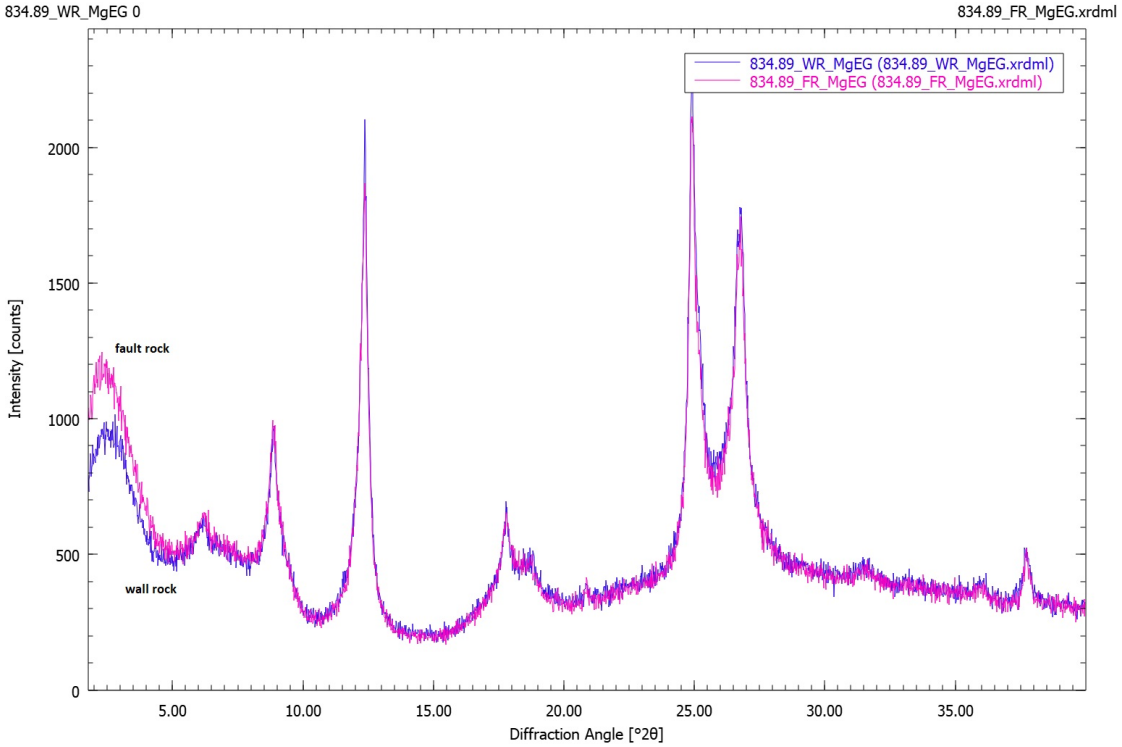

Figure 3.23: XRD patterns of fault rock (pink) and wall rock (blue) from sample BAC1-1 834.89 show differences in intensity at low diffraction angle

Mineralogy of $< 0.2\,\mu m$ Fraction

Usually, mixed-layer clay minerals can be better identified in the fine clay fraction ($< 0.2\,\mu m$ fraction). Hence, the fine clay fraction of two sample pairs (RHE1-1 637,94 and BAC1-1 834,89) was analysed. The measurement results from the $< 0.2\,\mu m$ fraction differ from the $< 2\,\mu m$ fraction only marginally. Clay minerals like illite and chlorite are still present in the sample, making identification and quantification of mixed-layer minerals rather difficult.
Nevertheless, the $< 0.2\,\mu m$ fraction shows slightly lower peak intensities compared to the $< 2\,\mu m$ fraction (Figure 3.24). In addition, XRD patterns have a high background, resulting in unclear peaks. However, broad peaks are visible between 6° 2θ and 10° 2θ indicating, illite/smectite mixed-layer clay minerals. It seems that most peaks are at around 12 Å in Mg saturated and 13 Å in Mg-EG saturated samples. This gives evidence for a regular interstratified R1 I/S mixed layer mineral. The 13 Å peak position in the Mg-EG saturated sample can be calculated from 17 Å EG-smectite plus 10 Å illite divided by two.

In sample BAC1-1 834.89 WR Mg-EG-saturated, there are 2 small peaks (at 17.19 ° 2θ and 9.6 ° 2θ) within the illite peak visible (Figure 3.25, Figure 3.26). From the angular difference of these two peaks, it can be deduced that ordered (R1) illite/smectite, containing approximately 74 % illite is present (Moore and Reynolds Jr, 1989). This angular difference is slightly higher in sample BAC1-1 834.89 FR Mg-EG-saturated, which indicates (R1) illite/smectite, containing 80 % illite.

In sample RHE1-1 637,94 the angular difference is also higher in the fault rock sample than in the wall rock sample, resulting in (R1) illite/smectite containing 73 % illite for the wall rock sample, and (R1) illite/smectite containing 77 % illite for the fault rock sample (Table 3.3).
Finally, the collapse of smectite to 10 Å in heated samples clearly indicated the existence of smectite.

Sample	$^{\circ}\Delta 2\theta$	% Illite
RHE1-1 637.94 WR	7.52	73
RHE1-1 637.94 FR	7.74	77
BAC1-1 834.89 WR	7.59	74
BAC1-1 834.89 FR	7.9	80

Table 3.3: Angular difference for estimation of percent illite/smectite in samples RHE1-1 637.94 and BAC1-1 834.89. Note that both fault rock samples have a higher percentage of illite compared to the wall rock sample. The samples from the deeper part of the drill core (834 m) contains more illite, than the sample from 627 m.

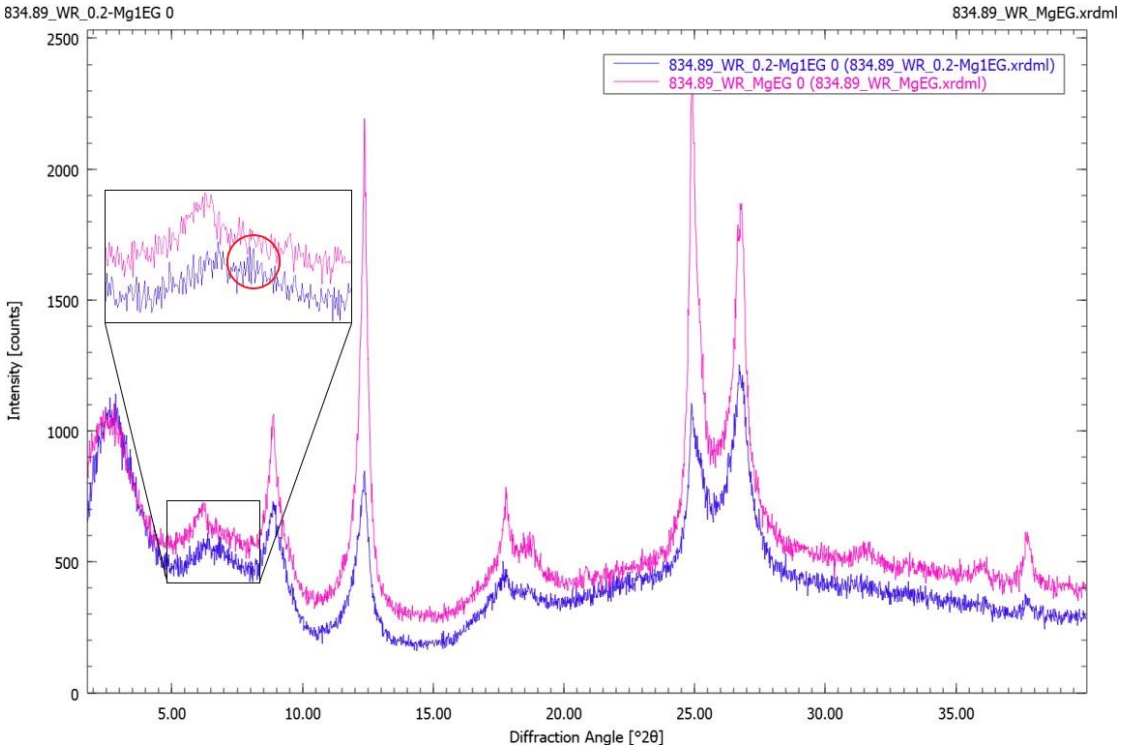

Figure 3.24: XRD patterns of sample BAC1-1 834.89 wall rock $< 0.2\mu m$ fraction (blue) compared to $< 2.0\mu m$ fraction (pink) both saturated with Mg and EG. Note that for the sample with smaller clay fraction (blue pattern), the peak intensity of illite and chlorite is lower, and thus a peak representative for illite/smectite mixed-layer minerals is visible. The illite/smecite mixed-layer peak is located within the red circle.

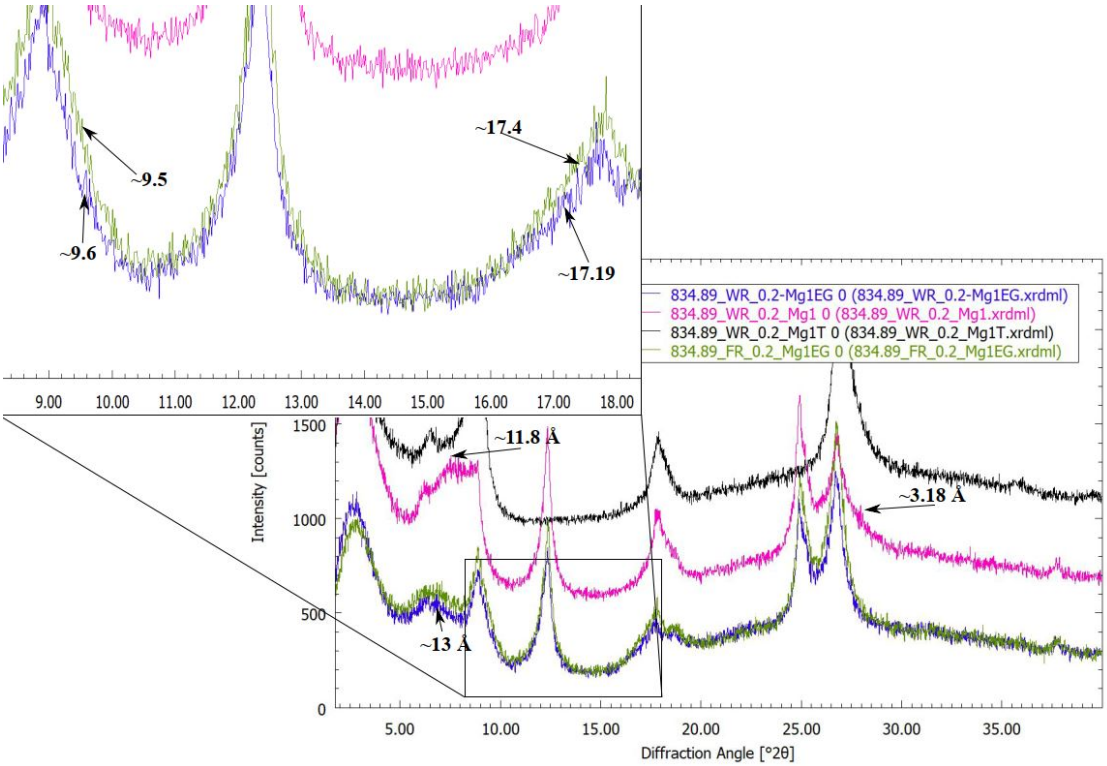

Figure 3.25: XRD patterns of sample BAC1-1 834,89 wall rock, Mg-saturated (pink), Mg and EG saturated (blue), heated to 550 °C (black), and BAC1-1 834,89 fault rock Mg and EG saturated (green). Note, labeled diffraction peaks at approximately 13 Å, 11.8 Å, and 3.18 Å are an indicator for illite/smectite mixed-layer clay minerals. The upper XRD-pattern (black) shows higher intensities due to the collapse of smectite. In the wall rock the angular difference between the peaks at 9.6 °2θ and 17.19 °2θ is 7.6 °2θ, and is an indicator for an ordered illite/smectite containing 74 % illite. Looking at the fault rock, the angular difference is with 7.9 °2θ higher than in the wall rock, resulting in an illite/smectite containing 80 % illite

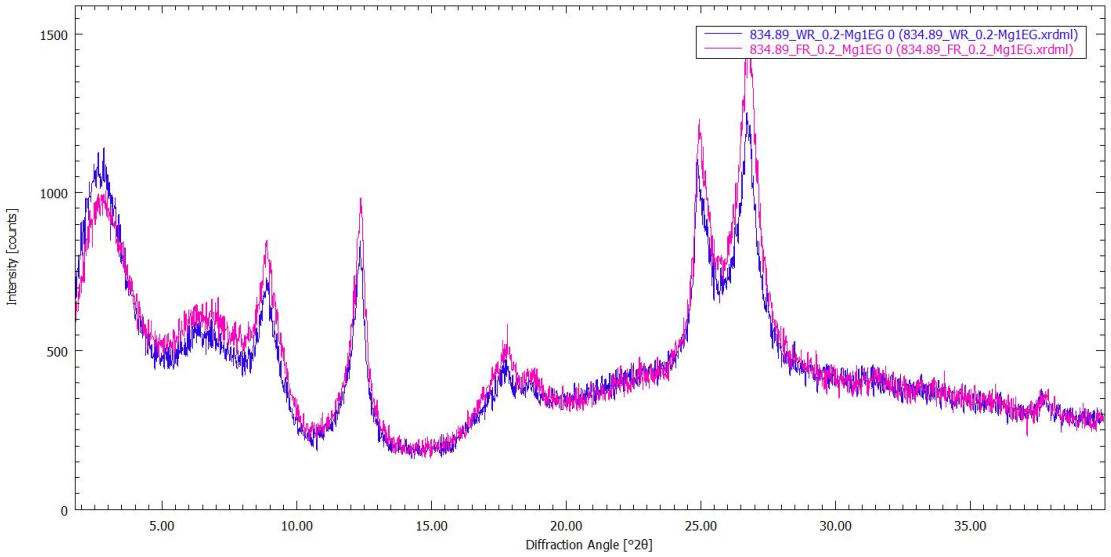

Figure 3.26: XRD patterns of sample BAC1-1 834.89 wall rock (pink) and fault rock (blue), both saturated with Mg and EG. Both samples are almost identical. Differences in mineralogy of mixed layer minerals are due to low resolution and high noise level imperceptible.

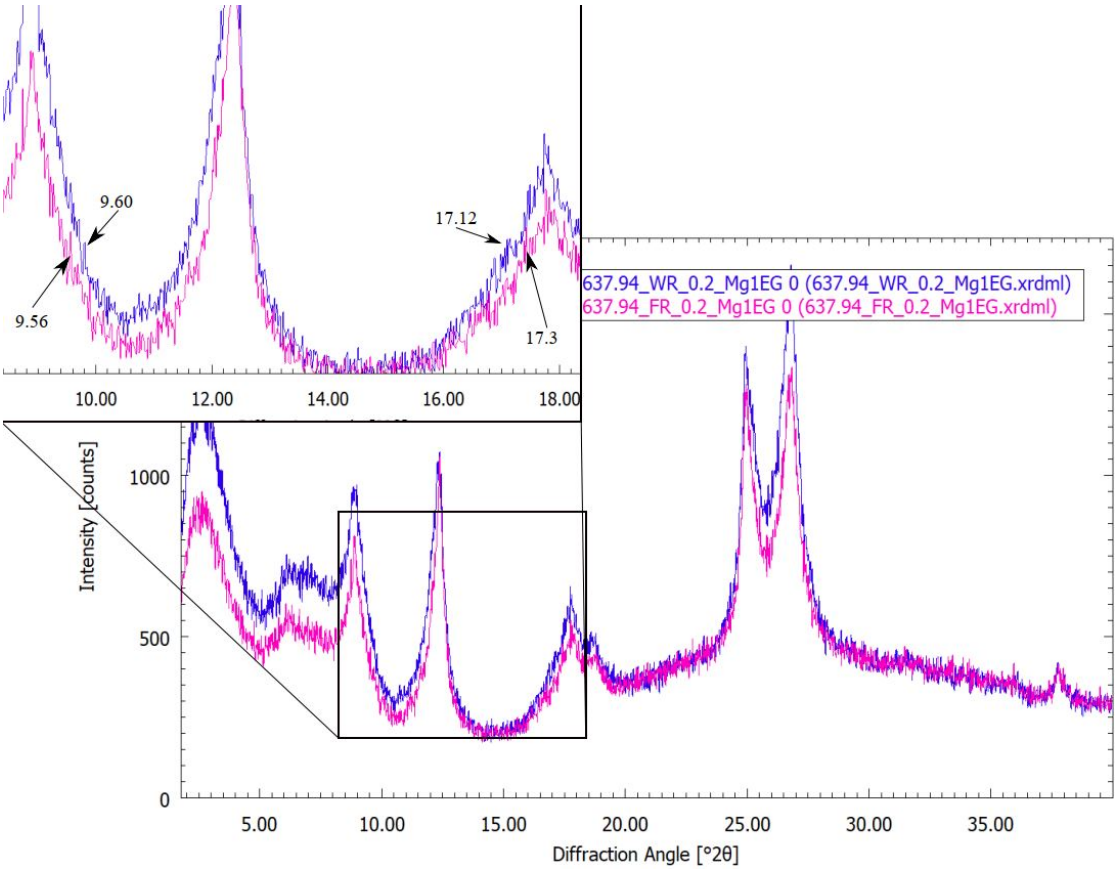

Figure 3.27: XRD patterns of sample RHE1-1 637.94 wall rock (pink) and fault rock (blue), both saturated with Mg and EG. There are peaks at around 9.6 and 17.12 °2θ. The angular difference between these peaks is 7.52 °2θ for the wall rock and 7.74 °2θ for the fault rock sample, resulting in an illite concentration of 73 % for the wall rock and 77 % illite for the fault rock.

3.5 Total carbon

The results of the total carbon analysis are summarised in table Table 3.4 below. All results are rounded to one decimal place since the reference material has a maximum accuracy of ± 0.05 %. All samples were measured twice in order to exclude errors in both the preparation and the measurement.

There is a minor difference in TOC content between fault rock and wall rock samples. It is noticeable that the TOC content is slightly higher in all fault rock samples. This is also visible in Figure 3.28, where the average of both measurements is shown. The organic carbon concentration ranges from 0.7 % to 1 % for all samples.

In comparison, values for the TIC content fluctuate significantly and range from 0.7 % to 2.1 %. A closer look reveals that samples BAC1-1 859.08 FR and STA2-1 843.38 FR have lower TIC contents (0.7 to 0.9 %) compared to the adjacent wall rock with 1.7 to 2.1 %. Furthermore, sample RHE1-1 637.94 FR has a notably lower TIC content (1.2-1.3 %) compared to the surrounding rock with 1.8 %. In two samples BAC1-1 834.89 and BAC1-1 828.26 no significant difference in TIC content can be measured. The results confirm the accuracy of the XRD analysis, and show that sample BAC1-1 859.08 FR has the lowest TIC concentration and calcite concentration, whereas sample BAC1-1 859.08 WR has the higest concetration of both calcite and TIC (Table 3.4 and Figure 3.18).

Additionally, only one sample (BAC1-1 828.26) shows the same values in TOC and TIC for fault rock and wall rock.

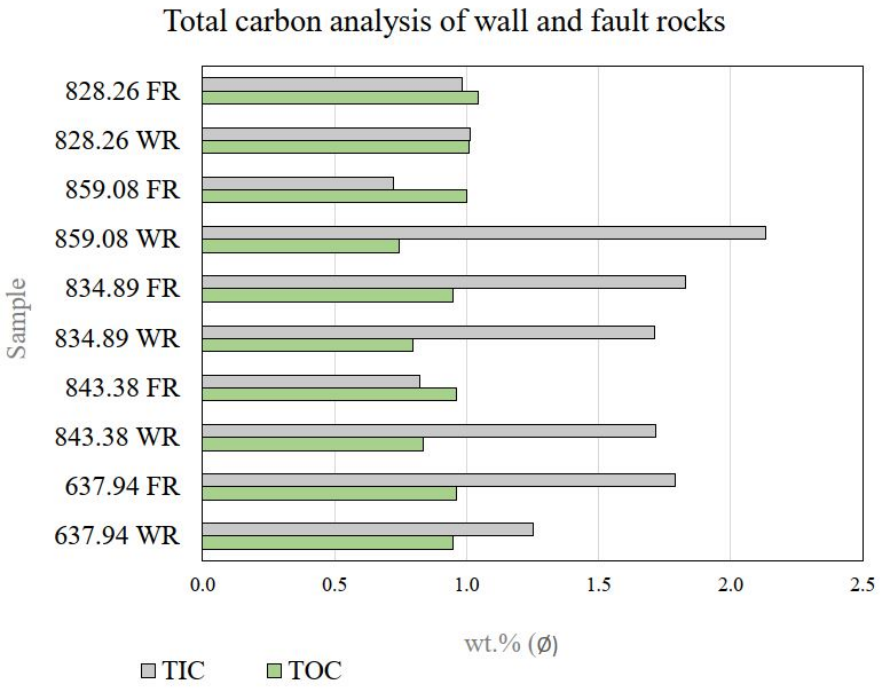

Figure 3.28: The bar chart shows the average TOC and TIC in wt.% from each sample. Note, that the TOC content is higher in fault rock samples, than in wall rock samples. There is no clear pattern in the TIC content recognizable. The concentration of TIC reflects the measured calcite content from the XRD analysis in Figure 3.18.

Well	Core depth / Rock type	TOC [wt%]	TIC [wt%]
RHE1-1	637.94 WR	0.9	1.3
RHE1-1	637.94 WR	1.0	1.2
RHE1-1	637.94 FR	1.0	1.8
RHE1-1	637.94 FR	1.0	1.8
STA2-1	843.38 WR	0.8	1.7
STA2-1	843.38 WR	0.8	1.7
STA2-1	843.38 FR	1.0	0.8
STA2-1	843.38 FR	1.0	0.8
BAC1-1	834.89 WR	0.8	1.7
BAC1-1	834.89 WR	0.8	1.7
BAC1-1	834.89 FR	0.9	1.8
BAC1-1	834.89 FR	1.0	1.8
BAC1-1	859.08 WR	0.7	2.1
BAC1-1	859.08 WR	0.8	2.1
BAC1-1	859.08 FR	1.0	0.7
BAC1-1	859.08 FR	1.0	0.7
BAC1-1	828.26 WR	1.0	1.0
BAC1-1	828.26 WR	1.0	1.0
BAC1-1	828.26 FR	1.0	1.0
BAC1-1	828.26 FR	1.0	1.0

Table 3.4: Total organic carbon and total inorganic carbon in percentage by weight of all samples. All fault rocks are shaded in red and all wall rocks are shaded in blue. Note that TOC content fluctuates very little between adjacent rocks, whereas TIC content varies more. Overall, fault rock samples have a slightly higher TOC content, than wall rock samples. The TIC values do not follow any clear pattern. Only one sample (BAC1-1 828.26) has no variation in carbon content.

3.6 Cation exchange capacity

The cation exchange capacity (CEC) was measured five times, and the mean value was calculated for each sample in order to avoid measurement errors. All final results can be seen in the bar chart (Figure 3.29). For better illustration, the results of fault rock and wall rock CEC are highlighted in different colors. The CEC of the standard sample "Hennersdorf" is 14 mEq/100g, and is therefore within the range of the standard. All measured values are between 17 and 35 mEq/100g and are therefore characteristic of clay samples. In two samples (BAC1-1 828.26 and STA2-1 843.38) the wall rock specimen shows significantly higher CEC values of 35 mEq/100g, compared to the adjacent fault rock, which shows CEC values of 17 and 26 mEq/100g. However, one sample pair BAC1-1 859.08 shows equal values of about 26 mEq/100g for both (wall and fault rock) specimens.

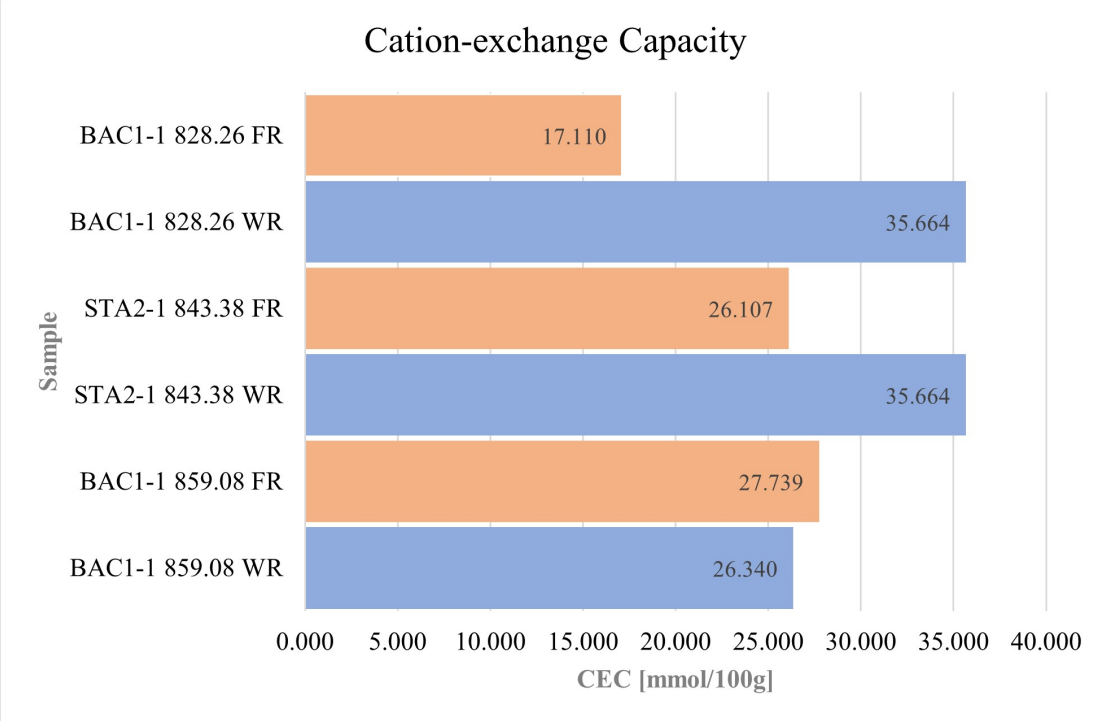

Figure 3.29: The bar chart shows the results of the CEC measurement for three pairs of samples. X-axis shows CEC in mmol/100g which is equal to mEq/100g. Note, the significant difference between fault rock and wall rock in sample pair BAC1-1 828.26 and STA2-1 843.38.

Chapter 4

Discussion

4.1 Slickensides and microstructures

During this thesis, kinematic indicators formed by ploughing clasts from three different fault rock samples of the OPA where statistically analyzed regarding slip distance. The most important finding is that slip distances of the fault planes can be identified on some slickenside surfaces under the microscope. Although this study could not identify the maximum displacement at the faults, it can be assumed, that displacements on individual slip surfaces are in the single-digit millimeter (mm) range (with most grooves ranging between 1000 μm and 2500 μm). Further, the statistical analysis has shown that the length of the displacement indicators on each sample does not vary much, and therefore the offset can be assumed to be representative. The different lengths of the grooves can be caused by the premature disintegration of the grains, which cause grooves or by several individual movements. The latter can be confirmed by the overlapping of grooves, and deviation of the directions of movement.

The observations of this study are in agreement with studies of the main fault in the Mt-Terri laboratory, where displacements in the millimetre range was identified (Laurich et al., 2014). Looking at the surface under the SEM confirms the short displacement and the disintegration of large clay minerals on the slickenside surface due to harder grains. Other kinematic indicators like steps could not be analysed under the SEM, because of the high relief. As already discussed in Laurich et al. (2014), the surface of slickensides does not differ much with higher magnification. That is to say, fault surfaces are covered homogeneously with clay minerals with a size of less than 250 nm, and are therefore not resolvable. This would also explain the high amount of small clay particles in the < 0.2 μm clay fraction.

Further, these small clay particles produced by friction sliding are typical for pol-

ished slickensides as already described by several authors (Laurich et al., 2014).

Finally, slickensides, which are covered with spherical nano-particles or dendrites do not show any sign of deformation. Consequently, these structures must necessarily been post-tectonic in origin. Due to the lack of chemical characterization, the exact formation of the nano-particles and dendrites can only be speculated. The most probable cause of the nano-particles is a deposition of material resulting from preparation, because specimens which are unprepared (not BIB milled) do not have these particles on the slickenside surface. The dendrites can also be found on unprepared specimens and could have originated naturally. The development of these dendrites out of the pore space could indicate a post-tectonic fluid transport. Dendrites usually form when supersaturated solutions penetrate the rock and precipitate on surfaces like cracks, which are exposed to air (Chopard et al., 1991). Indeed, this would contribute to the observed dendrites on the fault surface.

One of the most notable features from the BIB-milled specimens are the fractures which are parallel to the shear plane. These fractures are visible in all the examined specimens and are located close to the slickenside surface. It is regarded possible that these fractures are shear zones, which propagate between the clay minerals (Laurich et al., 2014). However, since no particle orientation can be seen on the shear surfaces, and fractures do not penetrate grains, it is more likely that these are stress relief fractures that occurred during drill core extraction.

Finally, calcite and celestite enrichment can be found in one fault rock sample. Previous studies on the main fault have shown that calcite and celestite mineral precipitation occurred syntectonically during the Jura folding (de Haller et al., 2014). This would also explain the calcite and celestite enrichment below the slickenside. Overall, no shear movement can be detected in the cross-section view of the observed samples, which can be explained due to the low offset of less than 5 mm. The absence of grains with cracks and deformed grains indicates a ductile deformation below the slickenside, which is common behavior of clay-rich fault rocks (Haines et al., 2013). However, in the analysed samples no deformation structures such as shear bands or dissolution-precipitation structures were identified.

4.2 Mineralogy and composition

As previously mentioned, the bulk mineralogy (kaolinite, chlorite, quartz, calcite, ankerite, siderite, albite, microcline, pyrite, and muscovite) does not show any systematic difference between fault rock and wall rock samples. The results are in agreement with previous studies, however, an absence of calcite in fault rocks, as mentioned by Orellana et al. (2022) could not be confirmed. One sample RHE1-1 637.94 FR has more calcite than the undeformed wall rock, which is due to the celestite and calcite precipitation previously described. In this sample, the celestite is also clearly visible under the SEM. Therefore, it can be deduced that not all fault rock samples contain calcite and celestite precipitations.

As already mentioned in the results, the XRD of the $< 2\ \mu m$ clay fraction, does not show any changes in mineralogy between fault rock and wall rock. All analysed samples contain the same clay minerals: kaolinite, illite, chlorite, and illite/smectite mixed-layer. By extracting the finer clay fraction, it is possible to detect differences in the composition of mixed layer minerals. However, this proved to be difficult with these samples. The main reason for the poor resolution is the fine grain size of the OPA which makes it difficult to remove unwanted coarser clay minerals for analysis. However, in four samples it was possible to quantify the illite/smectite, indicating R1 I/S mixed layer minerals with an illite content between 73 % and 80 %. Both faul rock sample RHE1-1 637.94 and BAC1-1 834.89 show a small increase of illite (77 % and 88 %) in the mixed layer minerals compared to the undeformed wall rock (73 % and 74 %). This result would confirm the illite aggregates in shear zones Laurich et al. (2014) and thus an illitization in fault rocks of the OPA. Finally, an increase of the illitization with depth could occure, because in the analyzed samples the illite content is higher in samples from 834.89 m than in samples from 637.94 m.

The organic carbon concentration of less than 1 wt. % is similar to the measured values at the main fault (Laurich et al., 2017). Further, slightly higher TOC concentrations in fault rocks can not explain the darker colour of the fault rocks (Laurich et al., 2017), but could be caused due to organic fluid diffusion. However, this statement must be supported by a larger number of samples. Finally, measured inorganic carbon concentration is congruent with the semi-quantitative analysis from X-ray powder patterns.

The results of the cation exchange capacity measurement show a significantly increased exchange capacity in the two wall rocks (BAC1-1 828.26 and STA2-1 843.38 FR) compared to the fault rocks. As a result of this, only a variation in the illite/smectite content of the mixed-layer could cause the variation in CEC.

Chapter 5

Implications and Conclusions

Within the scope of this work, five sample pairs (consisting of fault rock and wall rock samples) of the Opalinus Clay, were analyzed in detail in terms of their clay mineralogical and structural geological properties. The aim of this work was to identify if the properties (self-sealing/self-healing) of the Opalinus Clay are different in fault rocks, compared to the undeformed wall rock. Using Powder XRD, high-resolution digital microscope, and SEM, the samples were analyzed in detail. Further, the cation exchange capacity and the total carbon concentration was determined. The following implications and conclusions derive from this research:

- Slightly higher TOC concentration in fault rock samples, and dendrite on slickenside surface, could indicate fluid migration along faults.
- The wall rock specimen shows CEC values of 35 mEq/100g, compared to the adjacent fault rock, which shows CEC values of 17 and 26 mEq/100g.
- Slip distances of less than 5 mm are measured from imprints of ploughing clasts on three typical slip surfaces. Additionally, the direction of movement is ascertainable.
- Clay particles in nanometer size are formed on the slickenside surface by brittle deformation. However, there are no signs of brittle deformation directly below the slickenside surface.
- The slickenside of one sample is covered with spherical nano-particles, which are post-tectonic in origin.
- There is a transition from smectite to illite, which is however very small and only limited to the adjacent area of the shear plane. This smectite to illite transition shows that (R1) I/S mixed layer minerals in fault rocks contain slightly more illite (77-80 %) compared to I/S mixed layer minerals in wall rocks (73-74 %).

- The study of cation exchange capacity shows promising results in the determination of illite in mixed layer minerals of wall rock and fault rock samples, and therefore it would be recommended to carry out further studies using this method with a larger sample size. Further, XRD analysis using the $< 0.1\ \mu m$ fraction could provide better I/S composite peak resolution for the identification of mixed-layer minerals and would help to support the outcome of the study. Finally, transmission electron microscopy technique could help to make the illite transition zone visible.

Acknowledgements

Foremost, I would like to express my sincere thank to my Supervisor Ao. Univ. Prof. Susanne Gier and Co-Supervisor Dr. Kurt Decker for your guidance and excellent support during my research. Thank you both for your time and great organisation. Thanks to Nagra, in particular Raphael Schneeberger, PhD and Herfired Madritsch, PhD, for providing sample material from the Opalins Clay drill cores. Further, I want to thank Beatrix Bethke, DI for the assistance with the TOC/TIC measurement. Special thanks also to David Misch, PhD from the University of Leoben for the fast processing of my samples and excellent communication. Furthermore I have to thank Dr. Anna Rogowitz for helping me with the Sample preparation and SEM analysis. I also want to thank my girlfriend and cat for their continuous emotional support. Last but not least, I would like to thank my family for the permanent finical support during my years in University.
Thank you each and every one of you, without you this thesis would not have been possible.

Bibliography

Bläsi, H., Deplazes, G., Schellmann, M. and Traber, D. (2013), 'Sedimentologie und stratigraphie des 'braunen doggers' und seiner westlichen äquivalente', *Nagra Arbeitsbericht, NAB* pp. 12–51.

Bläsi, H., Peters, T. and Mazurek, M. (1991), 'Der opalinuston des mont terri (kanton jura). lithologie, mineralogie und physiko-chemische gesteinsparameter', *Unpublished NAGRA internal report* .

Borchardt, G. (1989), *Smectites*, John Wiley and Sons, Ltd, chapter 14, pp. 675–727.

Büchi, U. P., Lemcke, K., Wiener, G. and Zimdars, J. (1965), 'Geologische ergebnisse der erdölexploration auf das mesozoikum im untergrund des schweizerischen molassebeckens', *Bulletin der Schweizerischen Vereinigung von Petroleum-Geologen und-Ingenieuren* **15**, 7–38.

Burkhalter, R., Bläsi, H. and Feist-Burkhardt, S. (1997), 'Der dogger ß (oberes aalénien) in den bohrungen herdern-1, berlingen-1 und kreuzlingen-1 (nordschweiz) und seine beziehungen zu den gleichaltrigen schichten im nordjura', *Eclogae Geologicae Helvetiae* **90**, 269–291.

Chopard, B., Herrmann, H. J. and Vicsek, T. (1991), 'Structure and growth mechanism of mineral dendrites', *Nature* **353**(6343), 409–412.

Crisci, E., Ferrari, A., Giger, S. and Laloui, L. (2018), 'On the swelling behavior of shallow opalinus clay shale'.

de Haller, A., Mazurek, M., Spangenberg, J. and Möri, A. (2014), Selfsealing of faults (sf) project: Final report, Technical report, Mont Terri Technical Report, TR 08-02. Wabern, Switzerland: Federal Office ....

Decker, K., Schneeberger, R. and Madritsch, H. (2022), 'Paleo-strain reconstruction from drill core mapping and their relevance for northern switzerland', Presented at the 20th Swiss Geoscience Meeting, November 18-20, 2022, Lausanne. Structural Geology, Tectonics and Geodynamics P 1.19.

Dixon, J. B. and Weed, S. B., eds (1989), *Minerals in Soil Environments*, Soil Science Society of America.

Douglas, L. A. (1989), *Vermiculites*, John Wiley and Sons, Ltd, chapter 1, pp. 635–674.

Ewald, P. (1962), Laue's discovery of x-ray diffraction by crystals, *in* 'Fifty Years of X-Ray Diffraction: Dedicated to the International Union of Crystallography on the Occasion of the Commemoration Meeting in Munich July 1962', Springer, pp. 31–56.

Gaucher, E., Fernández, A. and Waber, H. (2003), 'Rock and mineral characterisation of the opalinus clay formation', *Mont Terri Project–Geochemistry of Water in the Opalinus Clay Formation at the Mont Terri Rock Laboratory. Reports of the Federal Office for Water and Geology (FOWG), Geology Series* **5**, 281–303.

Gee, G. W. and Or, D. (2002), '2.4 particle-size analysis', *Methods of soil analysis. Part* **4**(598), 255–293.

Gehring, A. U., Keller, P. and Heller, F. (1991), 'Paleomagnetism and tectonics of the jura arcuate mountain belt in france and switzerland', *Tectonophysics* **186**(3), 269–278.

Grim, R. E. (1962), *Applied clay mineralogy*, McGraw-Hill Book Company.

Grim, R. E. (1968), *Clay Mineralogy (McGraw-Hill International Series in the Earth and Planetary)*, McGraw-Hill Companies.

Haines, S. H., Kaproth, B., Marone, C., Saffer, D. and van der Pluijm, B. (2013), 'Shear zones in clay-rich fault gouge: A laboratory study of fabric development and evolution', *Journal of Structural Geology* **51**, 206–225.

Hostettler, B., Reisdorf, A. G., Jaeggi, D., Deplazes, G., Bläsi, H., Morard, A., Feist-Burkhardt, S., Waltschew, A., Dietze, V. and Menkveld-Gfeller, U. (2017), 'Litho- and biostratigraphy of the opalinus clay and bounding formations in the mont terri rock laboratory (switzerland)', *Swiss Journal of Geosciences* **110**(1), 23–37.

Hower, J., Eslinger, E. V., Hower, M. E. and Perry, E. A. (1976), 'Mechanism of burial metamorphism of argillaceous sediment: 1. mineralogical and chemical evidence', *Geological Society of America Bulletin* **87**(5), 725.

IAEA (2003), *Scientific and Technical Basis for the Geological Disposal of Radioactive Wastes*, number 413 *in* 'Technical Reports Series', IAEA, Vienna.

Kastrup, U., Zoback, M. L., Deichmann, N., Evans, K. F., Giardini, D. and Michael, A. J. (2004), 'Stress field variations in the swiss alps and the northern alpine foreland derived from inversion of fault plane solutions', *Journal of Geophysical Research: Solid Earth* **109**(B1).

Keller, L. M., Schuetz, P., Erni, R., Rossell, M. D., Lucas, F., Gasser, P. and Holzer, L. (2013), 'Characterization of multi-scale microstructural features in opalinus clay', *Microporous and Mesoporous Materials* **170**, 83–94.

Köster, E. (1964), *Granulometrische und morphometrische Messmethoden an Mineralkörnern, Steinen und sonstigen Stoffen*, F. Enke.

Lauper, B., Jaeggi, D., Deplazes, G. and Foubert, A. (2018), 'Multi-proxy facies analysis of the opalinus clay and depositional implications (mont terri rock laboratory, switzerland)', *Swiss Journal of Geosciences* **111**(3), 383–398.

Laurich, B., Urai, J. L., Desbois, G., Vollmer, C. and Nussbaum, C. (2014), 'Microstructural evolution of an incipient fault zone in opalinus clay: Insights from an optical and electron microscopic study of ion-beam polished samples from the main fault in the mt-terri underground research laboratory', *Journal of Structural Geology* **67**, 107–128.

Laurich, B., Urai, J. L., Vollmer, C. and Nussbaum, C. (2017), 'Deformation mechanisms and evolution of the microstructure of gouge in the main fault in opalinus clay in the mont terri rock laboratory (CH)'.

Leco-Corporation (2018), 'Temperature-dependent determination of total organic carbon (toc) in soil, rock, and shale'.

Lee, S. and Tank, R. (1985), 'Role of clays in the disposal of nuclear waste: A review', *Applied Clay Science* **1**(1), 145–162. Clay Mineralogy in Agriculture, Industry and the Environment.

Mazurek, M., Hurford, A. J. and Leu, W. (2006), 'Unravelling the multi-stage burial history of the swiss molasse basin: integration of apatite fission track, vitrinite reflectance and biomarker isomerisation analysis', *Basin Research* **18**(1), 27–50.

Meier, L. P. and Kahr, G. (1999), 'Determination of the cation exchange capacity (CEC) of clay minerals using the complexes of copper(II) ion with triethylenetetramine and tetraethylenepentamine', *Clays and Clay Minerals* **47**(3), 386–388.

Moore, D. M. and Reynolds Jr, R. C. (1989), *X-ray Diffraction and the Identification and Analysis of Clay Minerals.*, Oxford University Press (OUP).

Murray, H. H. (2006*a*), Chapter 2 structure and composition of the clay minerals, *in* H. H. Murray, ed., 'Applied Clay Mineralogy', Vol. 2 of *Developments in Clay Science*, Elsevier, pp. 24–27.

Murray, H. H. (2006*b*), Chapter 6 bentonite applications, *in* H. H. Murray, ed., 'Applied Clay Mineralogy', Vol. 2 of *Developments in Clay Science*, Elsevier, pp. 111–130.

Nadeau, P. H. (1981), 'Burial and contact metamorphism in the mancos shale', *Clays and Clay Minerals* **29**(4), 249–259.

NAGRA (2002*a*), Project opalinus clay safety report:demonstration of disposal feasibility for spent fuel, vitrified high-level waste and long-lived intermediate-level waste (entsorgungsnachweis), Technical report, Technical Report 02-05, Wettingen, Switzerland.

NAGRA (2002*b*), Synthese der geowissenschaftlichen untersuchungsergebnisse (entsorgungsnachweis), Technical report, Technical Report 02-03, Wettingen, Switzerland.

NAGRA (2021), Tbo bülach-1-1: Data report, Technical report, Arbeitsbericht NAB 02-08, Wettingen, Switzerland.

Nussbaum, C., Bossart, P., Amann, F. and Aubourg, C. (2011), 'Analysis of tectonic structures and excavation induced fractures in the opalinus clay, mont terri underground rock laboratory (switzerland)', *Swiss Journal of Geosciences* **104**(2).

Nussbaum, C., Kloppenburg, A., Caër, T. and Bossart, P. (2017), 'Tectonic evolution around the mont terri rock laboratory, northwestern swiss jura: constraints from kinematic forward modelling', *Swiss Journal of Geosciences* **110**(1), 39–66.

Ohazuruike, L. and Lee, K. J. (2023), 'A comprehensive review on clay swelling and illitization of smectite in natural subsurface formations and engineered barrier systems', *Nuclear Engineering and Technology* .

Orellana, L. F., Nussbaum, C., Grafulha, L., Henry, P. and Violay, M. (2022), 'Physical characterization of fault rocks within the opalinus clay formation', *Scientific reports* **12**(1), 1–13.

Pytte, A. M. and Reynolds, R. C. (1989), The thermal transformation of smectite to illite, *in* 'Thermal History of Sedimentary Basins', Springer New York, pp. 133–140.

Schoonheydt, R. and Johnston, C. (2006), Chapter 3 surface and interface chemistry of clay minerals, *in* F. Bergaya, B. K. Theng and G. Lagaly, eds, 'Handbook of Clay Science', Vol. 1 of *Developments in Clay Science*, Elsevier, pp. 87–113.

Schultz, L. (1964), 'Quantitative interpretation of mineralogical composition from x-ray and chemical data for the pierre shale'.

Tanner, C. B. and Jackson, M. L. (1948), 'Nomographs of sedimentation times for soil particles under gravity or centrifugal acceleration', *Soil Science Society of America Journal* **12**(C), 60–65.

Whitney, G. (1990), 'Role of water in the smectite-to-illite reaction', *Clays and Clay Minerals* **38**(4), 343–350.

Zhang, C.-L., Rothfuchs, T., Jockwer, N., Wieczorek, K., Dittrich, J., Mueller, J., Hartwig, L. and Komischke, M. (2007), 'Thermal effects on the opalinus clay. a joint heating experiment of andra and grs at the mont terri url (he-d project). final report'.

Zheng, L., Rutqvist, J., Birkholzer, J. T. and Liu, H.-H. (2015), 'On the impact of temperatures up to 200°c in clay repositories with bentonite engineer barrier systems: A study with coupled thermal, hydrological, chemical, and mechanical modeling', *Engineering Geology* **197**, 278–295.

List of Figures

Appendix A

Appendix

A.1 Geology and Introduction

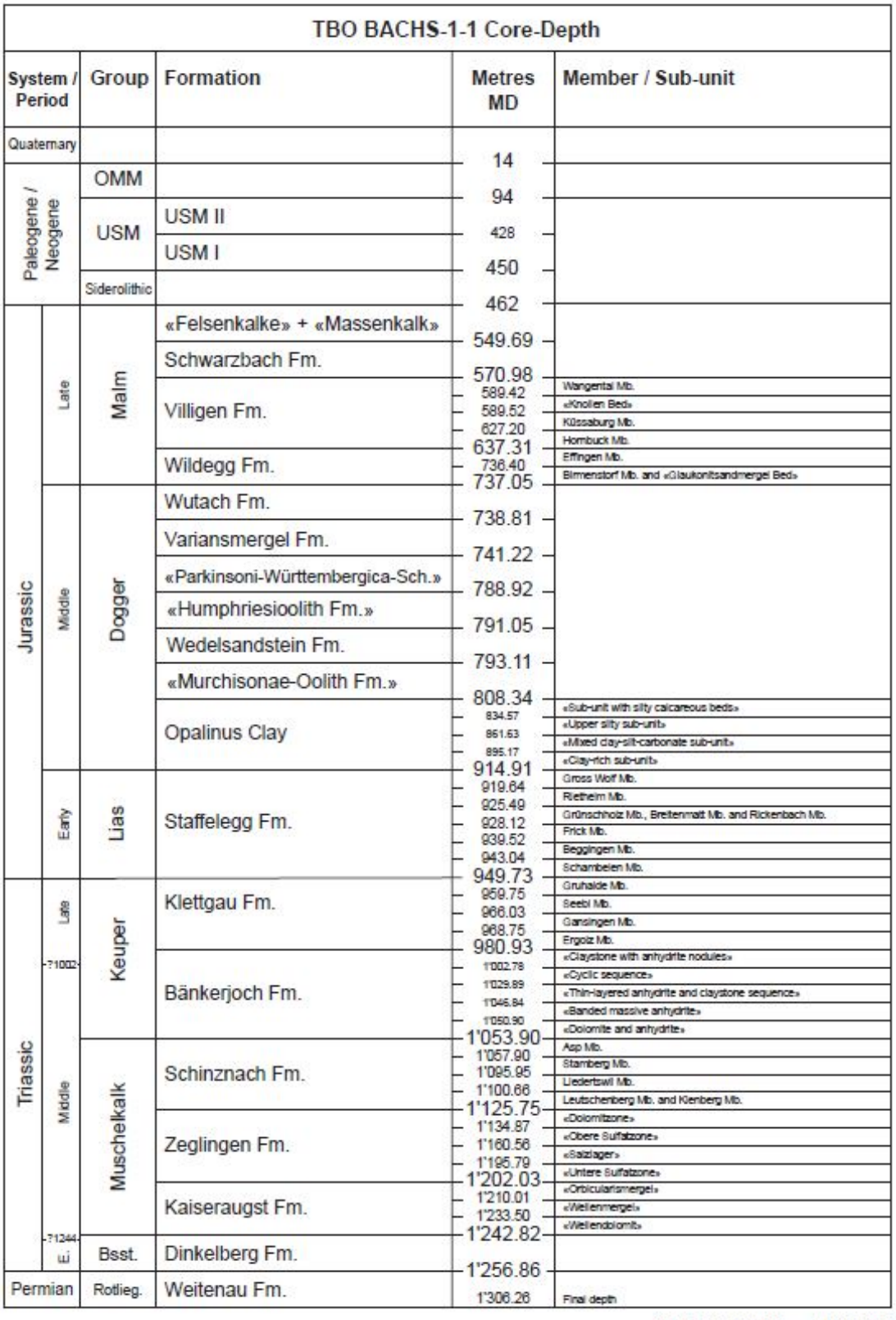

Figure A.1: BAC1-1 borehole stratigraphy. (NAGRA, 2021)

A.2 Geology and Introduction

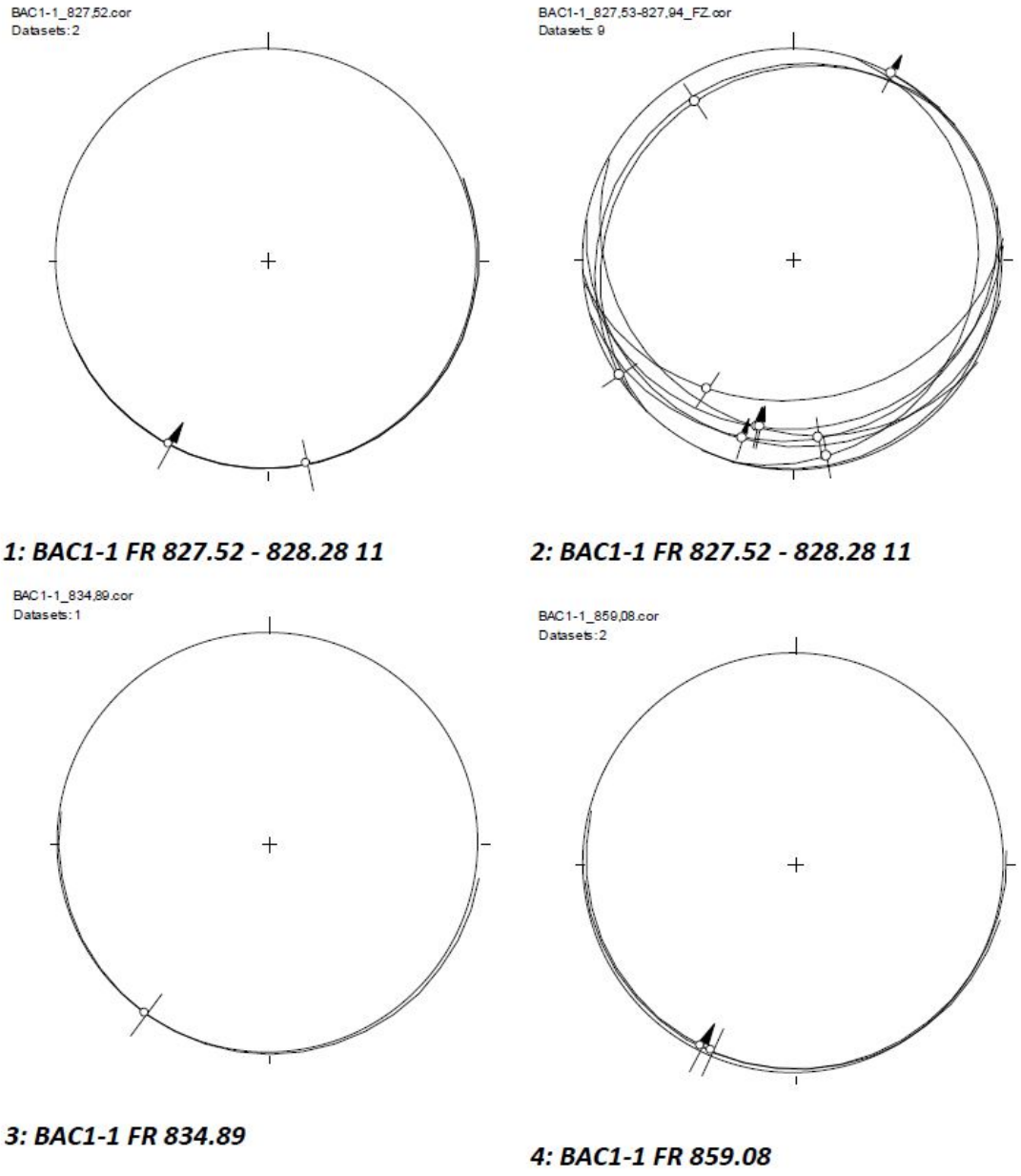

Figure A.2: Schmidt's net plots from the analyzed fault zones from borehole BAC1-1 show that all of the sampled faults and fault zones are shallow-dipping or sub-horizontal with SSW-NNE- or SSE-NNW-trending slickenlines. Available shear sense indicators such as fibrous mineralisation and ploughing clasts prove top-NNE- or top-NNW-directed slip.
Adapted from Decker et al. (2022).

A.3 Geology and Introduction

Figure A.3: Schmidt's net plots from the analyzed fault zones from boreholes RHE1-1 and STA2-1 show that all of the sampled faults and fault zones are shallow-dipping or sub-horizontal with SSW-NNE- or SSE-NNW-trending slickenlines. Available shear sense indicators such as fibrous mineralisation and ploughing clasts prove top-NNE- or top-NNW-directed slip.
Adapted from Decker et al. (2022).

A.4 Methods

Figure A.4: left: Atterberg-cylinder with clay particles in suspension (stable clay suspension). right: Atterberg-cylinder with flocculated/aggregated clay particles on the bottom (unstable clay suspension).

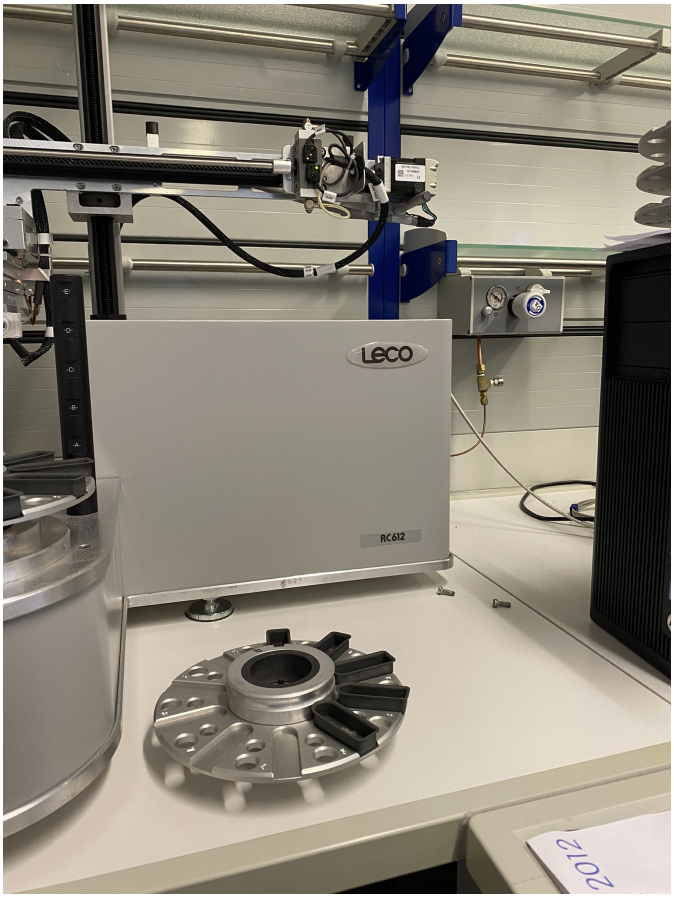

Figure A.5: RC612 Multiphase Determinator with filled crucible for TOC/TIC analysis.

A.5 Surface images

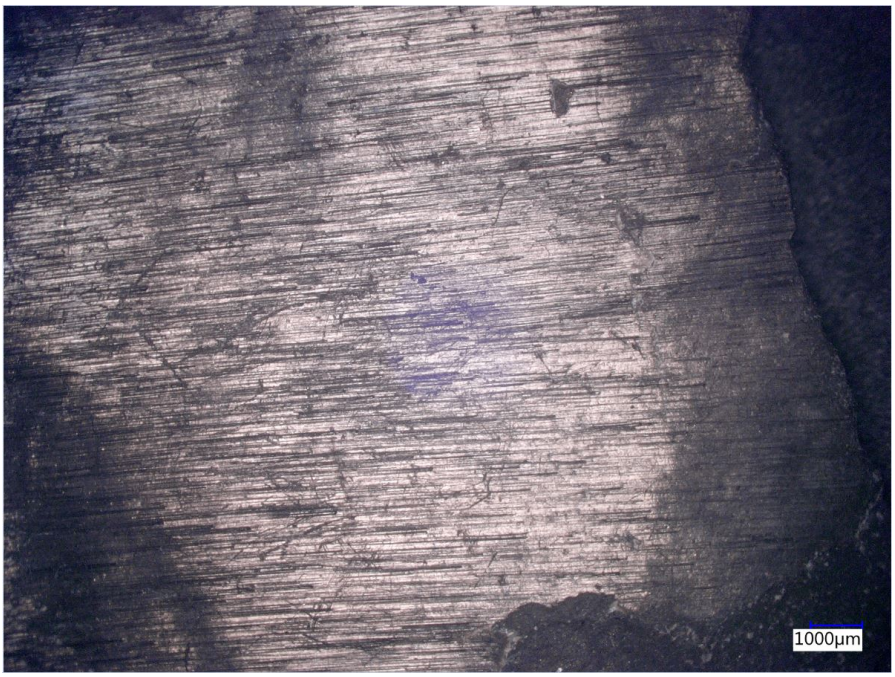

Figure A.6: Digital image of mapped sample (STA2-1 843.38) shows long grooves in x-direction. Note that the missing block moved towards the east.

Figure A.7: Digital image of mapped sample (STA2-1 843.38) shows short grooves in x-direction. Note that the missing Block moved towards the north-east.

A.6 KS-Test

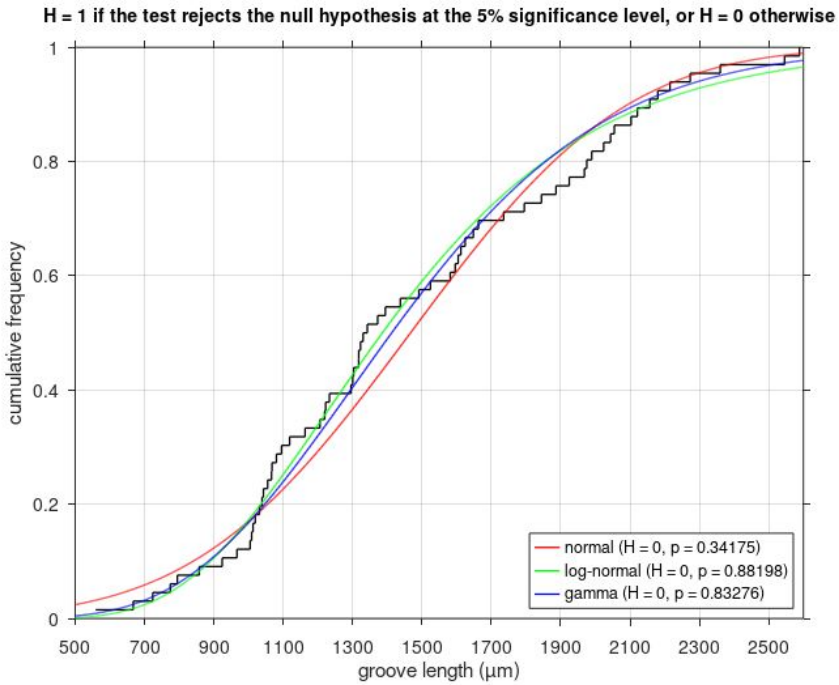

Figure A.8: Kolmogorov–Smirnov test from sample STA2-1 843.38 FR with long grooves shows that gamma distribution and log-normal distribution fits better to data.

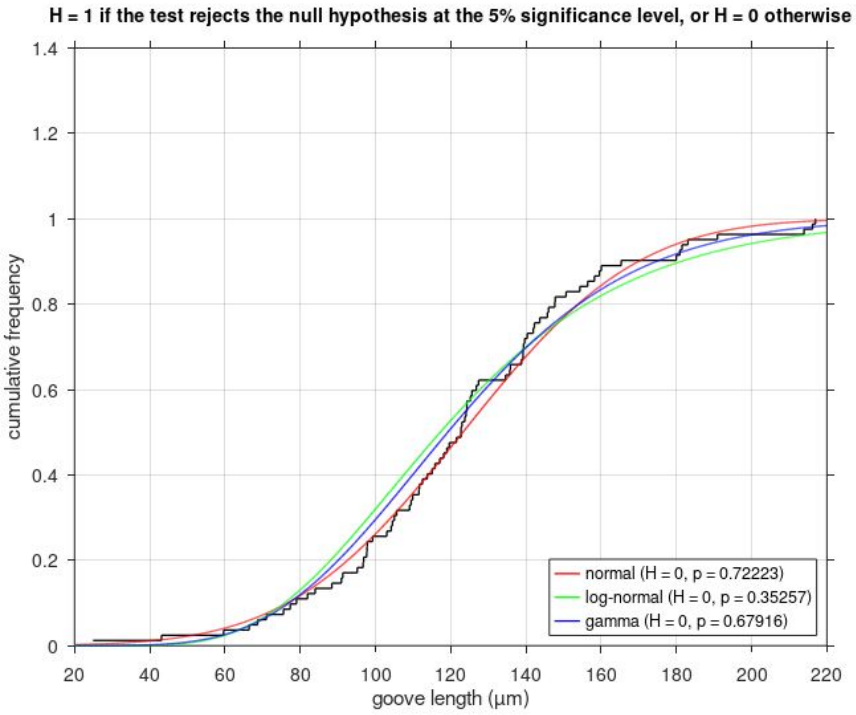

Figure A.9: Kolmogorov–Smirnov test from sample STA2-1 843.38 FR with short grooves indicates that data are normally distributed.

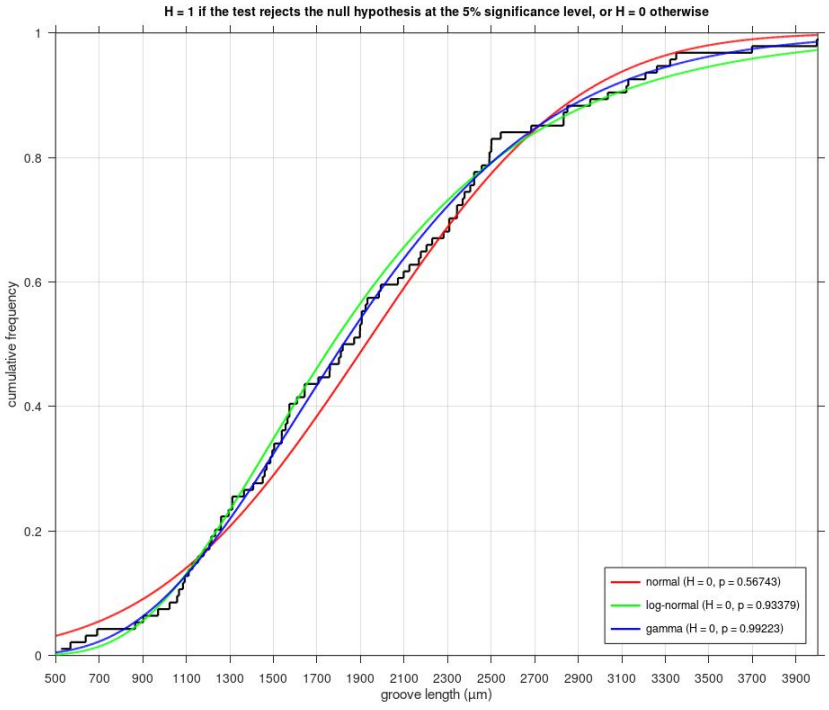

Figure A.10: Kolmogorov–Smirnov test from sample BAC1-1 827.52 FR indicates that data are gamma distributed.

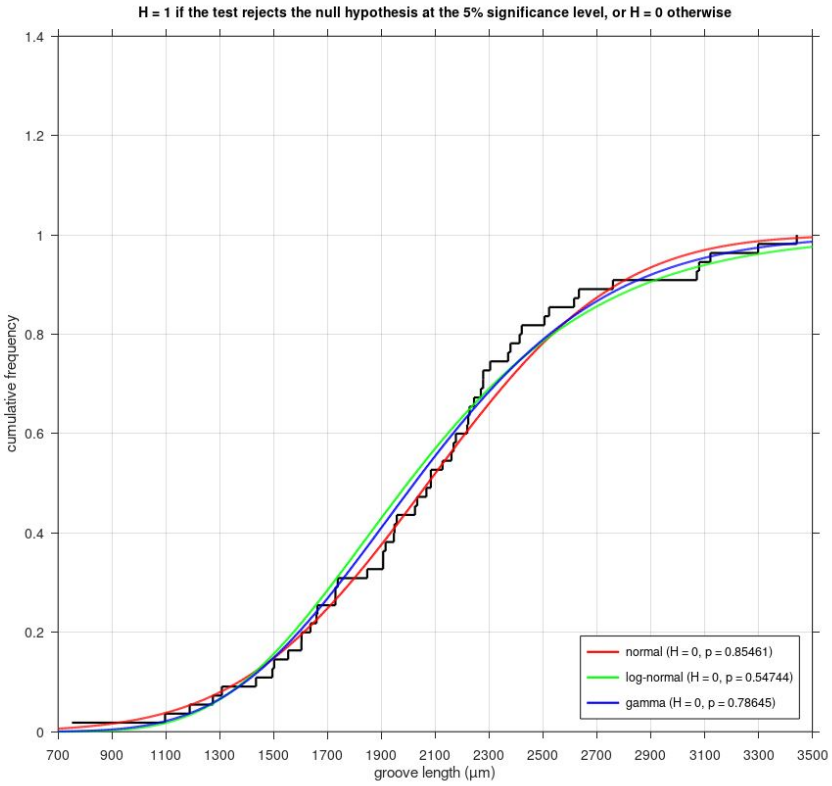

Figure A.11: Kolmogorov–Smirnov test from sample STA2-1 843.38 FR indicates that data are normally distributed.

A.7 Histograms groove length

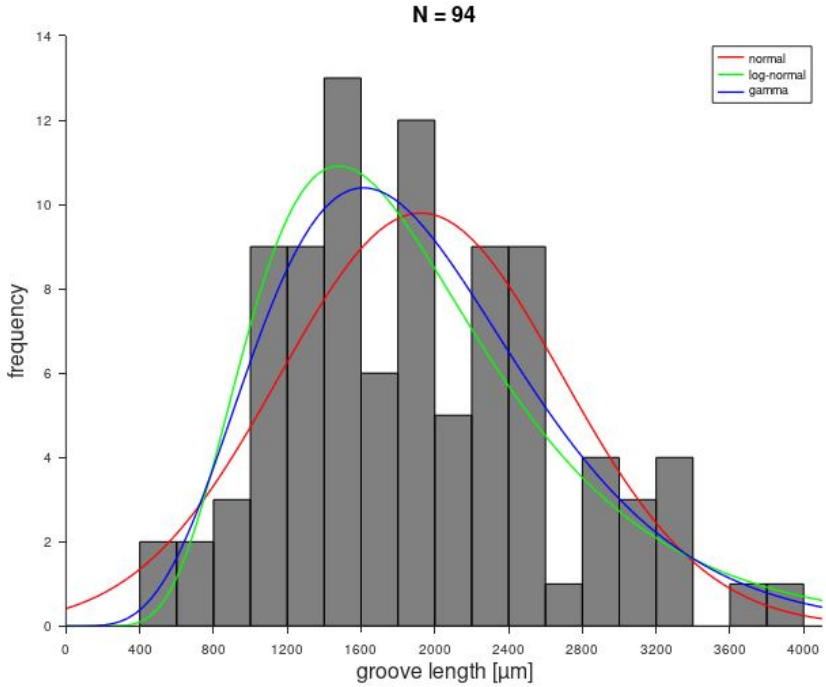

Figure A.12: Histogram of sample BAC1-1 827.52 FR with probability distribution.

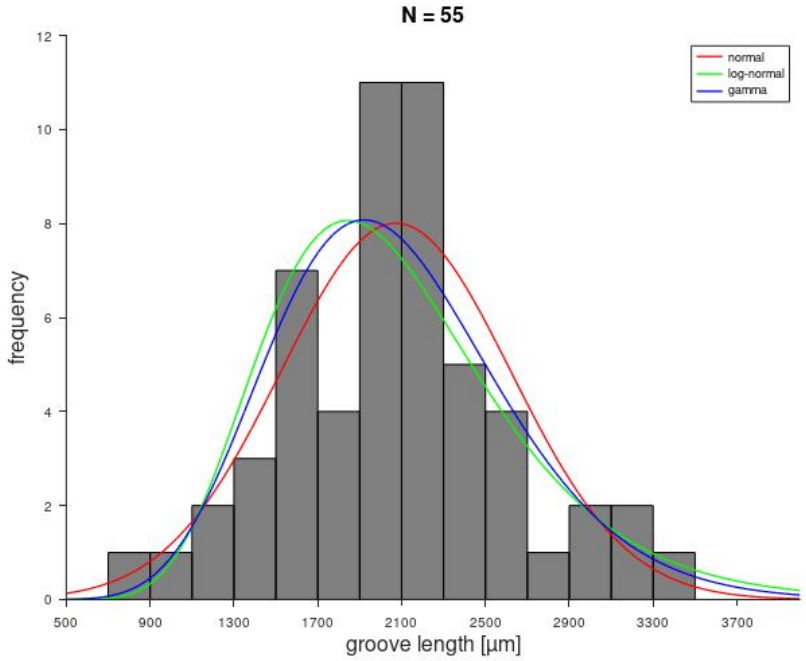

Figure A.13: Histogram of sample BAC1-1 827.52 FR with probability distribution.

A.8 SEM images

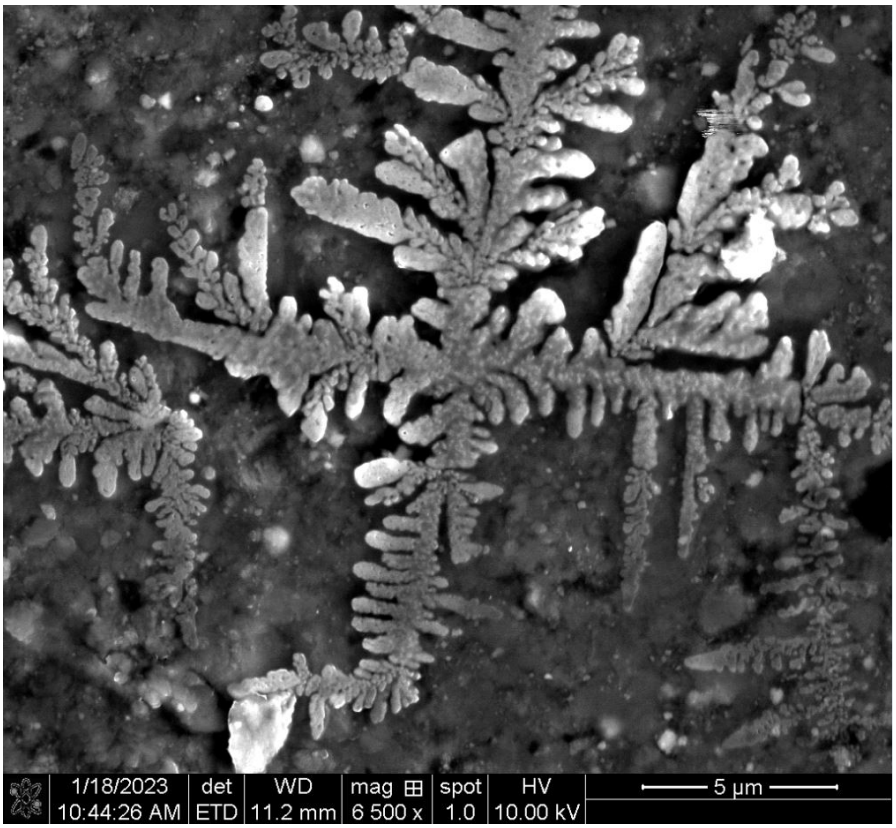

Figure A.14: Dendrites of sample BAC1-1 859.09 FR.

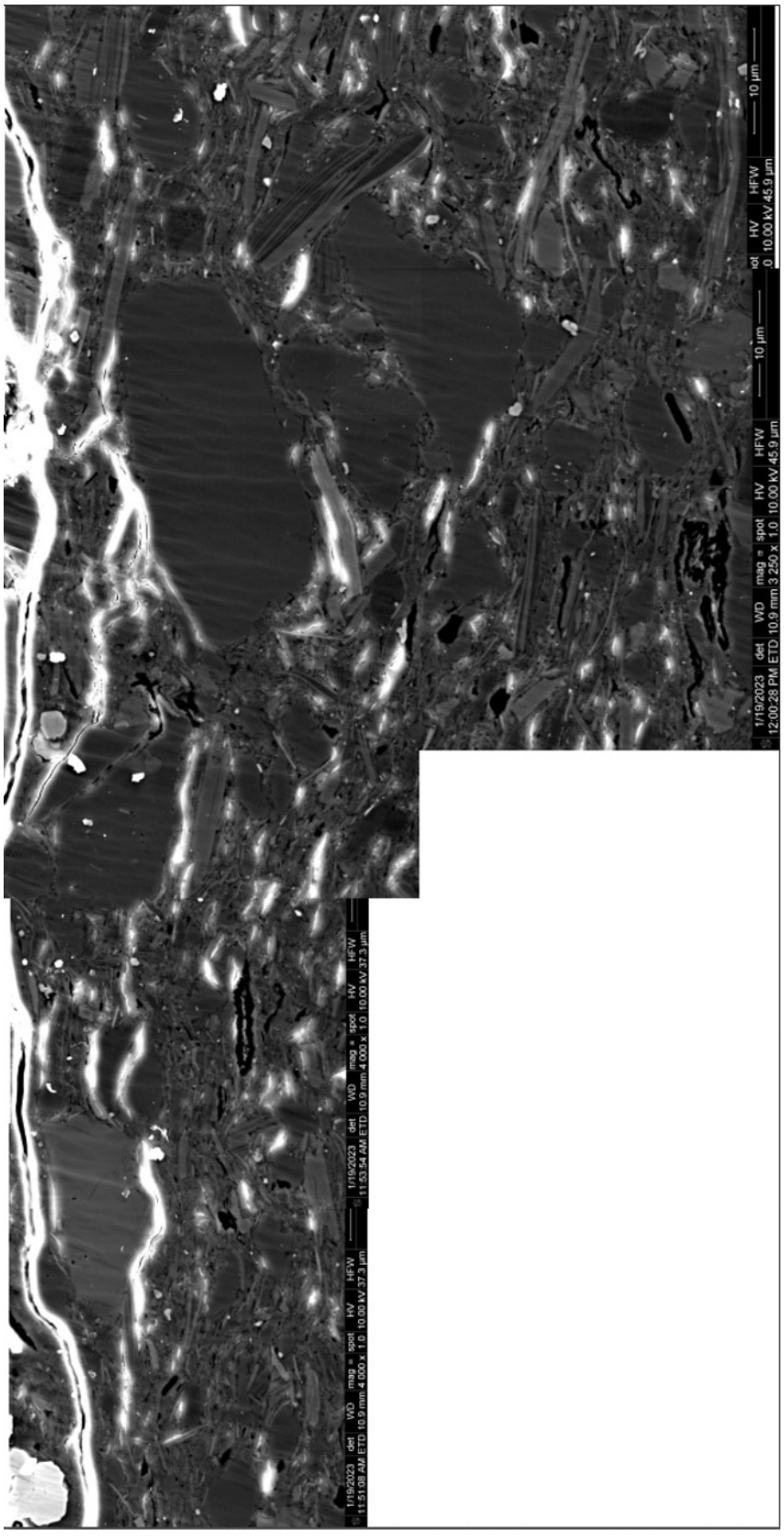

Figure A.15: Merged images of sample BAC1-1 827.52 FR.

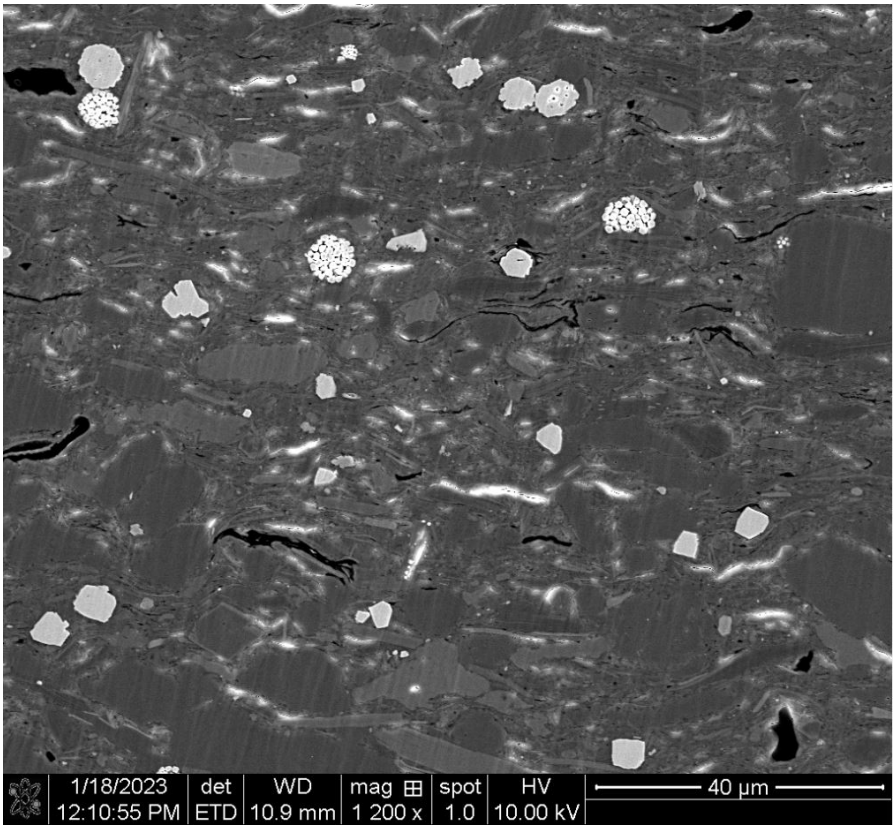

Figure A.16: Sample BAC1-1 827.52 FR, showing pyrite framboids.

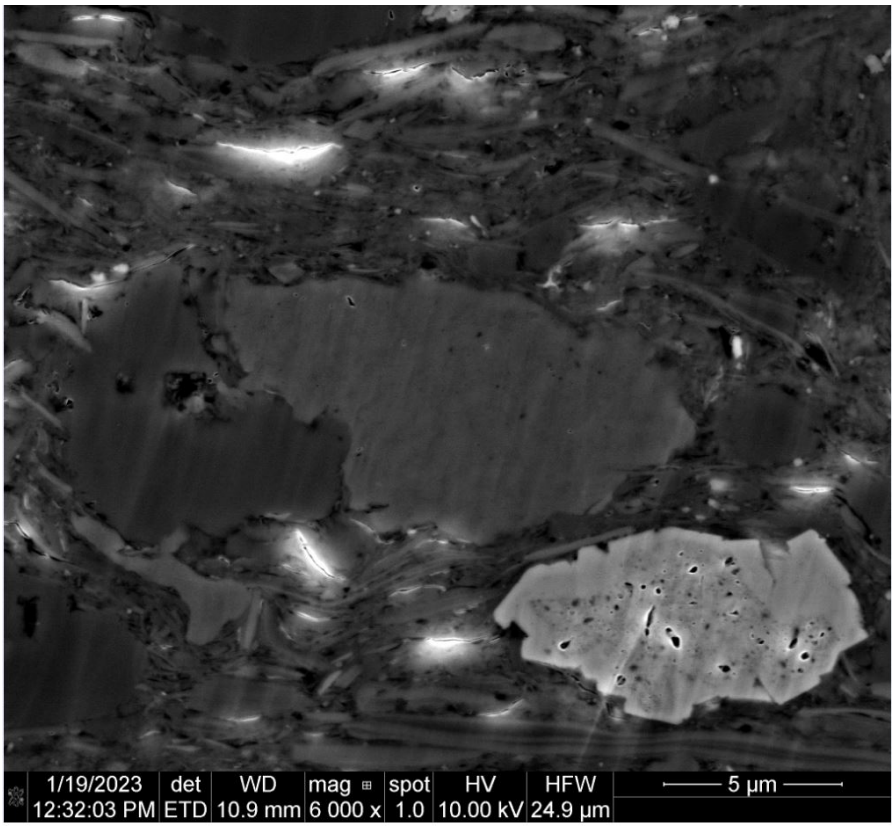

Figure A.17: Sample BAC1-1 827.52 FR. Note contact between feldspar (left) and calcite (right).

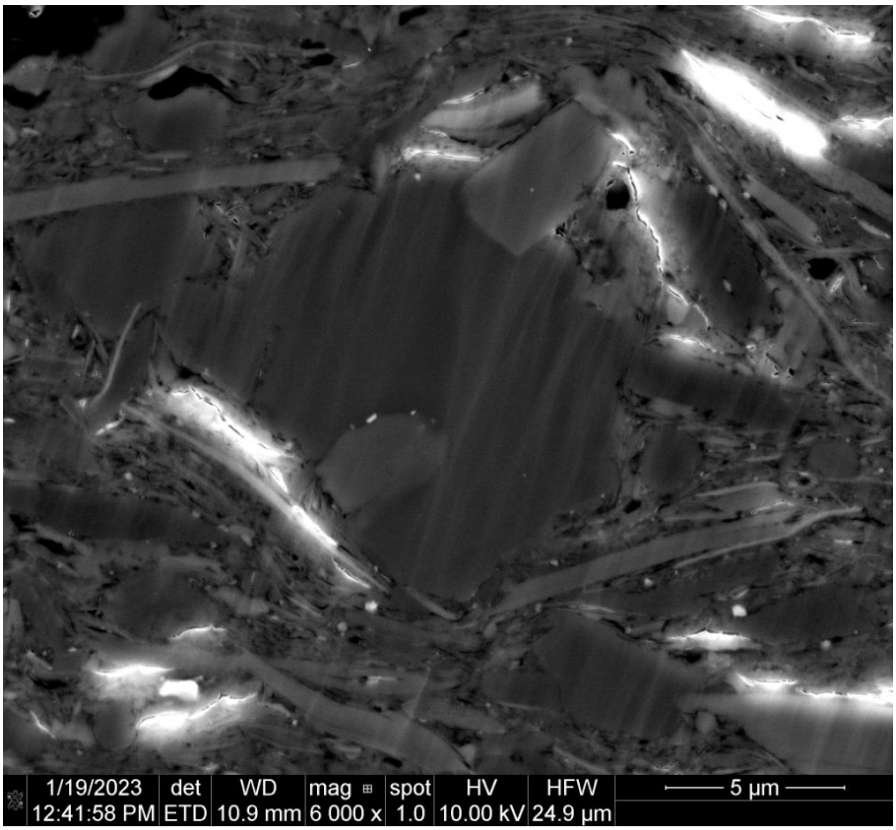

Figure A.18: Sample BAC1-1 827.52 FR, showing big quartz grain overlapped by k-feldspar grain in the top right corner.

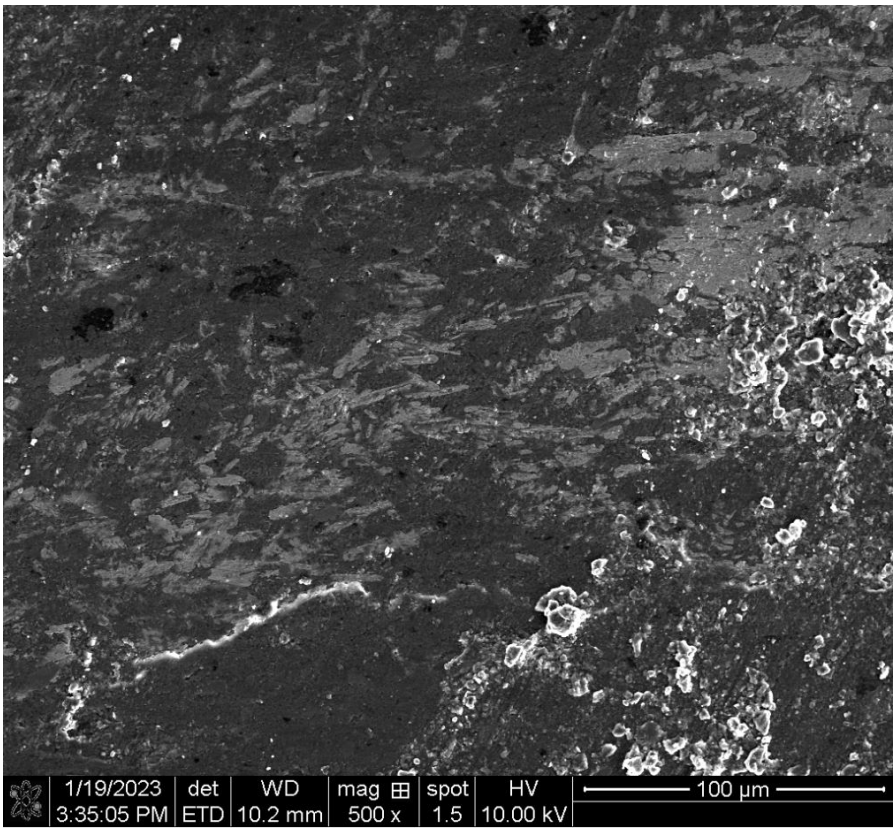

Figure A.19: Surface of slickenside of sample RHE1-1 637.94 FR with celestite and baryte minerals (white).

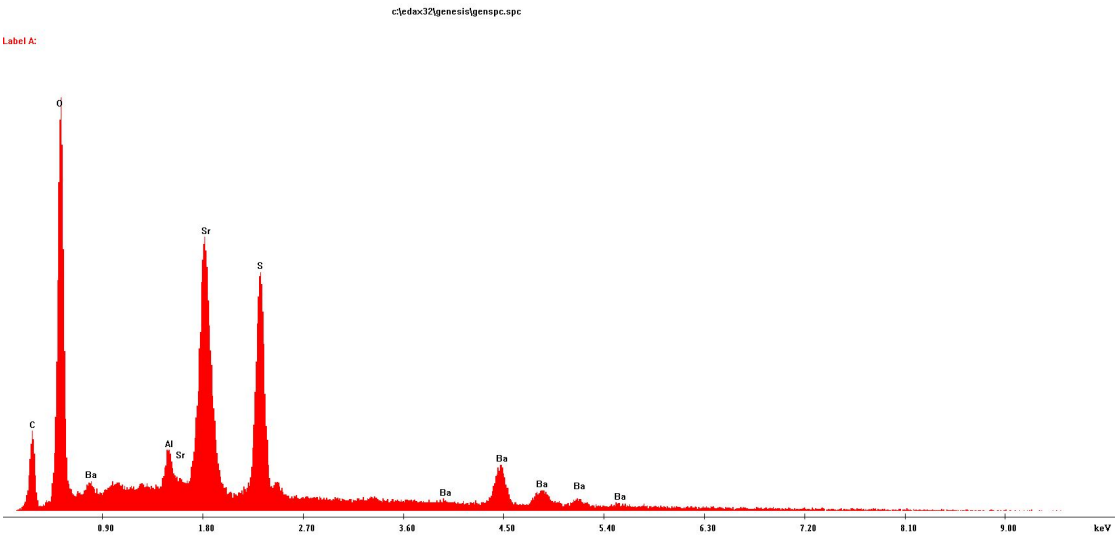

Figure A.20: EDS spectrum of the white minerals of sample RHE1-1 637.94 FR. Results show composition of celestite/baryte minerals.

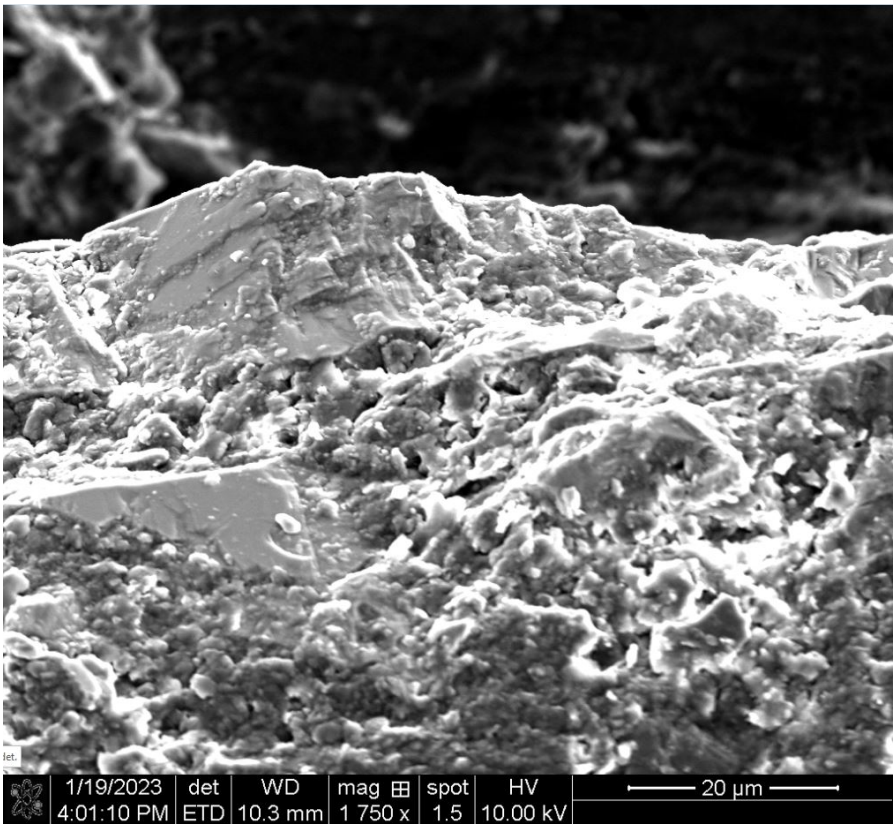

Figure A.21: Surface of sample RHE1-1 637.94 FR showing celestite/baryte minerals.

A.9 Total mineralogy

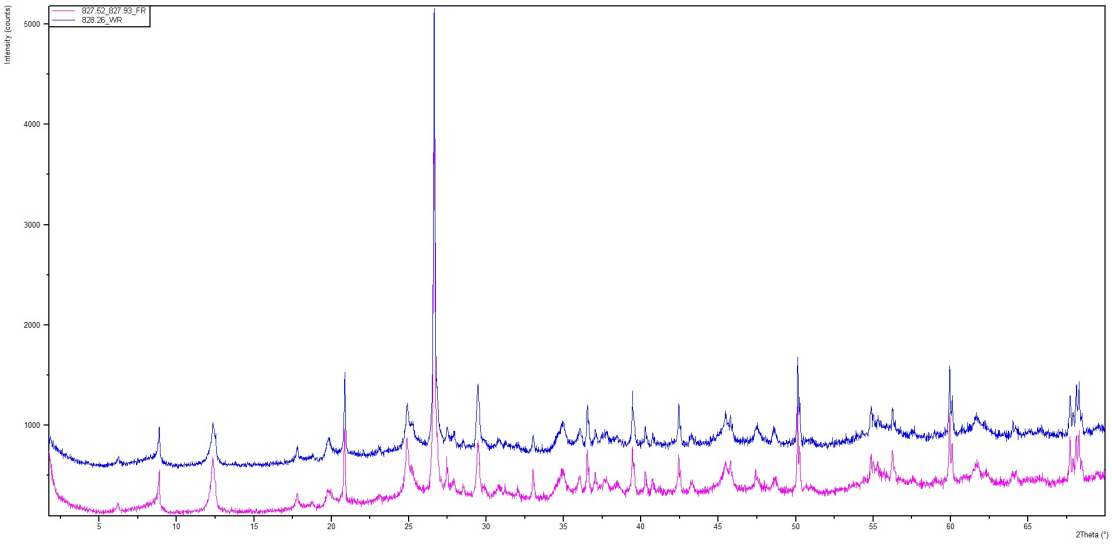

Figure A.22: XRD pattern of the mineralogical composition of sample BAC1-1 828.26 wall rock (blue) and fault rock (pink).

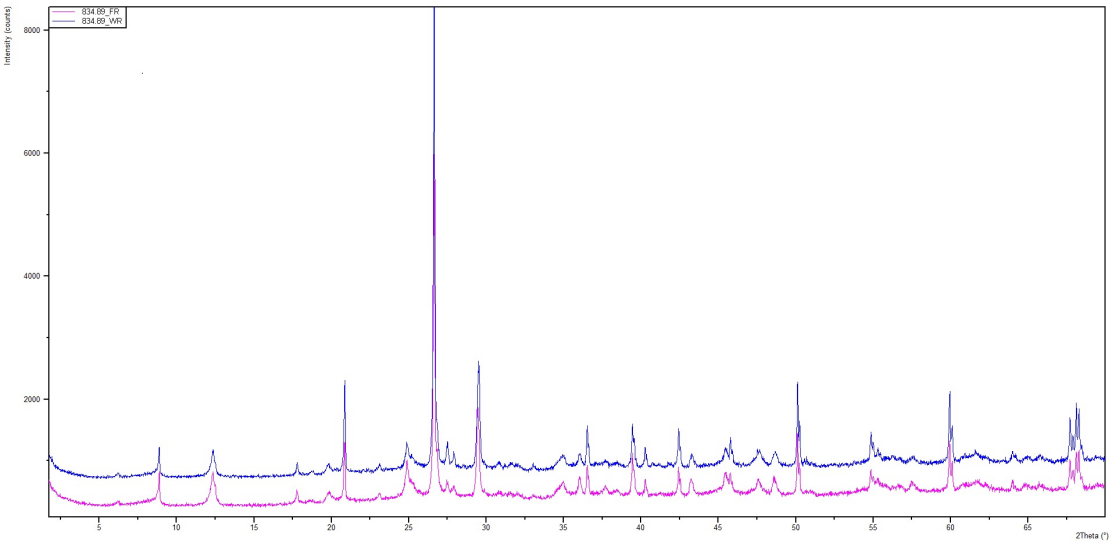

Figure A.23: XRD pattern of the mineralogical composition of sample BAC1-1 834.89 wall rock (blue) and fault rock (pink).

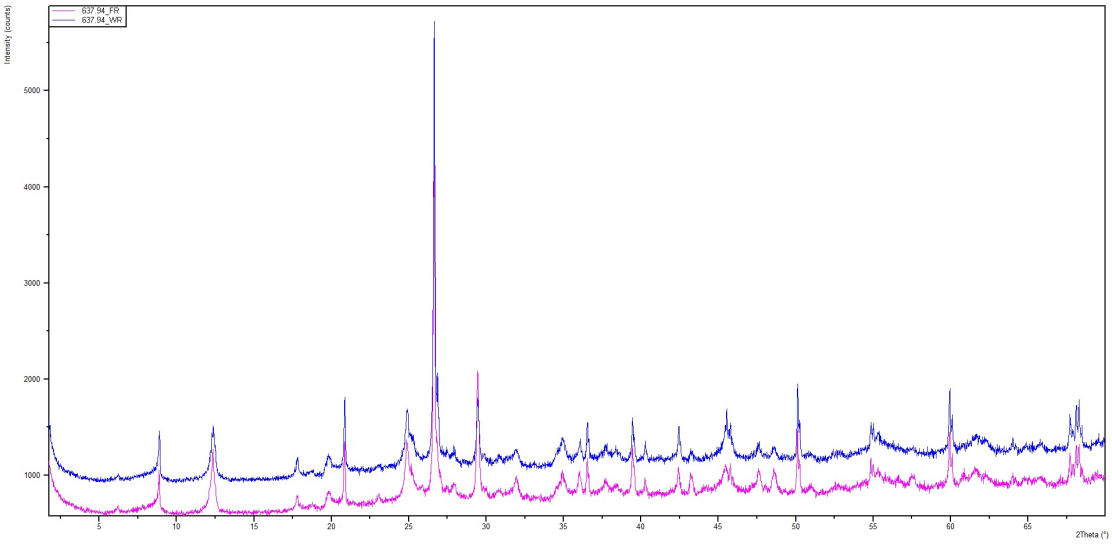

Figure A.24: XRD pattern of the mineralogical composition of sample RHE1-1 637.94 wall rock (blue) and fault rock (pink).

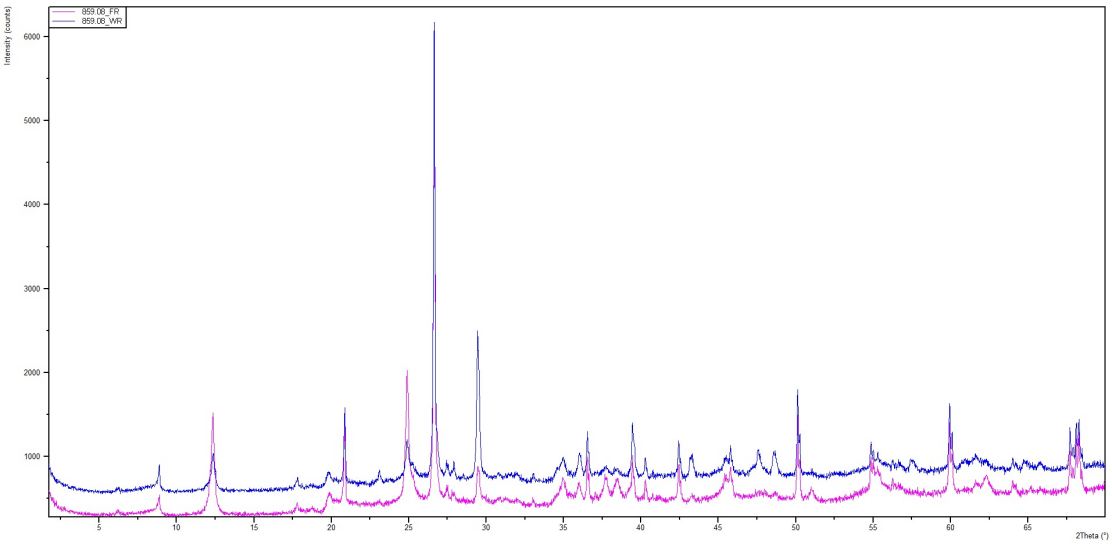

Figure A.25: XRD pattern of the mineralogical composition of sample BAC1-1 859.08 wall rock (blue) and fault rock (pink).

A.10 clay mineralogy

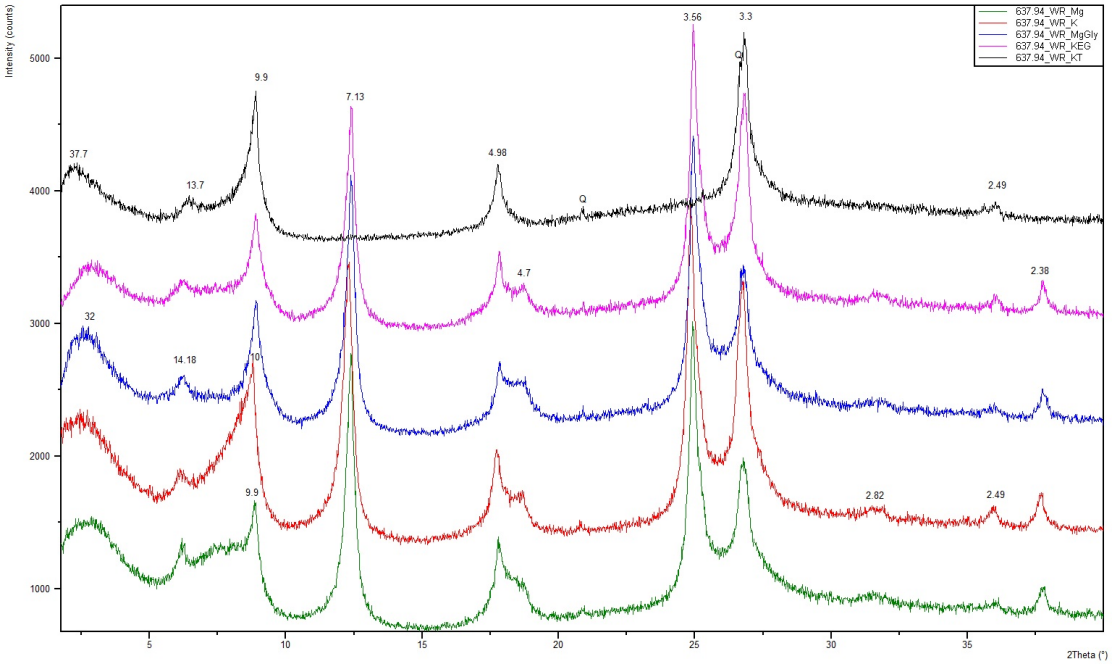

Figure A.26: Combined XRD patterns of sample RHE1-1 637.94 WR.

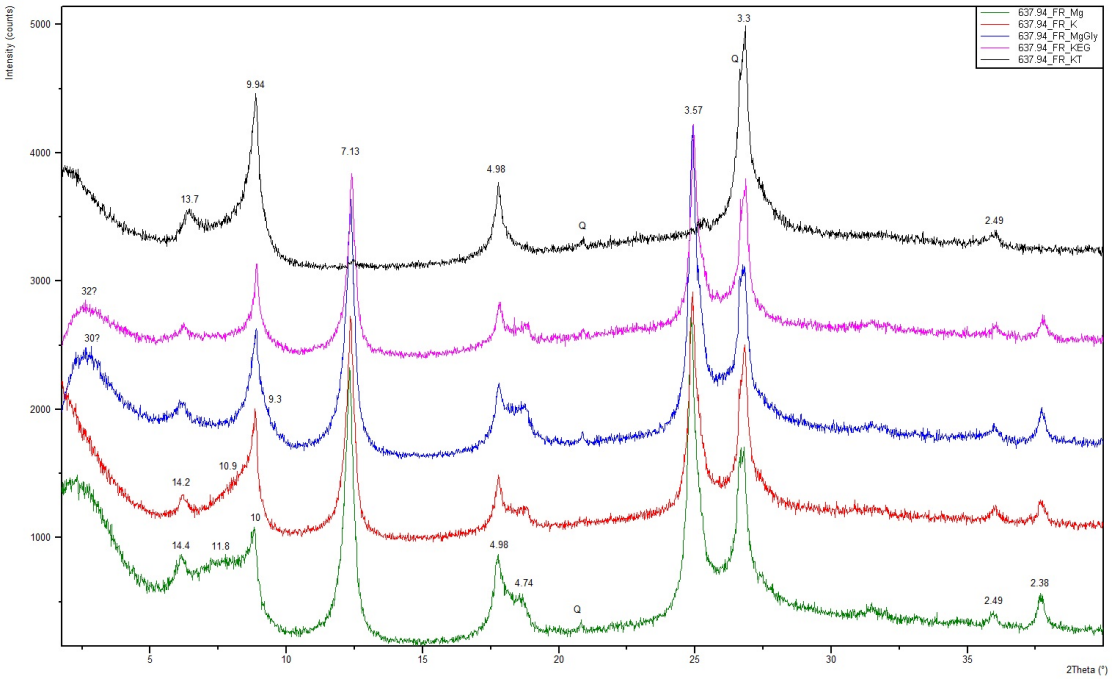

Figure A.27: Combined XRD patterns of sample RHE1-1 637.94 FR.

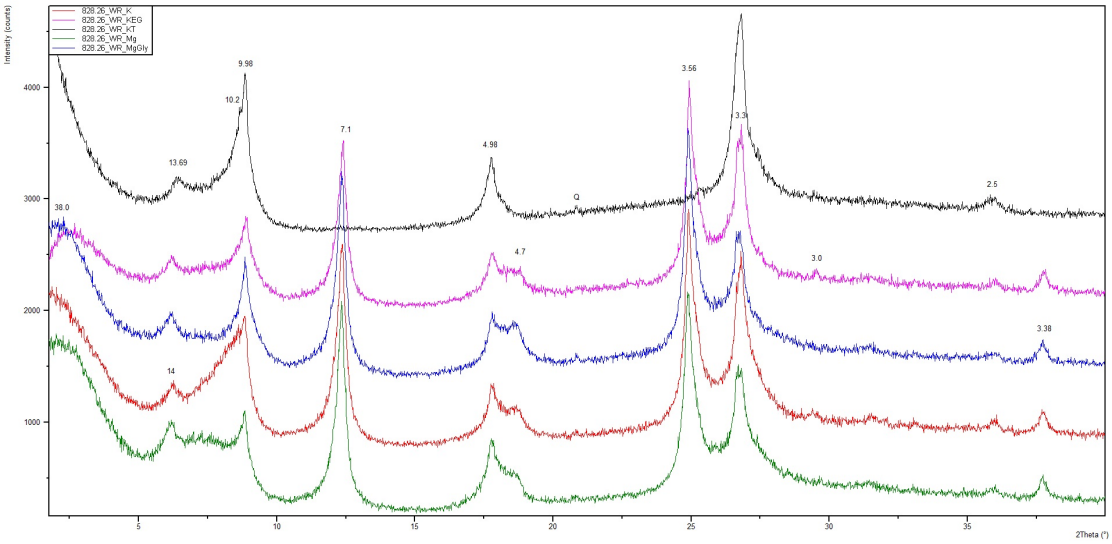

Figure A.28: Combined XRD patterns of sample BAC1-1 828.26 WR

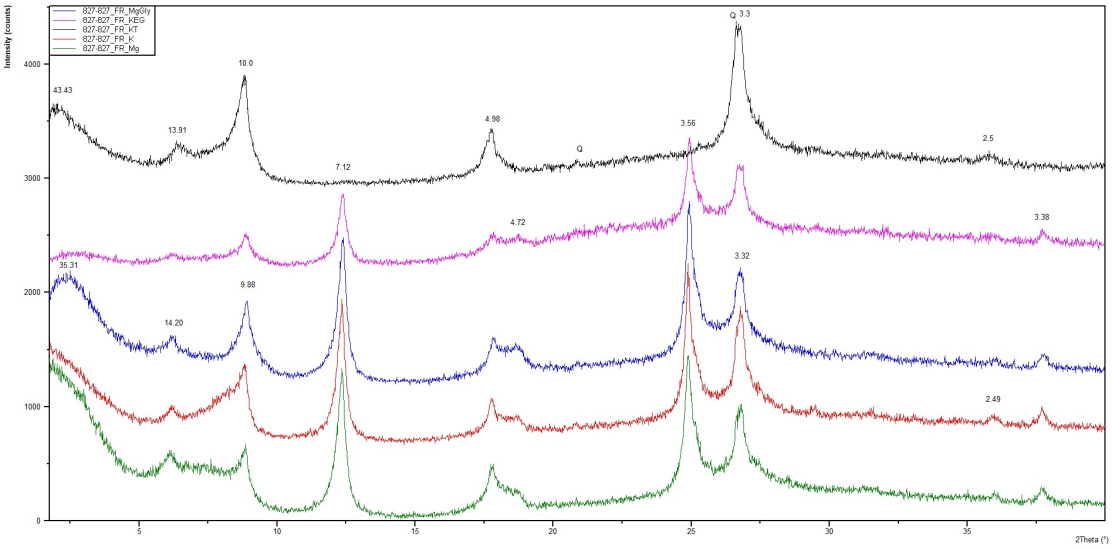

Figure A.29: Combined XRD patterns of sample BAC1-1 828.26 FR.

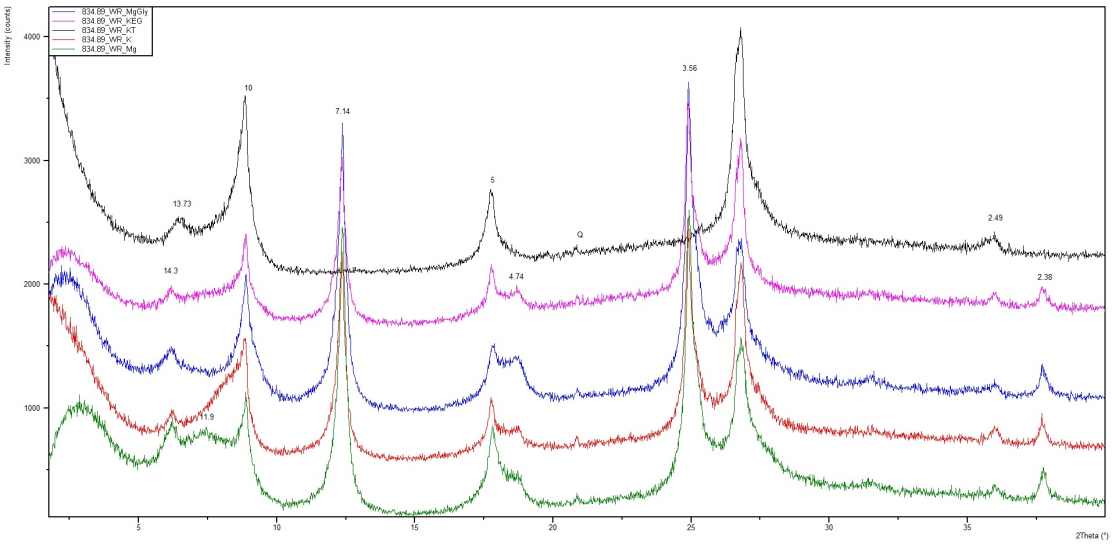

Figure A.30: Combined XRD patterns of sample BAC1-1 834.89 WR.

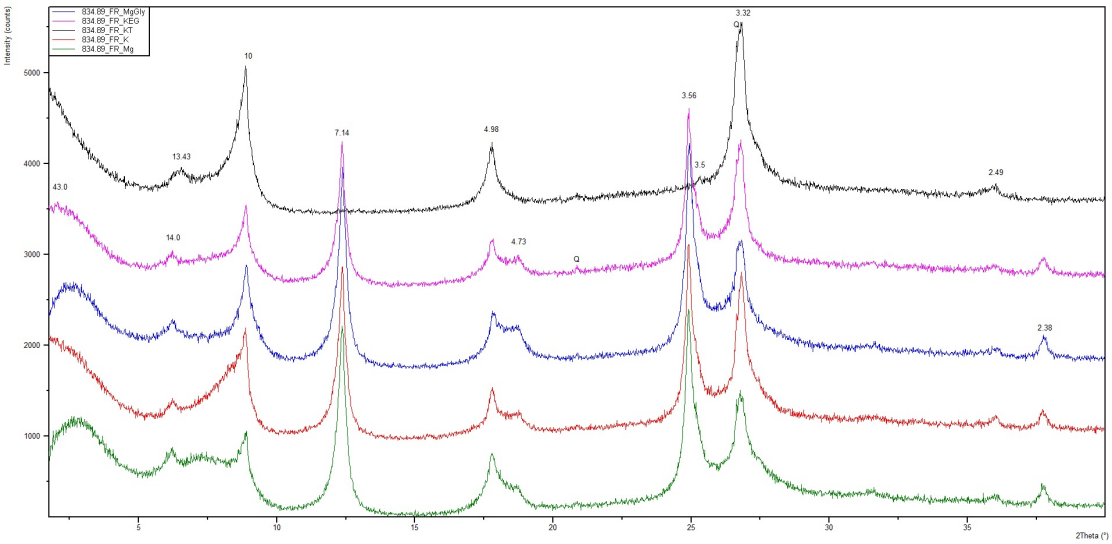

Figure A.31: Combined XRD patterns of sample BAC1-1 834.89 Fr.

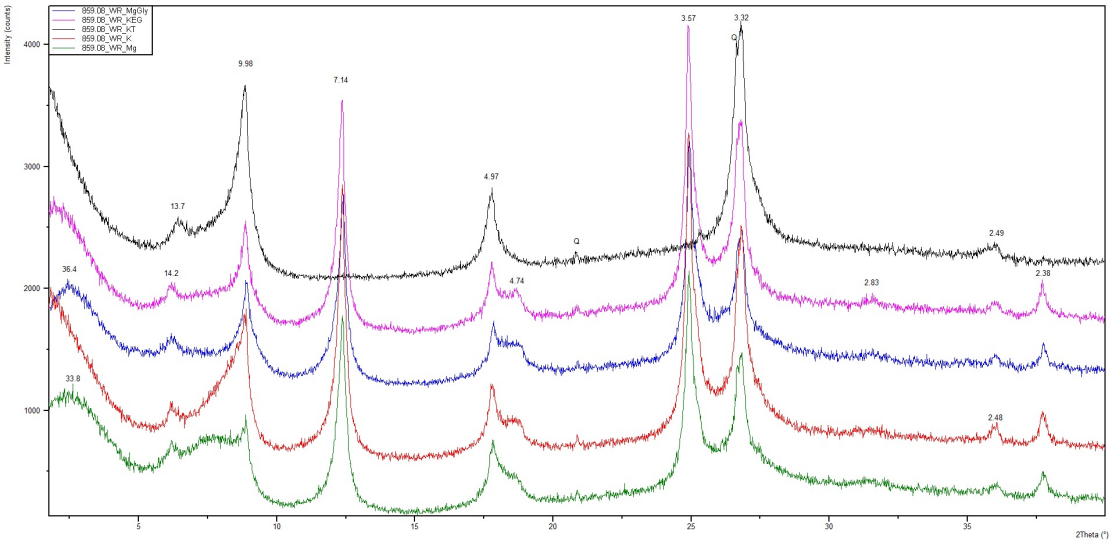

Figure A.32: Combined XRD patterns of sample BAC1-1 859.08 WR.

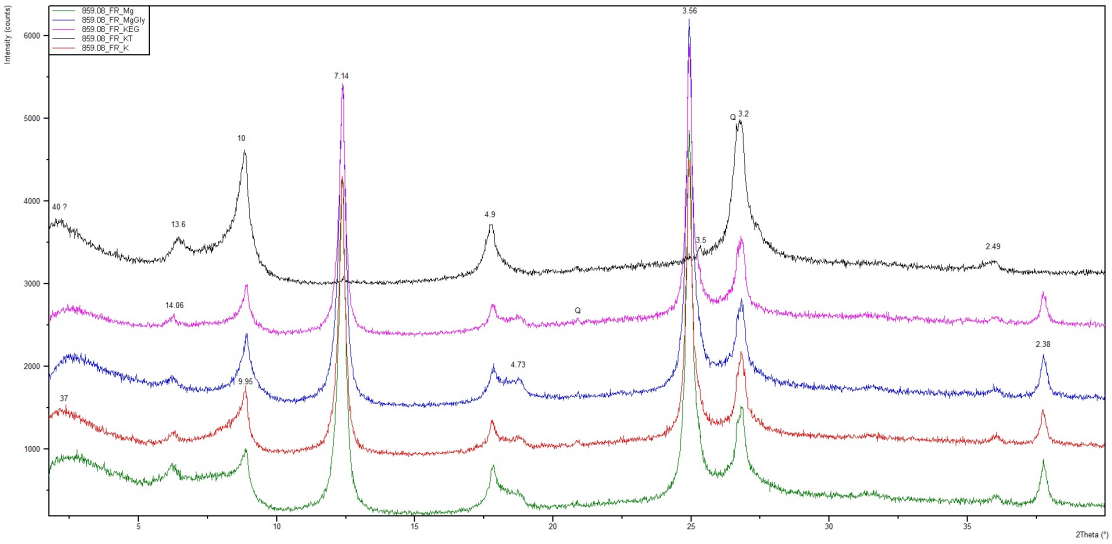

Figure A.33: Combined XRD patterns of sample BAC1-1 859.08 FR.

A.11 Fault/wall rock

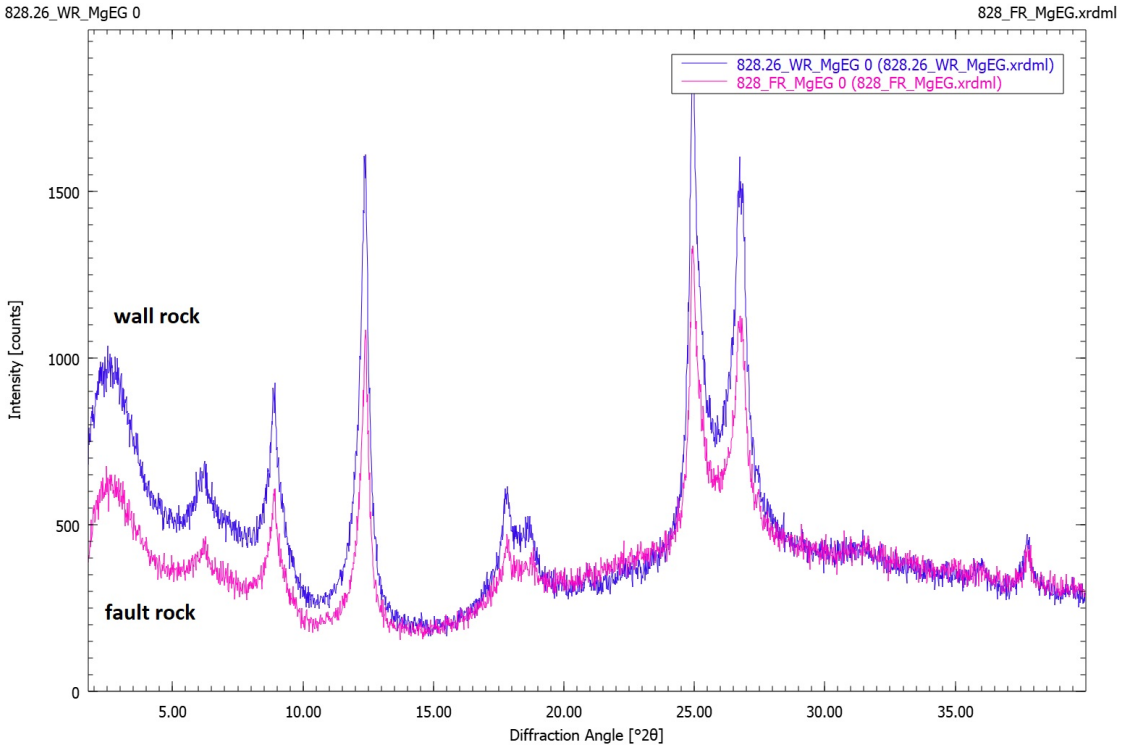

Figure A.34: XRD pattern of Mg and EG saturated sample BAC1-1 828.26 wall rock (blue) and fault rock (pink).

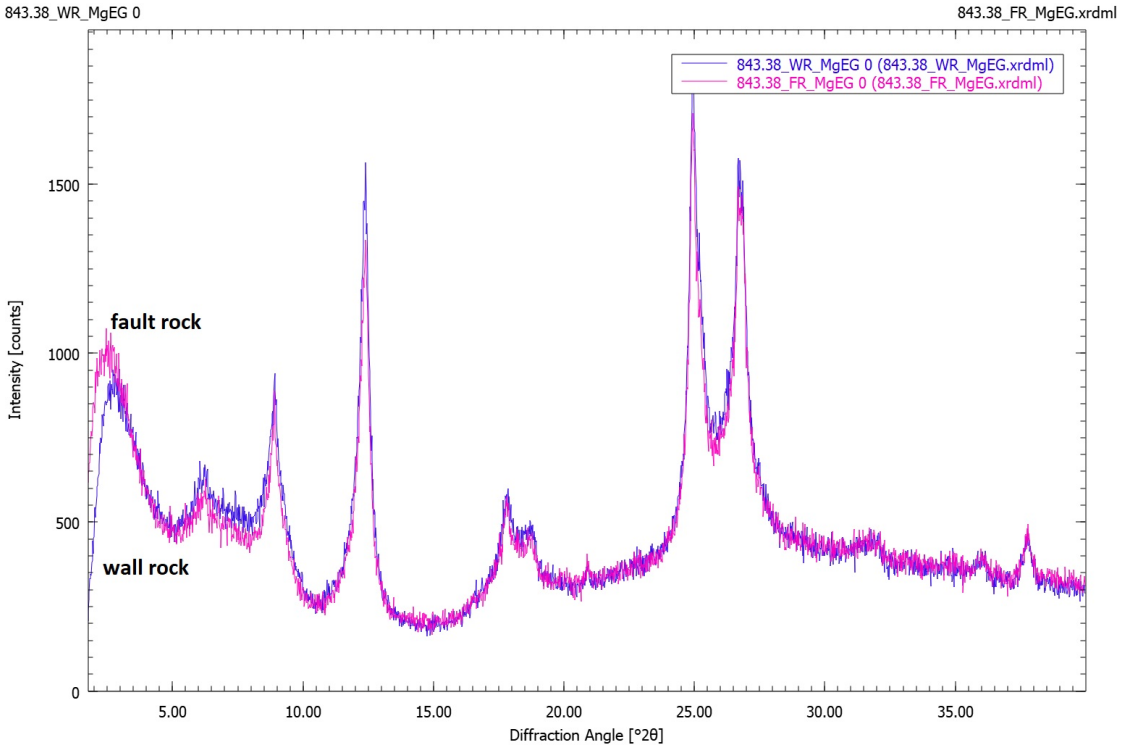

Figure A.35: XRD pattern of Mg and EG saturated sample STA2-1 843.38 wall rock (blue) and fault rock (pink).

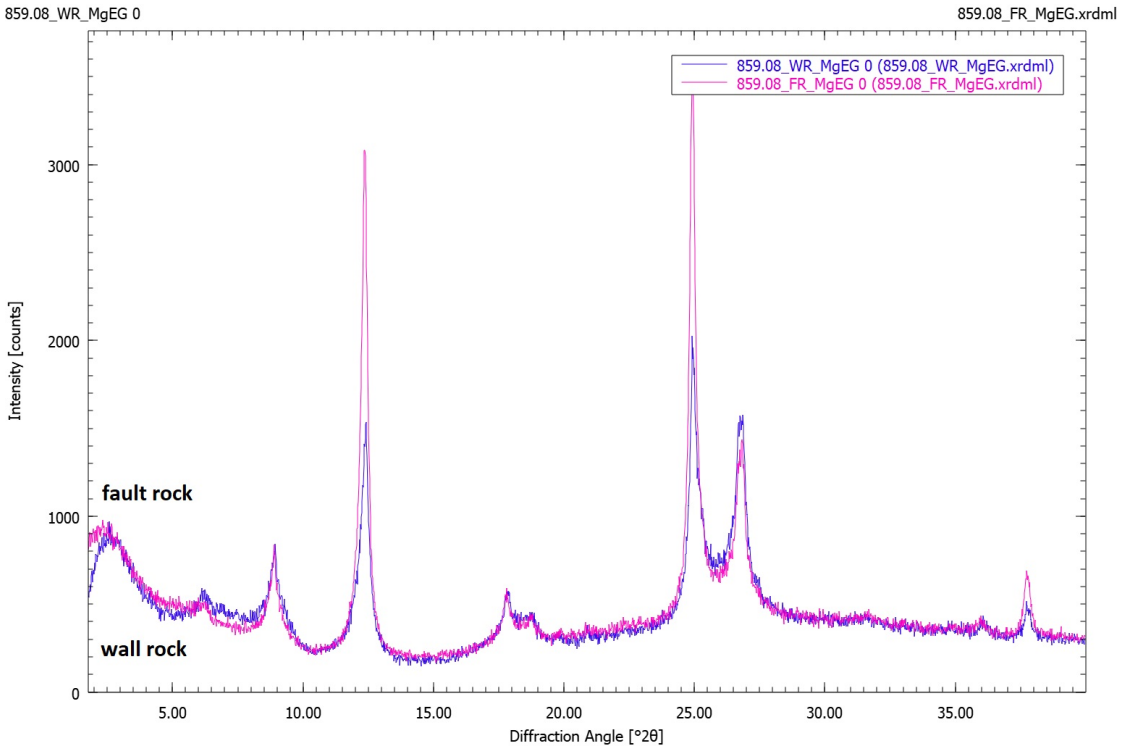

Figure A.36: XRD pattern of Mg and EG saturated sample BAC1-1 850.08 wall rock (blue) and fault rock (pink).

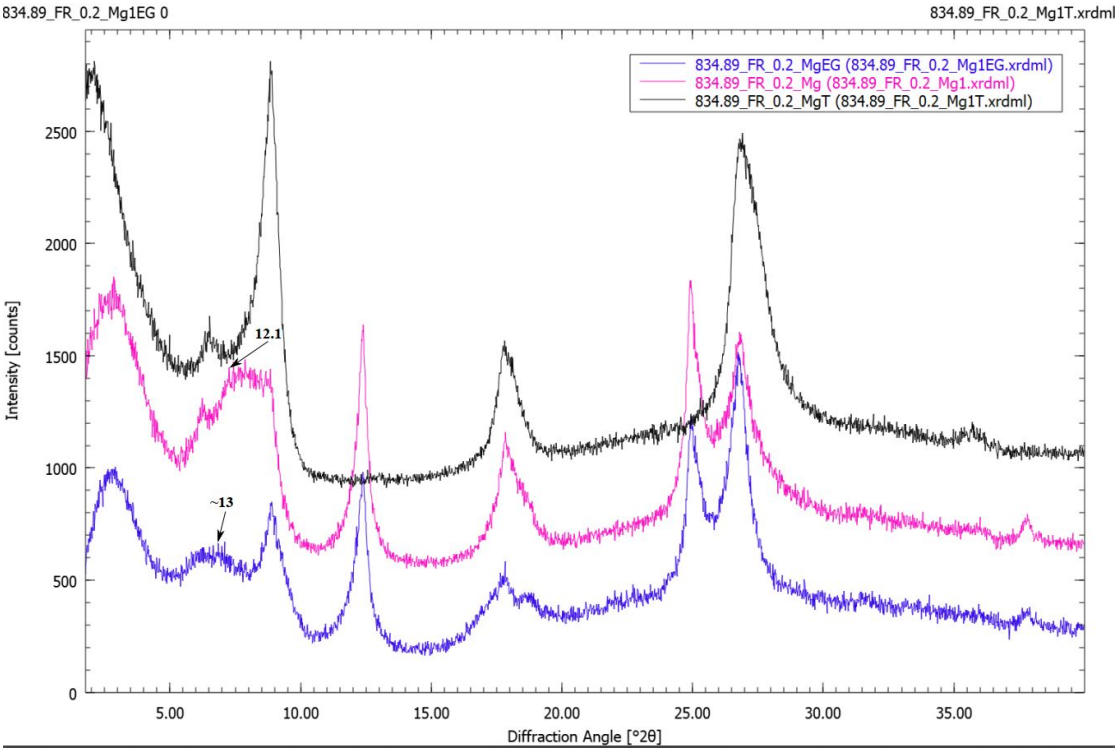

Figure A.37: XRD pattern of sample BAC1-1 834.89 fault rock saturated with Mg and EG (blue), Mg (pink), and heated.

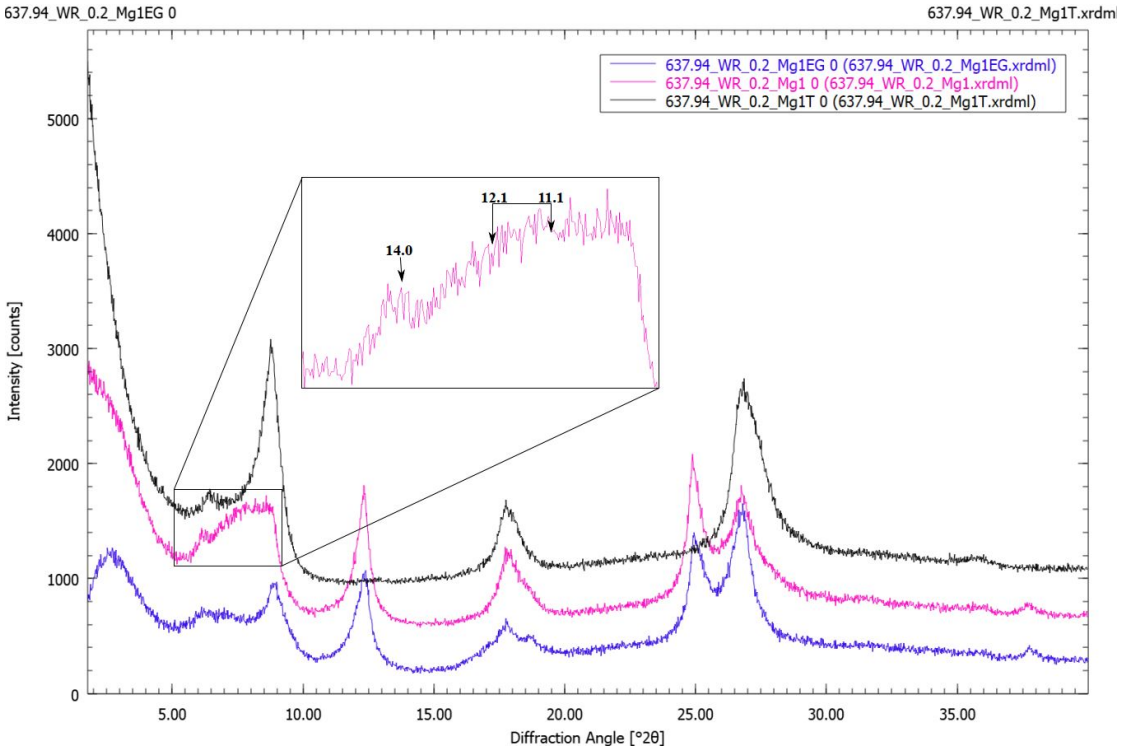

Figure A.38: XRD pattern of sample RHE1-1 637.94 wall rock saturated with Mg and EG (blue), Mg (pink), and heated. Note, hump between 12.1 Å and 11.1 Å indicates a I/S mixed layer clay mineral.

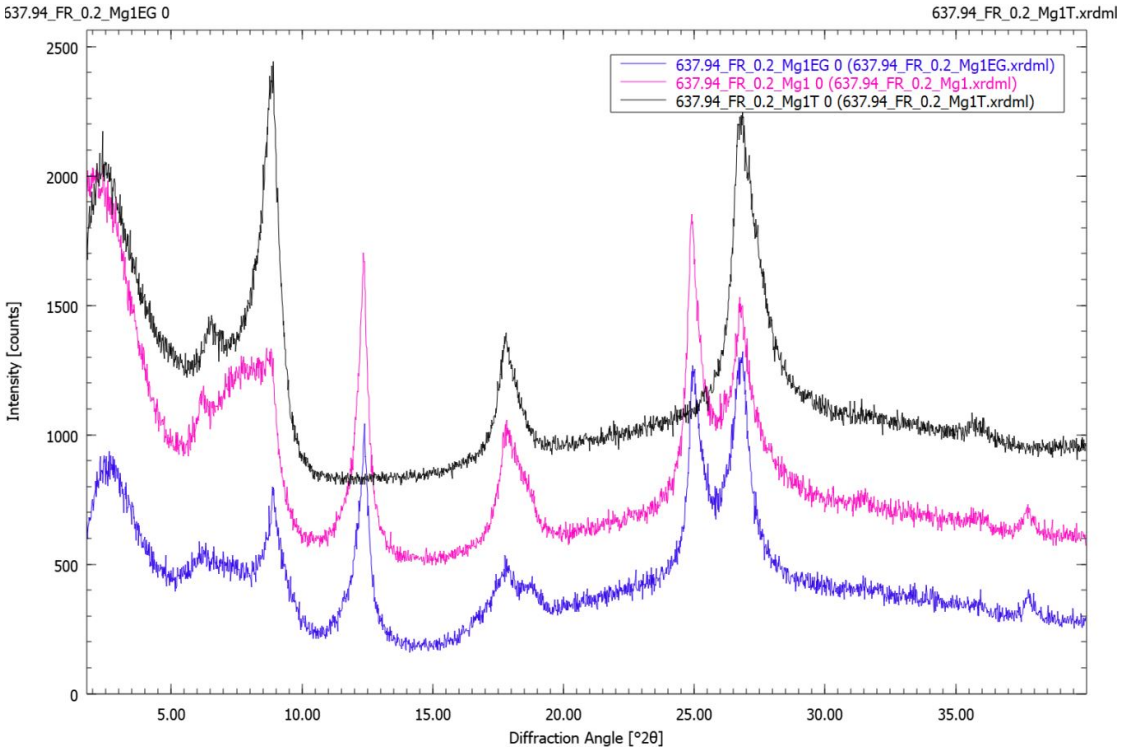

Figure A.39: XRD pattern of sample RHE1-1 637.94 fault rock saturated with Mg and EG (blue), Mg (pink), and heated.

A.12 Cation exchange capacity

Well	Core depth / type	1	2	3	4	5	average	CEC (mmol/100g)
STA2-1	843.38 WR	0.276	0.276	0.276	0.276	0.276	**0.276**	35.664
STA2-1	843.38 FR	0.317	0.316	0.317	0.318	0.317	**0.317**	26.107
BAC1-1	859.08 WR	0.316	0.316	0.316	0.316	0.316	**0.316**	26.340
BAC1-1	859.08 FR	0.310	0.310	0.310	0.310	0.310	**0.310**	27.738
BAC1-1	828.26 WR	0.276	0.276	0.276	0.277	0.275	**0.276**	35.664
BAC1-1	828.26 FR	0.355	0.358	0.355	0.356	0.354	**0.356**	17.109
Eb		0.429	0.429	0.429	0.429	0.429	**0.429**	
Hennersdorf Standard		0.279	0.279	0.278	0.279	0.278	**0.279**	14.023

Table A.1: Results of every absorbance measurement and average of all measurements, used for calcualtion of cation exchange capacity. Eb = blank value (deionized water). Hennersdorf Standard sample to check the correctness of measurement.